THE UNIVERSITY OF
SYDNEY

COPYRIGHT AND USE OF THIS THESIS

This thesis must be used in accordance with the provisions of the Copyright Act 1968.

Reproduction of material protected by copyright may be an infringement of copyright and copyright owners may be entitled to take legal action against persons who infringe their copyright.

Section 51 (2) of the Copyright Act permits an authorized officer of a university library or archives to provide a copy (by communication or otherwise) of an unpublished thesis kept in the library or archives, to a person who satisfies the authorized officer that he or she requires the reproduction for the purposes of research or study.

The Copyright Act grants the creator of a work a number of moral rights, specifically the right of attribution, the right against false attribution and the right of integrity.

You may infringe the author's moral rights if you:

- fail to acknowledge the author of this thesis if you quote sections from the work
- attribute this thesis to another author
- subject this thesis to derogatory treatment which may prejudice the author's reputation

For further information contact the University's Director of Copyright Services

sydney.edu.au/copyright

Reformation and Ion Dynamics of Quasiperpendicular Collisionless Shocks

A thesis submitted in fulfilment
of the requirements for the degree of
Doctor of Philosophy

by

Dion Tiu

School of Physics
University of Sydney
Australia

December, 2014

Declaration of originality

To the best of my knowledge, this thesis contains no copy or paraphrase of work published by another person, except where duly acknowledged in the text. This thesis contains no material which has previously been presented for a degree at the University of Sydney or any other university.

Dion Tiu

Included papers and attribution

Chapter 2 **Evidence for Reformation of the Uranian Bow Shock: Hybrid Simulations and Comparisons with Voyager Data**
D. Tiu, I. H. Cairns, X. Yuan, and P. A. Robinson,
Published in *J. Geophys. Res.*, 116, A04228 (2011).

I was primarily responsible for this work.

Chapter 3 **New Model for the Initial Reflection and Transmission of Thermal Ions at Quasiperpendicular Collisionless Shocks**
D. Tiu, I. H. Cairns, X. Yuan.

I was primarily responsible for this work.

Chapter 4 **Source Regions, Energization, and Populations of Different Classes of Ion Trajectories at Perpendicular Collisionless Shocks**
D. Tiu, I. H. Cairns.

I was primarily responsible for this work.

Acknowledgements

I would firstly like to thank my supervisor Prof. Iver Cairns for his guidance, patience, and unwavering support throughout my candidature, without whom this thesis would not be possible. I would also like to thank Dr. Xinqiu Yuan for allowing me to use and modify his simulation code.

I am especially grateful to my wife May for her love, care, and endless patience over the entire course of my university education. To my parents, I am forever indebted by the love, guidance, and generosity you've shown me throughout my life — thank you.

Abstract

Collisionless shocks are ubiquitous throughout the Universe. Shocks are nonlinearly steepened waves which cause plasmas to undergo dramatic changes in their density, temperature, flow velocity, and magnetic field. A plasma is called collisionless when the frequency of collisions between charged particles is substantially lower than the natural frequencies of the plasma, such as the electron plasma frequency or the electron gyrofrequency. The presence of a magnetic field in collisionless plasmas leads to a rich collection of different shock types and furthermore a wide variety of wave phenomena and particle dynamics are supported at such shocks. The unique physical behaviors and properties of magnetized collisionless shocks, compared to those of the classical gasdynamic shock, make them one of the most extensively studied nonlinear classes of phenomena in plasmas.

In this thesis we study several different but connected problems in collisionless shock physics. In Chapter 1 we present an overview of basic plasma theory, particularly of collisionless shocks in plasmas described using magnetohydrodynamic (MHD) theory. In Chapter 2, detailed quantitative evidence for shock reformation (a temporal variability of the shock structures) is presented from the Voyager 2 spacecraft's encounter with the Uranian bow shock. This evidence is based on finding very good agreement between Voyager observations of the Uranian bow shock and results from a standard 1-D hybrid simulation code run with similar plasma parameters. Specifically, the multiple large localized magnetic field enhancements $B/B_1 \sim 16$ observed downstream by Voyager 2, where $B_1 = 0.19$ nT is the upstream magnetic field, are quantitatively consistent with the reforming shock found in the simulation.

Chapter 3 develops a new analytic model for the reflection and transmission of ions at quasiperpendicular (the angle between the shock normal and upstream magnetic field is between $45° - 90°$) shocks. We show, using 1-D hybrid and test-particle simulations, that ions reflected at the shock ramp are decelerated by magnetic field effects, herein referred to as "magnetic deflection", in addition to the cross-shock electrostatic potential. We quantify the

contribution of magnetic deflection to ion reflection and in doing so resolve a discrepancy between the predicted ion reflection efficiency (based on the electrostatic potential jump alone) and numerical values calculated in our hybrid simulations. Moreover, an analytic expression for the reflection cutoff of ions reflected by the cross-shock potential and magnetic deflection is derived. We find excellent agreement between the simulations and the new model for ion reflection by the shock front, and show that both the electrostatic potential and magnetic field effects are vital in the ion reflection process.

Chapter 4 proposes a new classification scheme at perpendicular shocks for the classes of ion trajectories across the different shock regions of the foot, ramp, overshoot, and downstream plasma. For each particle class we calculate its energization, fractional population, and source region in initial velocity phase space using multiple test-particle simulations. We find that particle energization is mostly sensitive to the thickness of the shock and the magnitude of the electrostatic potential. Mild energy gains are observed for shocks with an overshoot whereas including a foot structure only changes the source regions for certain particle classes. Furthermore, we develop and test two new analytic reflection conditions for: (1) particles that are initially reflected by the electrostatic potential, complete half a gyro-orbit upstream, and finally escape downstream, and (2) particles that are initially transmitted downstream but return to the shock as part of their downstream gyromotion, complete half a gyro-orbit upstream, and finally escape downstream. In the former case, we find excellent agreement between analytic and numerical results; however, in the latter case we find good agreement only in simulations with thin shocks.

Contents

Chapter 1

Introduction and Literature Review

In this Chapter we provide a brief review of basic plasma and shock theory. We begin in Section 1.1 with a basic description of plasmas and their physical properties. In Section 1.2 we introduce orbit theory and common particle drifts. Kinetic and fluid theory are outlined in Section 1.3 followed by a brief discussion of magnetohydrodynamic theory in Section 1.4. Magnetosonic waves and their characteristics are described in Section 1.5. Section 1.6 discusses the governing physics of shocks waves and the different types of simulations used to model shock phenomena. We then examine the ion dynamics at shocks in Section 1.7 and review the different models and observational evidence for shock reformation in Section 1.8.

1.1 Plasmas

A plasma is gas which has been at least partially ionized, by removing some or all of each atom's electrons to travel through the medium separately and interact with the ionized atoms (or "ions"). On a local scale, plasmas consist of roughly equal numbers of free electrons and ions whence a plasma looks electrically neutral to the outside. This is known as quasineutrality, whereby the electric fields of the randomly distributed particles mutually cancel. The Debye length λ_D is the characteristic length at which balance is achieved between the thermal particle energy, which correspond to motions that tend to perturb charge neutrality, and the electrostatic potential energy resulting from charge separation, which tends to restore charge neutrality. For a plasma with singly charged ions, similar electron and ion temperatures $T_e \simeq T_i$, and similar electron and ion number densities $n_e \simeq n_i$, the Debye length is equal to (e.g.

Kivelson and Russell [1995])

$$\lambda_D = \left(\frac{\epsilon_0 k_B T_e}{n_e e^2}\right)^{1/2} \tag{1.1}$$

where ϵ_0 is the permittivity of free space, k_B is Boltzmann's constant, and e is the electric charge.

If some external force disturbs quasineutrality the electrons, which are more mobile than the heavier ions, are accelerated and then attempt to restore quasineutrality. The electrons will oscillate back and forth around an equilibrium position at the *electron plasma frequency* (e.g. *Kivelson and Russell* [1995]),

$$f_{pe} = \left(\frac{n_e e^2}{4\pi^2 m_e \epsilon_0}\right)^{1/2} \tag{1.2}$$

where m_e is the electron mass.

In a fully ionized plasma, electrons and ions interact via their electric Coulomb fields; the rate at which this occurs is known as the *Coulomb collision frequency*, and is given by (e.g. *Baumjohann and Treumann* [1999])

$$\nu_{ei} \sim f_{pe} \frac{\ln \Lambda}{\Lambda} \tag{1.3}$$

where $\Lambda = n_e \lambda_D^3$ and $\ln \Lambda$ is known as the *Coulomb logarithm*. It is appropriate to distinguish between two types of plasmas based on their relative Coulomb collision frequency to electron plasma frequency: if $\nu_{ei} \gg f_{pe}$ the plasma is *collisional* and if $\nu_{ei} \ll f_{pe}$ the plasma is *collisionless*. In the latter, collisions are so infrequent compared to any relevant variations in the fields or particle dynamics that they can be safely neglected. On the other hand, in collisional plasmas, collisions are sufficiently frequent that they play a vital role in the behavior of the plasma. Most space plasmas, including those we will be dealing with, are collisionless and support phenomena that are unique to them.

1.1.1 Solar Wind

One of the most important plasmas observed in nature is the solar wind generated by the Sun [*Kivelson and Russell*, 1995]. The solar wind is a hot collisionless plasma which expands radially outward from the Sun. Near the Earth the solar wind has typical values of the $n_e \approx 5$ cm^{-3} and $T_e \approx 10^5$ K respectively. The solar wind carries with it what is known as the interplanetary magnetic field **B** (IMF) because of the *frozen-in* theorem: in an ideal MHD plasma the magnetic field lines along a single flux tube remain linked as they convect through space. As a result the IMF **B** spreads throughout the entire solar system; its value is typically 5 nT near Earth.

1.1.2 Magnetosphere

When the solar wind encounters the Earth's magnetic field, it cannot penetrate it, but is slowed and deflected around it (because the plasma conductivity is large enough that **B** is "frozen-in" to the plasma). The *magnetosphere* is the region of space in which charged particles are influenced by the terrestrial magnetic field. The boundary separating the solar wind to the magnetospheric plasma is known as the *magnetopause*. On the nightside of the Earth the magnetosphere extends out into a long *magnetotail* far beyond the lunar orbit. The plasma in the magnetosphere consists mainly of electrons and ions but includes small fractions of He^+ and O^+ ions extracted from Earth's ionosphere.

1.2 Orbit Theory

The motion of a plasma is determined by the interaction between charge carriers and the electric **E** and magnetic **B** fields. Moving charge carriers generate electric currents and thus magnetic fields which feed back onto the overall dynamics of the plasma. In general the future motion of the plasma can be determined by solving the equation of motion for each individual particle subject to the internal fields generated by every other moving particle. Obtaining such a full solution is not only extremely difficult but impractical and so several theoretical approaches are employed depending on the type of problem studied. Nevertheless, the study of single particle motion can be useful in describing the overall plasma motion when the internal fields are unimportant compared with the macroscopic fields (e.g., the convected solar wind across its magnetic field). Orbit theory is also important in understanding the motion of energetic particles which often act as test particles.

1.2.1 Single Particle Motion

Charged particles are subject to the *Coulomb force*

$$\mathbf{F} = q\mathbf{E} \tag{1.4}$$

due to the electric field **E** and the *Lorentz force*

$$\mathbf{F} = q(\mathbf{v} \times \mathbf{B}) \tag{1.5}$$

due to the magnetic field **B**.

Now consider a particle of charge q in a uniform magnetostatic field $\mathbf{B} = B\hat{\mathbf{z}}$ but with $\mathbf{E} = 0$; it will have an acceleration of

$$\frac{d\mathbf{v}}{dt} = \frac{q}{m}(\mathbf{v} \times \mathbf{B}) \tag{1.6}$$

with individual components

$$\frac{dv_x}{dt} = \frac{qB}{m}v_y, \tag{1.7a}$$

$$\frac{dv_y}{dt} = -\frac{qB}{m}v_x, \tag{1.7b}$$

$$\frac{dv_z}{dt} = 0. \tag{1.7c}$$

The velocity component parallel to the magnetic field is constant, $v_\parallel = v_z$. Taking the time derivative of (1.7) yields

$$\frac{d^2v_x}{dt^2} = -\Omega_c^2 v_x, \tag{1.8a}$$

$$\frac{d^2v_y}{dt^2} = -\Omega_c^2 v_y. \tag{1.8b}$$

This implies that the particle undergoes circular motion with an angular frequency of

$$\Omega_c = \frac{qB}{m} \tag{1.9}$$

called the *gyrofrequency*. The particle's *gyroradius* or Larmor radius is given by

$$r_L = \frac{v_\perp}{\Omega_c} \tag{1.10}$$

where $v_\perp = (v_x^2 + v_y^2)^{1/2}$ is the magnitude of the particle's velocity perpendicular to the magnetic field. One can now write the solution for the particle's trajectory as

$$x(t) = x_0 + r_L \sin \Omega_c t \tag{1.11a}$$

$$y(t) = y_0 + r_L \cos \Omega_c t \tag{1.11b}$$

$$z(t) = z_0 + v_\parallel t \tag{1.11c}$$

where (x_0, y_0, z_0) is the center of the orbit called the *guiding center*.

1.2.2 Particle Drifts

In general, a particle's motion can be written as a combination of velocity parallel to the magnetic field $\mathbf{v}_\parallel$, its gyromotion $\mathbf{v}_g$, and its drift velocity $\mathbf{v}_D$ perpendicular to the magnetic field, with

$$\mathbf{v} = \mathbf{v}_\parallel + \mathbf{v}_g + \mathbf{v}_D. \tag{1.12}$$

Particle drifts are important in understanding plasma motion in space physics. Here we discuss several important drift mechanisms and their relevance to shocks.

Let us assume that an electrostatic field $\mathbf{E}$ is present. The electric field parallel to the magnetic field simply accelerates the particle along the same axis with

$$m\frac{dv_\parallel}{dt} = qE_\parallel. \tag{1.13}$$

Parallel electric fields in geophysical plasmas are difficult to sustain since electrons are extremely mobile along magnetic fields and can cancel these fields almost immediately.

However, if a perpendicular electric field is present along the x axis ($\mathbf{E}_\perp = E_x\hat{\mathbf{x}}$), the particle acceleration is now

$$\frac{dv_x}{dt} = \Omega_c v_y + \frac{q}{m}E_x, \tag{1.14a}$$
$$\frac{dv_y}{dt} = -\Omega_c v_x. \tag{1.14b}$$

Taking the second derivative gives

$$\frac{d^2v_x}{dt^2} = -\Omega_c^2 v_x, \tag{1.15a}$$
$$\frac{d^2v_y}{dt^2} = -\Omega_c^2\left(v_y + \frac{E_x}{B}\right). \tag{1.15b}$$

and making the substitution $v_y' = v_y + E_x/B$ recovers (1.7) where the particle is gyrating about the guiding center but now drifts in the $-y$ direction with a drift velocity of (e.g. [*Baumjohann and Treumann*, 1999])

$$\mathbf{v}_{E\times B} = \frac{\mathbf{E}\times\mathbf{B}}{B^2}. \tag{1.16}$$

known as the $\mathbf{E}\times\mathbf{B}$ drift; this velocity is charge-independent meaning that both ions and electrons will drift in the same direction.

Often the magnetic field can vary as a function of time or space, causing particles to change their perpendicular kinetic energy. Moreover, magnetic gradients perpendicular to the direction of the magnetic field can cause particles to experience a ∇B drift if the gyroradius is much smaller than the characteristic length scale L of the magnetic gradient, i.e. $r_L \ll L$.. This drift velocity is given by (e.g. [*Baumjohann and Treumann*, 1999])

$$\mathbf{v}_{\nabla B} = \frac{1}{2} v_\perp r_L \frac{\mathbf{B} \times \nabla B}{B^2}. \tag{1.17}$$

The ∇B drift speed depends on the charge so this drift can therefore cause currents and charge separations in the plasma.

Another important drift related to the topology of the magnetic field lines is curvature drift. If $\mathbf{R}_c$ is the radius of curvature, then a particle's curvature drift velocity is (e.g. [*Baumjohann and Treumann*, 1999])

$$\mathbf{v}_{curvature} = \frac{m v_\parallel^2}{q R_c^2} \frac{\mathbf{R}_c \times \mathbf{B}}{B^2}. \tag{1.18}$$

Again, curvature drifts depend on the electric charge and therefore can generate currents and charge separation in plasmas.

1.3 Fluid Theory

In fluid theory, a plasma is characterized by macroscopic plasma parameters such as the number density n, kinetic temperature T and flow velocity $\mathbf{u}$. The evolution of these parameters are obtained by taking moments of the Vlasov equation [*Vlasov*, 1968]

$$\frac{\partial f(\mathbf{x}, \mathbf{u}, t)}{\partial t} + \mathbf{u} \cdot \nabla_{\mathbf{x}} f(\mathbf{x}, \mathbf{u}, t) + \frac{q}{m} (\mathbf{E} + \mathbf{u} \times \mathbf{B}) \cdot \nabla_{\mathbf{u}} f(\mathbf{x}, \mathbf{u}, t) = 0, \tag{1.19}$$

which is the kinetic equation for a collisionless plasma. Here $f(\mathbf{x}, \mathbf{u}, t)$ is the seven-dimensional phase space distribution function, $\nabla_{\mathbf{x}}$ is the vector derivative with respect to the position vector, and $\nabla_{\mathbf{u}}$ is the vector derivative with respect to the velocity vector. By taking the zeroth order moment of the Vlasov equation we obtain

$$\frac{\partial n_\alpha}{\partial t} + \nabla \cdot (n_\alpha \mathbf{u}_\alpha) = 0, \tag{1.20}$$

the continuity equation for particle species α. Equation (1.20) implies that in the absence of sources the number density is conserved during the motion of the fluid. Taking the first order moment of the Vlasov equation (1.19) gives the momentum equation

$$n_\alpha m_\alpha \left[\frac{\partial \mathbf{u}_\alpha}{\partial t} + (\mathbf{u}_\alpha \cdot \nabla)\mathbf{u}_\alpha \right] = -\nabla \cdot \mathbf{P}_\alpha + q_\alpha n_\alpha (\mathbf{E} + \mathbf{u}_\alpha \times \mathbf{B}), \tag{1.21}$$

where $\mathbf{P}$ is the pressure tensor. It is equivalent to the Navier-Stokes equations on including an electromagnetic Lorentz force but neglecting dissipative effects.

The motions of charged particles are also the source of the fields $\mathbf{E}$ and $\mathbf{B}$ themselves. The fundamental equations that govern the evolution of the electric and magnetic fields in a plasma are given by Maxwell's equations,

$$\nabla \times \mathbf{E} = -\frac{\partial \mathbf{B}}{\partial t}, \tag{1.22a}$$

$$\nabla \times \mathbf{B} = \mu_0 \mathbf{j} + \mu_0 \epsilon_0 \frac{\partial \mathbf{E}}{\partial t}, \tag{1.22b}$$

$$\nabla \cdot \mathbf{E} = \frac{\rho}{\epsilon_0}, \tag{1.22c}$$

$$\nabla \cdot \mathbf{B} = 0, \tag{1.22d}$$

where μ_0 is the permeability of free space and the source terms ρ and $\mathbf{j}$ are the charge density and current density, respectively. In fluid theory, ρ and $\mathbf{j}$ are defined as

$$\rho = e(n_i - n_e), \tag{1.23a}$$

$$\mathbf{j} = e(n_i \mathbf{u}_i - n_e \mathbf{u}_e). \tag{1.23b}$$

Taking the second order moment of the Vlasov equation results in the *heat transport equation*

$$\frac{3}{2} n_\alpha k_B \left(\frac{\partial T_\alpha}{\partial t} + \mathbf{u}_\alpha \cdot \nabla T_\alpha \right) = P_\alpha \nabla \cdot \mathbf{u}_\alpha - \nabla \cdot \mathbf{Q}_\alpha - (\mathbf{P}'_\alpha \cdot \nabla) \cdot \mathbf{u}_\alpha, \tag{1.24}$$

where P is the scalar pressure, $\mathbf{Q}$ is the heat flux vector, and $\mathbf{P}'$ denotes the stress tensor part of the full pressure tensor $\mathbf{P}$. However, (1.24) does not close the system of equations since the evolution of the heat flux vector is not known. Taking another order moment of the Vlasov equation will only introduce a next order quantity to be determined. Therefore, these sets of equations are typically truncated by introducing an equation of state and assuming an isotropic distribution which yields an isotropic pressure and zero heat flux. For an isotropic pressure tensor, there are two important equations of states. The most simple equation of state is the ideal gas law under isothermal conditions.

$$P_\alpha = n_\alpha k_B T_\alpha. \tag{1.25}$$

The other case deals with time variations that are so fast that no heat exchange can occur, corresponding to the adiabatic equation of state

$$P_\alpha n_\alpha^{-\gamma} = C. \tag{1.26}$$

Here C is a constant and γ is the specific heat ratio, which for an ideal 3-D collisionless plasma is $\gamma = 5/3$.

1.4 Magnetohydrodynamic Theory

Magnetohydrodynamics is a one fluid theory which combines two separate electron and ion fluids into a single fluid [*Kivelson and Russell*, 1995]. A fully ionized plasma has electrons with mass m_e and charge $q_e = -e$, and ions of mass m_i and charge $q_e = Ze$. For simplicity we assume the ions are protons and hence $Z = 1$. New fluid variables which are combinations of the densities and velocities of the individual components are introduced:

$$n = \frac{m_e n_e + m_i n_i}{m_e + m_i} \tag{1.27a}$$

$$m = m_e + m_i = m_i\left(1 + \frac{m_e}{m_i}\right) \tag{1.27b}$$

$$\mathbf{u} = \frac{m_e n_e \mathbf{u}_e + m_i n_i \mathbf{u}_i}{m_e n_e + m_i n_i}. \tag{1.27c}$$

Also, one typically assumes quasineutrality which demands that the charge density $\rho = 0$, which from (1.23a) yields $n = n_e = n_i$.

From these assumptions and (1.20) we can derive the MHD continuity equation

$$\frac{\partial n}{\partial t} + \nabla \cdot (n\mathbf{u}) = 0. \tag{1.28}$$

Note that the continuity equation in this form no longer discriminates between particle species. The MHD momentum equation is derived by adding proton and electron forms of (1.21) and using the definitions (1.27) of the new fluid variables. We take advantage of the smallness of the electron mass $m_e \ll m_i$ to arrive at the equation

$$nm\left[\frac{\partial \mathbf{u}}{\partial t} + (\mathbf{u}\cdot\nabla)\mathbf{u}\right] = -\nabla P + \rho\mathbf{E} + \mathbf{j}\times\mathbf{B}, \tag{1.29}$$

where $P = P_e + P_i$. To determine the current density $\mathbf{j}$ in (1.29), we need to introduce the *generalized Ohm's law*. It is obtained by subtracting the fluid momentum equations (1.21) for the electrons and ions and introducing a resistivity η due to effective particle collisions via fluctuations in $\mathbf{E}$ and $\mathbf{B}$ via a resistive term $\eta\mathbf{j}$ to give

$$\mathbf{E} + \mathbf{u} \times \mathbf{B} = \eta\mathbf{j} + \frac{1}{ne}\mathbf{j} \times \mathbf{B} - \frac{1}{ne}\nabla P_e + \frac{m_e}{ne^2}\frac{\partial \mathbf{j}}{\partial t}. \tag{1.30}$$

Typically, the generalized Ohm's law can be approximated by omitting different terms [*Baumjohann and Treumann*, 1999]. Finally, the MHD energy continuity equation is given by

$$\begin{aligned} &\frac{\partial}{\partial t}\left(\frac{1}{2}nmu^2 + \frac{P}{\gamma - 1} + \frac{B^2}{2\mu_0} + \frac{1}{2}\epsilon_0 E^2\right) + \\ &\qquad \nabla \cdot \left(\frac{1}{2}nmu^2\mathbf{u} + \frac{\gamma}{\gamma - 1}P\mathbf{u} + \frac{1}{\mu_0}\mathbf{E} \times \mathbf{B}\right) = 0. \end{aligned} \tag{1.31}$$

1.5 Plasma Waves

A variety of rich wave phenomena can be supported in plasmas. The approximations made in MHD require the time scales for variation to be larger than the ion time scales. Hence equations (1.28) to (1.31) are valid for wave modes in the low frequency regime, which are referred to as MHD waves. These wave modes are derived by linearizing the MHD equations and assuming a plane wave solution $e^{-i(\omega t - \mathbf{k}\cdot\mathbf{x})}$ where ω and $\mathbf{k}$ are the wave angular frequency and wave vector, respectively. It is convenient to express the set of linear equations in the fluid displacement vector ξ which is defined such that its time derivative is the fluid velocity, i.e. one writes $\mathbf{u} = -i\omega\xi$. Doing this and making the replacements $\partial/\partial t \rightarrow i\omega$ and $\nabla \rightarrow i\mathbf{k}$ we obtain (e.g. *Melrose* [1986])

$$\Gamma_{ij}\xi_j = 0, \tag{1.32}$$

where the matrix of coefficients is given as

$$\Gamma_{ij} = \omega^2\delta_{ij} - k^2c_s^2\kappa_{\mathbf{i}}\kappa_{\mathbf{j}} - k^2v_A^2\left[\kappa_i\kappa_j - \cos\theta(\kappa_i b_j + b_i\kappa_j) + \cos^2\theta\delta_{ij}\right] \tag{1.33}$$

and δ_{ij} is the Dirac delta function, $\mathbf{b} = \mathbf{B}/B$ is the normalized magnetic field vector, $\kappa = \mathbf{k}/k$ is the normalized wave vector, and θ is the angle between the wave vector $\mathbf{k}$ and the magnetic field $\mathbf{B}$. The parameter c_s is the familiar sound speed in an adiabatic gas, given by

$$c_s = \left(\frac{\gamma k_B T}{m_i}\right)^{1/2}, \tag{1.34}$$

and v_A is the Alfvén speed given by

$$v_A = \frac{B}{\sqrt{\mu_0 n m_i}}. \tag{1.35}$$

The dispersion relations for MHD waves are found by setting the determinant of (1.33) equal to zero, i.e.,

$$\Delta\Gamma_{ij} = 0. \tag{1.36}$$

The first wave mode that will be discussed is called the Alfvén wave which has a linear dispersion relation

$$\omega = k v_A |\cos\theta|. \tag{1.37}$$

Alfvén waves are shear waves which rely on the magnetic pressure of the plasma as a restoring force. The speed at which Alfvén waves propagate is the Alfvén speed v_A and is the speed at which magnetic signals propagate in a plasma with negligible thermal pressure.

Two additional solutions obtained from the general dispersion relation are referred to as the fast (+) and slow (−) magnetosonic waves. Their phase speed satisfy the following relation

$$v_\pm^2 = \frac{1}{2}\left(v_A^2 + c_s^2\right) \pm \frac{1}{2}\left[(v_A^2 + c_s^2)^2 - 4v_A^2 c_s^2 \cos^2\theta\right]^{1/2}. \tag{1.38}$$

To interpret the nature of these waves let us consider taking the limit as c_s goes to zero. Observe that the phase speed v_- of the slow magnetosonic mode goes to zero whereas the fast magnetosonic wave has the dispersion relation

$$\omega = k v_A. \tag{1.39}$$

This shows us that the fast mode is in fact the Alfvén wave being modified by contributions from the thermal pressure. Taking another limiting case where $c_s \ll v_A$ reduces the dispersion relation for the slow mode to

$$\omega \simeq k c_s^2 \cos\theta. \tag{1.40}$$

Thus slow modes are sound waves modified by the presence of a magnetic field.

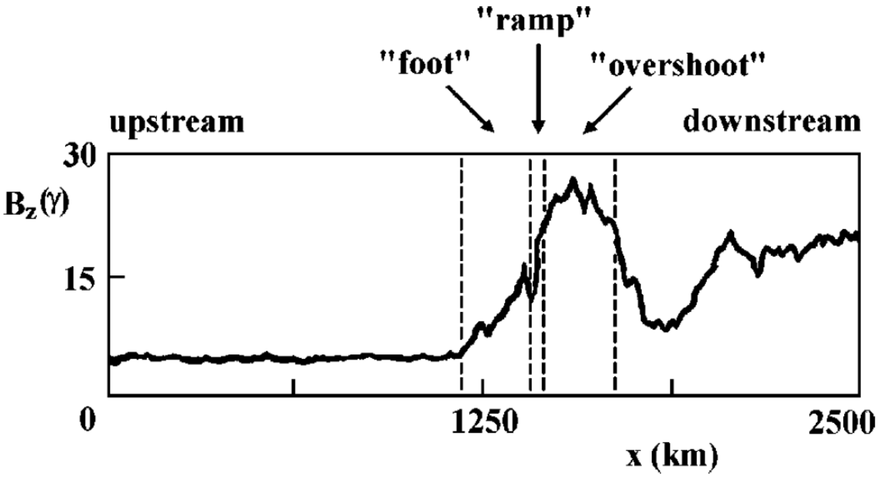

Figure 1.1: An example of a shock where regions such as the shock foot, ramp and overshoot are defined [*Wu et al.*, 1984].

1.6 Shocks

In a gas or neutral fluid, any disturbance causes a wave to propagate through the fluid at the speed of sound c_s. If the cause of the disturbance is moving slower than the speed of sound, then the wave will propagate ahead of the disturbance and the medium has time to respond to it. However, if the source of the disturbance moves faster than the speed of sound, then it will eventually overtake the wave-front with the result that the fluid experiences a sudden, non-adiabatic, change of state. This is known as a shock wave [*Tidman and Krall*, 1971; *Greenstadt and Fredricks*, 1979]; an example of a simulated shock wave is in Figure 1.1. Shocks are nonlinearly steepened waves which involve irreversible processes, such as the conversion of kinetic energy into thermal energy and the creation of entropy at the shock transition.

In a collisionless plasma, the collisional coupling between molecules is absent and so plasma waves are important for the transfer and dissipation of energy and momentum. There are numerous examples of shocks in space physics and astrophysics [*Tsurutani and Stone*, 1985]. Shocks surround planets with magnetospheres, appear in supernovae explosions, and are created in front of coronal mass ejections (CME) from the solar corona. One of the most widely studied example is the Earth's bow shock [*Kivelson and Russell*, 1995], which forms through the interaction between the supersonic solar wind and the Earth's magnetosphere; its location in the solar-terrestrial environment is shown in Figure

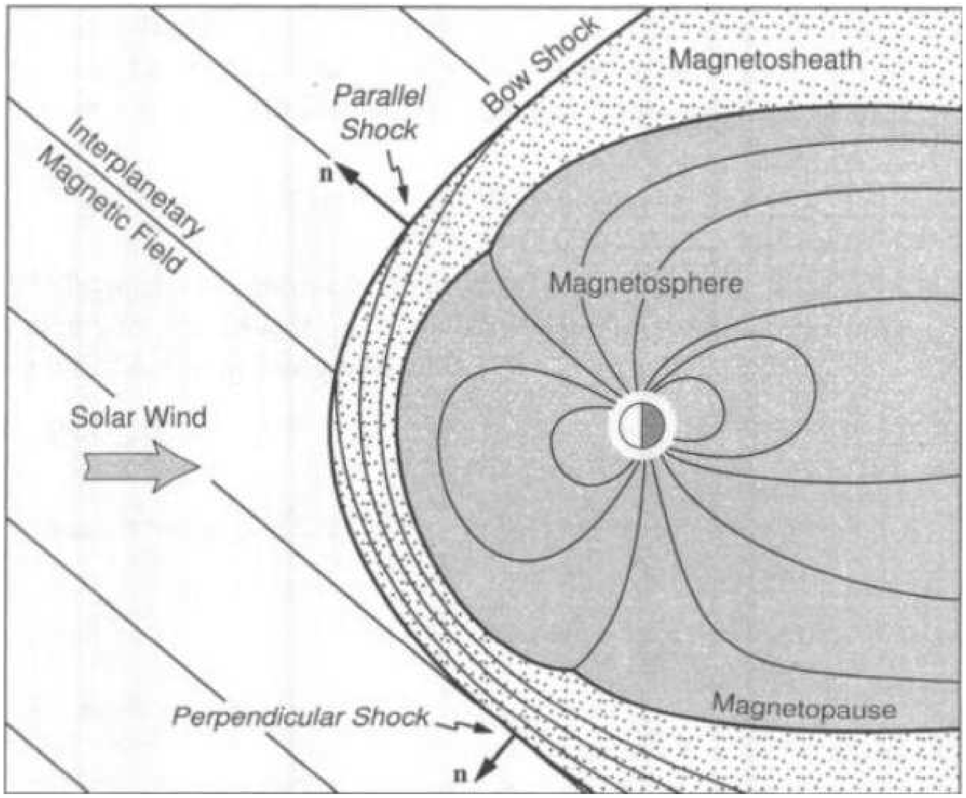

Figure 1.2: The interaction between the supersonic solar wind and the terrestrial magnetic field creates the Earth's bow shock, which is well described as a parallel, perpendicular, quasiparallel, or quasiperpendicular shock in different locations [*Baumjohann and Treumann*, 1999].

1.2. As the solar wind encounters the magnetosphere it is slowed and deflected at the bow shock, giving the parabolic shaped surface of the bow shock seen in Figure 1.2. The bow shock is a fast mode shock since the density and magnetic field strength both increase as the solar wind traverses through, as explained more below.

1.6.1 The Rankine-Hugoniot relations

The *jump conditions* or the *Rankine-Hugoniot relations* seeks to relate properties of the shocked downstream medium to the unshocked fluid in the upstream region (Figure 1.3). The Rankine-Hugoniot relations are derived from the conservation of mass, momentum, energy, and normal magnetic field and tangential electric field [*de Hoffmann and Teller*, 1950; *Tidman and Krall*, 1971; *Kennel et al.*, 1985]. For a magnetized plasma, three independent variables are needed to define these conditions. They are the Alfvén Mach number M_A, the angle between the shock normal direction and the upstream magnetic field θ_{Bn} and the plasma beta β. The Alfvén Mach number is the ratio between the upstream speed of the fluid and the Alfvén speed (1.35)

$$M_A = \frac{u}{v_A}. \tag{1.41}$$

The plasma beta describes the relative importance of the thermal pressure P_{th} and magnetic pressure $P_B = B^2/2\mu_0$ on the plasma dynamics and is defined as

$$\beta = \frac{P_{th}}{P_B} = \frac{2\mu_0 P_{th}}{B^2}. \tag{1.42}$$

On eliminating all downstream variables and introducing the three independent variables given above, the Rankine-Hugoniot relations lead to the following equation [*Melrose*, 1986]:

$$\begin{aligned}&\left(\frac{aM_A^2}{r} - \beta\right)\left(\frac{M_A^2}{r} - \cos^2\theta_{Bn}\right)^2 - \\ &\qquad \frac{M_A^2}{r}\sin^2\theta_{Bn}\left[\frac{M_A^2}{r}\left(a - \frac{1-r}{2}\right) - a\cos^2\theta_{Bn}\right] = 0,\end{aligned} \tag{1.43}$$

where $a = \frac{1}{2}[\gamma + 1 - r(\gamma - 1)]$ and the density compression ratio r across the shock is

$$r = \frac{n_2}{n_1}. \tag{1.44}$$

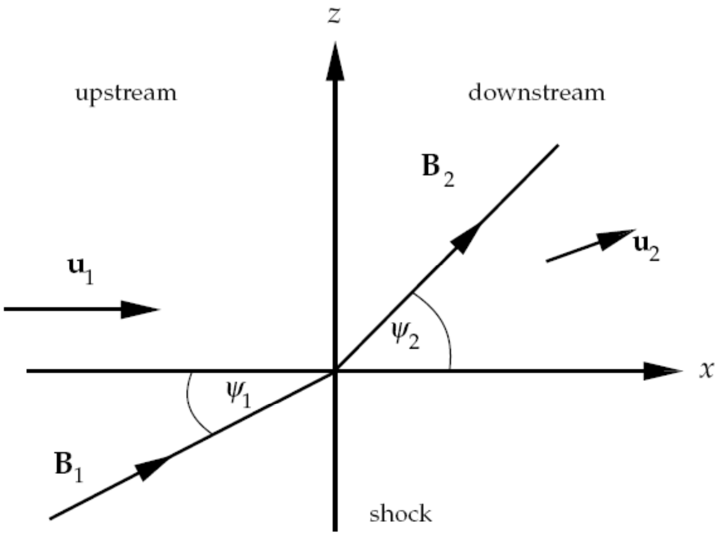

Figure 1.3: The shock normal frame where boundary of the shock is perpendicular to the upstream fluid velocity. Subscripts one and two denote upstream and downstream regions respectively [*Ball and Melrose*, 2001].

Subscripts 1 and 2 denote upstream and downstream quantities respectively. Equation (1.43) supports a wide range of different solutions, not all of which are shocks. In general, (1.43) is cubic in M_A^2 and hence has three solutions. On taking the limit as $r \rightarrow 1$, (1.43) reduces to the dispersion equation for MHD waves (1.36). Thus the three solutions are classified as Alfvénic, fast or slow mode shocks according to the MHD wave modes derived previously.

In space physics and astrophysics, the fast mode shock is by far the most frequently observed type of shock [*Stone and Tsurutani*, 1985] and will be discussed here. The fast shock corresponds to the fast magnetosonic wave mode after evolving to large amplitude. In a fast shock, the magnetic field strength, pressure and number density all increase across the shock transition. Depending on the value of θ_{Bn}, shocks can be classified as parallel ($\theta_{Bn} = 0°$), perpendicular ($\theta_{Bn} = 90°$) or oblique shocks ($0° < \theta_{Bn} < 90°$). We refer to shocks with normals close to the perpendicular and parallel directions (relative to B_1) as quasiperpendicular and quasiparallel, respectively.

Figure 1.4 shows the evolution of the magnetic profile as a function of θ_{Bn}. Low Mach-number quasiperpendicular shocks are usually *laminar* shocks because they have a smooth transition from upstream conditions to downstream conditions [*Russell et al.*, 1982; *Livesey et al.*, 1982]. Quasiparallel shocks typically have a turbulent magnetic field profile with short wavelength oscilla-

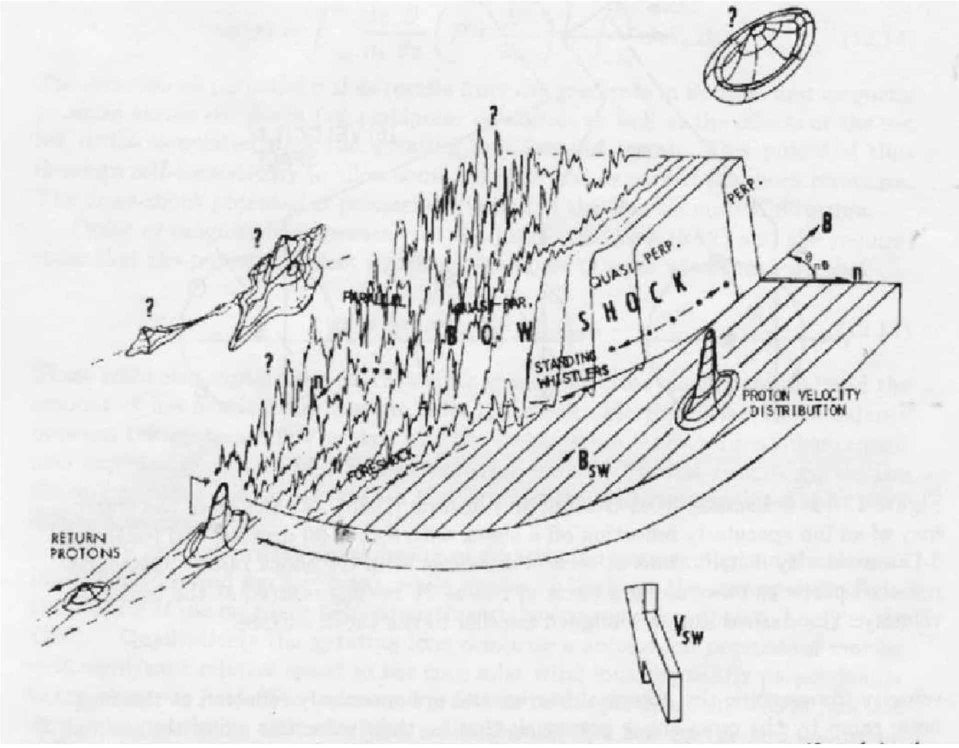

Figure 1.4: A schematic illustration of the evolution of a turbulent parallel shock to a laminar perpendicular shock [*Greenstadt and Fredricks*, 1979].

tions appearing before and after the shock [*Gosling et al.*, 1982; *Burgess*, 1989; *Winske et al.*, 1990].

In the high-Mach number limit, $M_A \gg 1$, the solution of (1.43) is $a = 0$ which means the compression ratio satisfies

$$r = \frac{\gamma + 1}{\gamma - 1}. \tag{1.45}$$

For a collisionless ideal plasma with $\gamma = 5/3$ (1.45) yields a maximum $r = 4$. The magnetic enhancement ratio B_2/B_1 is also equal to the compression ratio, $B_2/B_1 = r$, and therefore cannot be arbitrarily large. However, both the downstream pressure and temperature can increase without bound since the pressure jump is (e.g. [*Tidman and Krall*, 1971])

$$\frac{P_2}{P_1} = 1 + \frac{2M_{\mathrm{A}}^2}{\beta}\left(1 - \frac{1}{r}\right) + \frac{1 - r^2}{\beta}, \tag{1.46}$$

which scales with M_A^2.

1.6.2 Simulations

Three types of simulation codes are typically used to model shock phenomena in collisionless plasmas, with the choice depending on the physical problem. Each method varies in the type of physics included or neglected.

The first method models a plasma as a MHD fluid using the MHD equations (1.27)–(1.31), Maxwell's equations (1.22), and an equation of state [see e.g., *Ledvina et al.*, 2008]. This is a popular approach for modelling large scale phenomena in the solar-terrestrial environment or interplanetary medium [*Wu et al.*, 2001; *Ofman*, 2009].

The second method is referred to as the particle-in-cell (PIC) model and relies on tracking each individual particle, electrons and ions, in phase space $(\mathbf{x}, \mathbf{v}, t)$ [see e.g., *Pritchett*, 2003]. A finite mass ratio $\mu = m_i/m_e$ is used that is generally much lower than the real value due to computational limits. The spatial resolution of PIC codes must be on the order of the electron gyroradius or Debye length, with time resolutions greater than the minimum of the inverse electron cyclotron or inverse electron plasma periods in order to resolve the electron physics.

The third method is a hybrid of the two previous models. The standard hybrid model treats ions as inertial particles but electrons as a massless fluid [see e.g., *Winske et al.*, 2003]. Hence all space and time scales for the electrons are neglected. The evolution of the macroscopic fields and parameters of the electrons are governed by fluid equations but ion trajectories are determined by integrating their equations of motion. Hybrid codes model phenomena that occur on shorter spatial-temporal scales than can be treated by MHD and yet do not resolve processes that occur on electron scales [*Winske et al.*, 2003]. The relevant distance and time scales are then the ion gyroradius and the inverse ion gyrofrequency, respectively.

1.7 Ion Dynamics

1.7.1 Specular Reflection

Quasiperpendicular shocks can possess a variety of spatial structures depending on M_A and β. Figure 1.1 shows spacecraft observations of a high M_A shock and indicates the different spatial regions. These structures arise from considering the kinetic aspects of the shock and deal with the microphysics of the system [*Gosling and Robson*, 1985]. The *ramp* of the shock corresponds to the (ideally) discontinuous shock front. Solar wind ions and electrons encountering the abrupt change in the magnetic field will have differing gyroradii. The electrons complete numerous gyrations as they pass the shock ramp. However, ions with a much larger gyroradius than the ramp see it as an abrupt change in their motion but can penetrate deeper into the ramp. This creates a charge separation between the ions and electrons, which generates an electric field which points in the direction of the shock normal. This self-consistent electrostatic field is often referred to as the *cross-shock potential* [*Gosling and Robson*, 1985]: it slows and deflects ions but acts to accelerate and capture electrons downstream.

Ions with normal kinetic energy less than the cross-shock potential are slowed and reflected; this process is historically known as specular reflection [*Gosling et al.*, 1982; *Leroy*, 1983] and the magnetic force is often neglected in this idealization of the reflection. These ions then gyrate half a gyroradius upstream before being convected back through the shock. This localized region of gyrating ions in front of the shock ramp establishes a current which in turn generates a "bump" in the magnetic field. This localized perturbation in the magnetic field upstream of the shock ramp is known as the *foot* of the shock. Ideally, the combination of specular reflection and the $\mathbf{E}\times\mathbf{B}$ drift downstream causes the reflected ions to develop a new gyrospeed equal to twice the perpendicular component of the solar wind velocity [*Gosling et al.*, 1982]. As the foot is intrinsically associated with the gyration of an upstream reflected ion, the length of the foot is typically about of half an ion gyroradius. Ion reflection causes a notable difference in ion and electron temperatures further downstream and has been observed at the Earth's bow shock [*Sckopke et al.*, 1983].

In the region just behind the shock ramp, the gyrating specularly reflected ions at first amplify the local magnetic field, causing it to "overshoot" the predictions of the Rankine-Hugoniot conditions. This amplified magnetic field is known as the *overshoot* of the shock. Further downstream the gyrating ions cause undershoot-overshoot oscillations before settling down to an average downstream value. Although the overshoot can violate the Rankine-Hugoniot prediction [*Tiu et al.*, 2011], the shock transition must satisfy the jump conditions on a macroscopic level (meaning averaged over the downstream region).

Coroniti [1970] showed that for a fast mode shock if resistivity is the only dissipation process, then the shock cannot remain steady above a critical Mach number M_A^*. Shocks having Mach-numbers above and below the critical Mach number are called *subcritical* and *supercritical*, respectively. He speculated that ion reflection becomes important for supercritical shocks $M_A > M_A^*$, providing the necessary dissipation for the shock to remain steady. Since ion reflection is responsible for the creation of the foot and overshoot features at quasiperpendicular shocks, the appearance of these structures is widely used as an operational definition of a supercritical shock. Subcritical shocks which do not possess foot or overshoot features closely resemble the ramp-only shock profiles of an ordinary gas. Put another way, subcritical shocks typically have a smooth laminar monotonic transition from upstream to downstream. A parametric survey by *Edmiston and Kennel* [1984] found that the critical Mach-number is $M_A^* \sim 2.7$ for $\theta_{Bn} = 90°$ and decreases with decreasing θ_{Bn}. The Earth's bow shock has values of $M_A \sim 1 - 10$ and so both subcritical and supercritical shocks have been observed [*Russell et al.*, 1982; *Livesey et al.*, 1982; *Scudder et al.*, 1986].

Ion reflection also plays an important role in the heating of the downstream plasma [*Biskamp and Welter*, 1972; *Forslund et al.*, 1984; *Burgess et al.*, 1989; *Sckopke et al.*, 1990; *Gedalin*, 1997]. In an ordinary fluid, heating or dissipation is due to the viscosity provided by collisions between molecules. However, in a collisionless plasma the source of shock heating is not so obvious, since collisions are unimportant, and remains a major problem in space physics today [*Lembège et al.*, 2004; *Bale et al.*, 2005; *Krasnoselskikh et al.*, 2013]. Indeed, while the total amount of heating must be prescribed by the Rankine-Hugoniot relations, the heating may be due to a single process or to multiple processes.

One possible heating mechanism involves the production of the so called "ring" distribution downstream [*Sckopke et al.*, 1983, 1990]. Specularly reflected ions which are accelerated by the convective electric field upstream are predicted to emerge downstream with a perpendicular speed of twice the incoming fluid speed [*Gosling et al.*, 1982; *Burgess et al.*, 1989], i.e. $v_\perp \simeq 2u$. This eventually forms the ring distribution downstream which can be the source of free energy for waves to grow and scatter particles, generating dissipation and heat. Figure 1.5 shows observational evidence for a ring distribution at a supercritical shock from ISEE-2 spacecraft data [*Sckopke et al.*, 1983]. Contour plots of the upstream and downstream ion distribution in perpendicular velocity phase space clearly show some particles with larger perpendicular speed than the thermal core. Qualitatively, we would then expect most of the downstream ion temperature to reside with the ion ring population [*Sckopke et al.*, 1990].

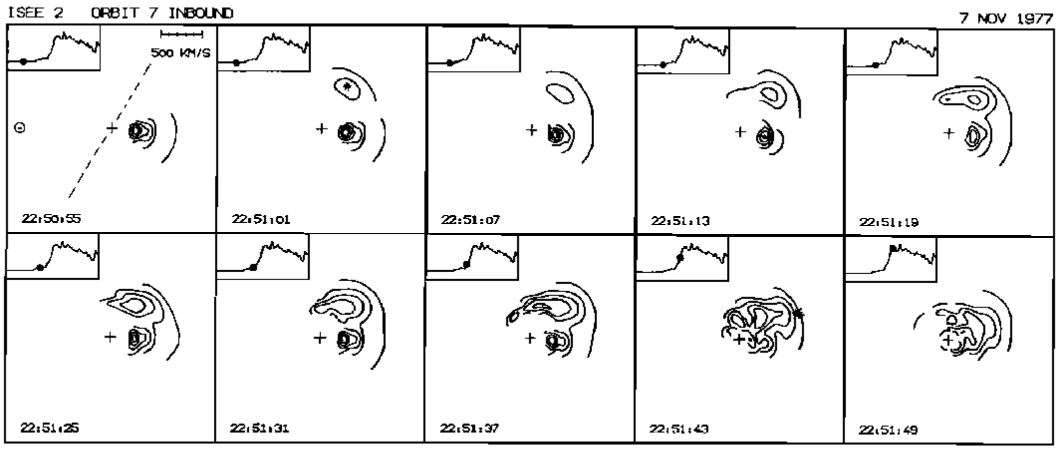

Figure 1.5: Contour plots of the ion distribution in perpendicular velocity phase space as a function of time for an inbound shock crossing observed by ISEE-2 [*Sckopke et al.*, 1983].

1.7.2 Acceleration and Energization

Shocks are efficient instruments by which particles undergo acceleration and energization. Several theories have been proposed on how electrons and ions are accelerated at shocks; in this Section we focus on ion acceleration.

Shock drift acceleration (SDA) [see e.g., *Armstrong et al.*, 1985] involves ions gaining energy by drifting parallel to the convective electric field by ∇B or curvature drifts for extended periods of time. (Electrons gain energy by drifting anti-parallel to the convective electric field.) Transmitted particles can also gain energy through this mechanism but the largest energy gains occur for reflected particles. In its simplest form SDA predicts that the maximum energy increase for a reflected particle is

$$\frac{E_{\max}}{E} = \frac{1+(1-1/r)^{1/2}}{1-(1-1/r)^{1/2}} \tag{1.47}$$

which for a strong shock with $r = 4$ means a reflected particle can only increase its original energy by a maximum factor of 13.93 [*Ball and Melrose*, 2001]. Shock drift acceleration is most efficient for thin shocks [*Lever et al.*, 2001] where the ramp thickness L_r is much smaller than the ion inertial length $\lambda_i = v_A\Omega_{ci}$, i.e. $L_r \ll \lambda_i$. Indeed, Cluster spacecraft measurements of the ramp thickness at the terrestrial bow shock suggest L_r is on the order of the electron inertial length $\lambda_e = c/\omega_{ce} \ll \lambda_i$ [*Mazelle et al.*, 2010; *Hobara et al.*, 2010]. Under these conditions, ions can be reflected multiple times off the shock which is known as multiply reflected ion (MRI) acceleration [*Zank et al.*, 1996] or "shock surfing" [*Lee et al.*, 1996]. With each reflection the particle is accelerated and so can reach energies several to many times larger than the incoming ram energy [*Zank et al.*, 1996; *Lee et al.*, 1996].

Diffusive shock acceleration (DSA) [see e.g., *Lee and Fisk*, 1982] is a form of first order Fermi acceleration associated with particles being scattered by waves on either side of the shock. Since the fluid velocity decreases across the shock, a particle travelling upstream from the downstream region, or vice-versa, will approach the scattering centers of the waves head on and so cause the particle's energy to increase. Provided that particles cross the shock many times, which is highly likely since scattering is a diffusive process, DSA is an efficient acceleration mechanism. Eventually particles diffuse away from the shock. Quantitatively, one can show that diffusive shock acceleration leads to a downstream spectrum of accelerated particles that follows a power law distribution $f(p) \propto p^b$, where b is the power-law index and depends solely on the compression ratio of the shock: $b = 3r/(r-1)$ [*Lee and Fisk*, 1982].

1.8 Shock Reformation

So far we have only considered shock structures that are stationary in time. However, early laboratory experiments of collisionless shock waves in a plasma-wind-tunnel showed nonstationary structures, oscillating with a time scale close to the ion gyroperiod [*Morse et al.*, 1972]. This phenomena is called *shock reformation* or *shock nonstationarity* [see e.g., *Bale et al.*, 2003; *Chapman et al.*, 2005; *Burgess et al.*, 2012; *Krasnoselskikh et al.*, 2013]. An example of a reforming shock from a numerical simulation is shown in Figure 1.6.

This dynamic shock behavior was suggested in early PIC simulations [*Biskamp and Welter*, 1972; *Leroy et al.*, 1982; *Lembège and Dawson*, 1987] and hybrid simulations [*Quest*, 1985; *Burgess*, 1989; *Winske et al.*, 1990] of high M_A shocks which showed spatial structures disappearing and reappearing on time scales close to the ion gyroperiod. *Quest* [1985] modelled a high $M_A \sim 22$, low $\beta = 0.1$, perpendicular shock using a 1-D hybrid simulation. He noted the ion reflection process was periodic, with intervals of 100% transmission and 100% reflection in the absence of electron resistivity [*Quest*, 1986]. Furthermore, the growing time-dependency of the shock was also evident with increasing M_A. *Lembège and Dawson* [1987] studied in detail the field patterns and ion dynamics of perpendicular supercritical shocks using a 1-D PIC simulation code.

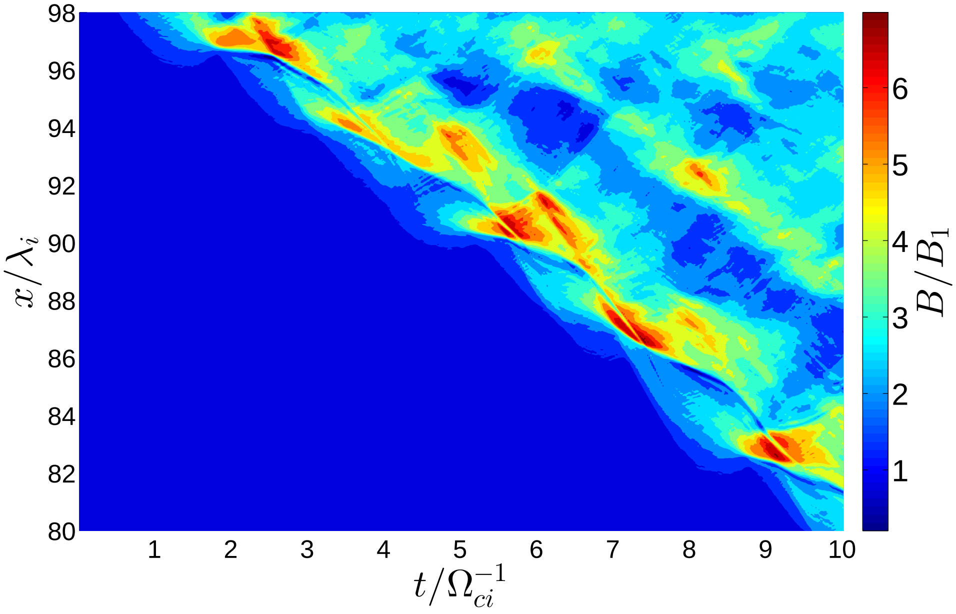

Figure 1.6: Contour plot of the spatial-temporal normalized magnetic field B/B_1 of a reforming shock in our 1-D hybrid simulation with shock parameters $M_A \sim 6.1$, $\beta_e = \beta_i = 0.5$, and $\theta_{Bn} = 85°$.

They found successive stages of ion acceleration-trapping-detrapping in their simulations. The dominating magnetic field structures of the trailing wave train, foot, and ramp were also shown to have length scales dictated by the ion dynamics at the shock front.

Lembège and Savoini [1992] confirmed and extended these results with 2-D PIC simulations of supercritical perpendicular shocks. They found evidence for a critical angle θ_r, below which reformation in their simulations would disappear. They argued that dispersive effects which become stronger for angles further away from $\theta_{Bn} = 90°$ stabilize the foot and overshoot and hence any nonstationary effects.

Yuan et al. [2007] examined the dynamics of low beta ($\beta = 0.05$) high M_A ($\sim 4-5$) quasiperpendicular ($\theta_{Bn} = 87°$) shocks using a 1-D hybrid simulation with electron mass and pressure tensor effects. They found the shock reformed with a period of $1.8\Omega_{ci}^{-1}$ and the addition of electron dissipation led to strong ion thermalization and phase space mixing between upstream incoming and reflection ions via plasma wave interactions in the foot.

Evidence for shock reformation occurring in nature has so far been limited. For a single-spacecraft shock encounter, the challenge remains in separating temporal fluctuations to spatial variations observed in the shock structure. So far most evidence for reformation has been from the Cluster mission [*Krasnoselskikh et al.*, 2013], a group of four spacecraft which fly in tetrahedron formation around Earth. This makes it suitable for studying nonstationary effects by comparing magnetic and electric field data between each four spacecraft but requires careful analysis of the shock motion and location. Here we outline previous evidence for shock reformation, most of which are based from Cluster spacecraft data.

Horbury et al. [2001] analyzed magnetic field data of a low $\beta \approx 0.1$ high $M_A \approx 5$ quasiperpendicular $\theta_{Bn} \approx 89°$ terrestrial shock. By combining data from the four spacecraft they estimated the bow shock orientation and velocity. Thus by examining the residual magnetic field variations, i.e. through removing the average field profile from each synchronized time series, they concluded that compressive temporal fluctuations of significant amplitude were observed in the foot which are not phase standing and are not present in the ramp. *Lobzin et al.* [2007] also analyzed Cluster spacecraft data of a high $M_A \simeq 5$ quasiperpendicular $\theta_{Bn} \approx 81°$ terrestrial shock. Their measurements of the magnetic field structure, spectra of electric field fluctuations, and ion distributions suggested a highly nonstationary shock. On the other hand, *Mazelle et al.* [2010] performed a statistical analysis of the ramp thickness L_r from 24 terrestrial close to perpendicular shocks with very similar upstream conditions observed between the four spacecraft. They found variation in ramp thickness between each four spacecraft, most being a few electron inertial lengths wide $L_r \sim \lambda_e = c/\omega_e$ but some reaching just under the ion inertial length $L_r \lesssim \lambda_i$. They interpreted the variability of the ramp scales, observed for the same upstream conditions, as a clear signature of reforming shocks. Recently, *Sundberg et al.* [2013] examined magnetic field measurements across a quasiparallel $\theta_{Bn} \sim 45°$ shock in Mercury's magnetosphere from MESSENGER spacecraft data. Over a 25-minute interval they documented a sustained period of magnetic field pulsations with an average period of 10 s which they interpreted as being caused by magnetic pressure fronts connected to a reforming shock.

There are many proposed causes of shock reformation and the suggested mechanisms vary between quasiparallel and quasiperpendicular shocks. One possible explanation involves the time-varying particle dynamics at the shock front, in particular due to ion reflection at quasiperpendicular shocks [*Leroy*, 1983; *Sckopke et al.*, 1983; *Quest*, 1986]. The idea is that when the density of the reflected ions is large enough the magnetic field at the upstream edge of the foot, where the reflected ions turn around, can ignite the emergence of a new shock foot [*Lembège and Dawson*, 1987]. This shock foot grows in amplitude until it becomes the new shock ramp and reflects ions itself, leaving the previous ramp to decay.

Wave-particle interactions are also a popular explanation for shock nonstationarity. *Matsukiyo and Scholer* [2003] investigated the modified two stream instability (MTSI) driven by the relative drift between electrons and ions across the magnetic field. They found evidence for MTSI in the foot region of supercritical quasiperpendicular shocks in 1-D PIC simulations with the real mass ratio $\mu = 1836$. The instability results in small scale vortices in $v_x - x$ phase space of the incoming ions in the foot and phase mixing between the incoming and specularly reflected ions. Subsequently, a new shock front is created at the upstream edge of the foot [*Scholer and Matsukiyo*, 2004]. *Matsukiyo and Scholer* [2006] extended their investigation to include the electron cyclotron drift instability (ECDI) [*Forslund et al.*, 1970] and Buneman instability [*Buneman*, 1958]. Nonetheless they concluded from their 2-D PIC simulation results that the most dominant instability was still MTSI.

Finally, *Krasnoselskikh et al.* [2002] suggested that shock reformation at quasiperpendicular shocks was associated with the nonlinear whistler wave being no longer balanced by the effects of the dispersion and dissipation. For oblique shocks the whistler wave train, which stands in front of the shock ramp, is an intrinsic feature of the shock structure. *Krasnoselskikh et al.* [2002] derived a theoretical Mach number, called the nonlinear whistler critical Mach number M_{nw}, above which the stationary nonlinear wave train cannot exist anymore within the shock front. The authors argued that $M_A = M_{nw}$ corresponds to the transition between stationary and nonstationary temporal behavior of the shock. Using 1-D PIC simulations they performed shocks with Mach numbers above and below M_{nw}, and confirmed the disappearance of the whistler wave train and the appearance of shock nonstationarity above this threshold. Recently, *Lembège et al.* [2009] recovered the occurrence and disappearance of the nonlinear whistler waves in both 2-D PIC and 2-D hybrid simulations.

Chapter 2

Evidence for Reformation of the Uranian Bow Shock: Hybrid Simulations and Comparisons with Voyager Data

[Published as D. Tiu *et al.*, *J. Geophys. Res.* 116, A04228 (2011)]

2.1 Abstract

The cyclic reformation of shock structures is still a major unresolved issue for collisionless shock physics. We investigate the Voyager 2 spacecraft's encounter with the Uranian bow shock and present detailed quantitative evidence that the bow shock was reforming. This evidence is based on finding very good agreement between Voyager observations of the Uranian bow shock and results from a standard 1-D hybrid simulation code run with similar plasma parameters. Specifically, the multiple large localized magnetic field enhancements $B/B_1 \sim 16$ observed downstream by Voyager 2, where $B_1 = 0.19$ nT is the upstream magnetic field, are quantitatively consistent with the reforming shock found in the simulation. Moreover, the variability and large enhancement factors for B and the number density, as well as the variations of the plasma velocity, and ion temperature over an almost 2-hour period including and after the shock crossing, are consistent with Voyager being very close to the reforming bow shock and with the Uranian bow shock receding planetwards with the spacecraft. Additional simulations show the magnetic overshoot factor to increase approximately linearly with Alfvén Mach number and to be robust against changes in magnetic field orientation (from quasiparallel to quasiper-

pendicular). These large overshoots may be important in applications involving particle acceleration and type II solar radio bursts. In addition, we estimate the effective numerical resistivity of our code by comparing simulations with varying applied resistivity. The estimated numerical resistivity found is consistent with estimates inferred from observations of Earth's bow shock by *Scudder et al.* [1986].

2.2 Introduction

A shock is a nonlinearly steepened wave, ideally with an abrupt discontinuity in the plasma parameters at the shock front [*Tidman and Krall*, 1971; *Russell*, 1985]. Shocks are present in numerous physical situations across multiple fields of physics such as space physics and astrophysics. They are important as they generate heat and entropy across the shock interface, accelerate particles, and signal supersonic flows and energy releases [*Tidman and Krall*, 1971; *Biskamp and Welter*, 1972; *Knock et al.*, 2001]. Planetary bow shocks are formed through the interaction between the Sun's supersonic solar wind and a planet's magnetosphere or ionosphere [*Russell*, 1985; *Scudder et al.*, 1986; *Bagenal et al.*, 1987].

The time-averaged jumps in plasma parameters across the macroscopic shock are governed by the Rankine-Hugoniot (R-H) conditions, which are based on time-invariance (neglect of time derivatives in the MHD equations) and the conservation of mass, energy, momentum, normal magnetic field, and tangential electric field across a planar discontinuity with infinitesimal thickness [*de Hoffmann and Teller*, 1950; *Tidman and Krall*, 1971; *Kennel et al.*, 1985; *Russell*, 1985]. In realistic applications the effects of waves, periodic variations, and other temporal and spatial variations are assumed to be removed by suitable temporal and spatial averaging of the upstream and downstream plasmas, and the R-H conditions are applied to the averaged upstream and downstream states [*Russell*, 1985]. The R-H conditions for a magnetized plasma are defined by three independent parameters: the Alfvén Mach number M_A, the angle θ_{Bn} between the upstream magnetic field and the shock normal, and the plasma beta β [*Tidman and Krall*, 1971]. In the limit of a high M_A shock, these relations predict a maximum magnetic enhancement (or compression) ratio of $B/B_1 = 4$ where B_1 is the upstream magnetic field strength [*Kennel et al.*, 1985; *Russell*, 1985].

The detailed structure of quasiperpendicular shocks ($45° < \theta_{Bn} < 90°$) include regions called the foot, ramp and overshoot. The shock ramp is often idealized as a discontinuous jump, and typically has an almost linear increase in magnetic field strength. The foot is the region in front of the ramp that is commonly associated with a mildly enhanced magnetic field and wave phenomena driven by ions specularly reflected (specular meaning the reversal of the normal component of the incoming ion velocity) by the cross-shock electrostatic potential and magnetic ramp. These ions gyrate upstream for half an ion gyroperiod and then move downstream. The overshoot is associated with the return of the gyrating ions, thereby enlarging the maximum magnetic field near the ramp. The gyrating ions cause additional undershoot-overshoot patterns in B downstream, which disappear as the ions are thermalized. The downstream plasma is expected to have the (fluid) characteristics predicted by the R-H conditions sufficiently far downstream from the shock.

Shock reformation is the cyclic variation of shock structures in time – specifically the shock foot, ramp, and overshoot form, disappear, and reform on time scales on the order of the upstream ion gyroperiod [*Morse et al.*, 1972; *Leroy et al.*, 1982; *Quest*, 1986; *Hellinger et al.*, 2002; *Krasnoselskikh et al.*, 2002; *Yuan et al.*, 2009]. One picture of reformation is that the gyrating ions reflected by the cross-shock potential generate a wave which steepens and grows to the magnitude of the previous shock, becoming the new shock while the previous ramp then disappears [*Quest*, 1986; *Lembège and Savoini*, 1992; *Krasnoselskikh et al.*, 2002; *Lembège et al.*, 2004]. An alternative picture is that the shock foot, ramp and overshoot do not disappear entirely, but rather fluctuate in strength about a characteristic equilibrium value [*Lembège et al.*, 2004]. This phenomenon of a cyclic shock structure has long been found in particle-in-cell (PIC) and hybrid simulations of collisionless plasmas. Reformation of quasiperpendicular shocks was reported in some early 1-D [*Biskamp and Welter*, 1972; *Leroy et al.*, 1982; *Lembège and Dawson*, 1987] and 2-D [*Lembège and Savoini*, 1992] PIC simulations. *Leroy et al.* [1982] performed 1-D hybrid simulations which showed temporal variations of the magnetic field strength on timescales of the order of the ion gyroperiod. In addition, they found that for $M_A = 10$ and $\beta_i = \beta_e = 0.1$ up to 30% of the incoming ions were periodically reflected. Simulations have indicated that the onset of reformation is typically associated with emerging shock structures such as the shock foot, the overshoot, and with large amplitude whistler waves [*Krasnoselskikh et al.*, 2002; *Hellinger et al.*, 2002, 2007; *Yuan et al.*, 2007; *Lembège et al.*, 2009].

Evidence for shock reformation occurring in nature has so far been limited. The earliest evidence of reformation is often attributed to *Morse et al.* [1972]

in the laboratory and [*Horbury et al.*, 2001] in space. *Morse et al.* [1972] interpreted low frequency fluctuations on the order of the ion cyclotron frequency upstream of the shock as evidence for cyclic reformation. *Horbury et al.* [2001] analyzed magnetic field data aboard the four Cluster spacecraft and pointed out that large amplitude fluctuations near and upstream of the ramp may be signatures of reformation or instead whistler waves. More recently *Lobzin et al.* [2007] found bursty ion reflection and quasiperiodic variations of Langmuir-like waves observed upstream of Earth's bow shock, both with periods of the order of Ω_{ci}^{-1}. These waves were speculated to be caused by bursts of electrons reflected off a nonstationary shock, as found in recent simulations [*Yuan et al.*, 2008a]. However, the observational evidence for shock nonstationarity is primarily in terms of temporal variations of plasma parameters on timescales of the ion gyroperiod.

To this end we provide strong evidence of shock reformation occurring in nature through direct analyses of the Voyager 2 spacecraft's data for the Uranian bow shock. This paper focuses on the very high magnetic compression ratios $B/B_1 \sim 20$ observed at the immediate shock ramp and for 2 hours downstream, much greater than the R-H predictions (which apply properly only to the final averaged downstream state and not the shock microstructure), found in both our 1-D hybrid simulations and the Voyager 2 data. Very good agreement between the simulations and observations is found for the magnetic field, plasma density, flow velocity, and temperature. Additional simulations address the magnitudes of the overshoots, progressing beyond the observations of *Livesey et al.* [1982] and *Russell et al.* [1982]. The localized magnetic compression (enhancement) factor increases linearly with M_A and is robust against changes in θ_{Bn}. This paper is organized as follows. In section 2 we examine and analyze Voyager 2 observations of the Uranian bow shock. Section 3 briefly outlines our simulation methods. Section 4 outlines our results and the evidence for shock reformation. Sections 5 and 6 discuss the results and conclude the paper, respectively.

2.3 Voyager 2 Data

Voyager 2 encountered the Uranian bow shock on 24 January 1986, under the conditions of high Alfvén Mach number ($M_A \sim 23$) and high plasma beta ($\beta \sim 3$) [*Bagenal et al.*, 1987]. Voyager 2 spacecraft was inbound to Uranus and moving close to the planet-Sun line, as shown in Figure 2.1 (reproduced

Table 2.1: Observed plasma parameters at Earth's bow shock as measured by ISEE 1 [*Scudder et al.*, 1986].

Parameter	**Up**	**Down**
n_e, cm^{-3}	9.87	32.2
θ_{Bn}, °	76.1 ± 4	
β_i	0.8	5.7
β_e	1.6	1.5
B, nT	5.49	0.7
v_A, km s^{-1}	37.8	67.1
M_A	7.7	1.1
f_{ci}, Hz	0.082	0.27

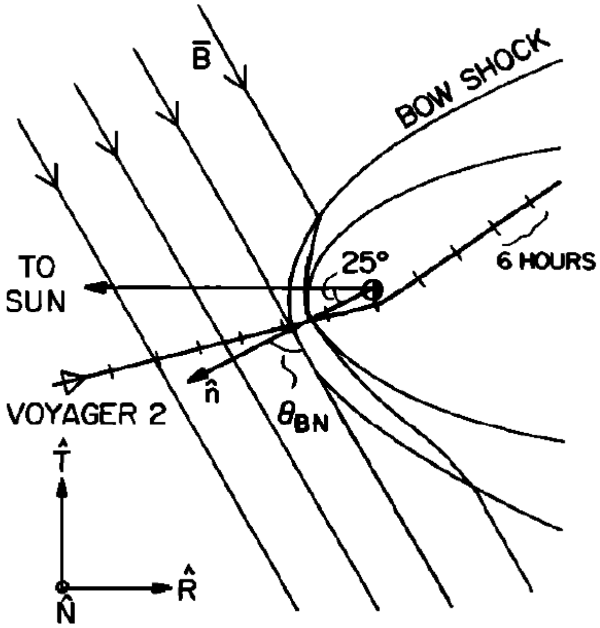

Figure 2.1: The trajectory of the Voyager 2 spacecraft at the Uranian bow shock crossing, reproduced from *Bagenal et al.* [1987]. The vector $\hat{n}$ is the shock normal. The heliographic coordinate system with unit vectors $\hat{R}$, $\hat{T}$ and $\hat{N}$ define a spherical polar coordinate system ($\hat{N}$ is out of the page).

from *Bagenal et al.* [1987]). The heliographic coordinate system is a spherical polar coordinate system defined by the set of unit vectors $(\hat{R}, \hat{T}, \hat{N})$, with $\hat{R}$ and $\hat{T}$ in the solar equatorial plane. Half an hour before the bow shock crossing, *Bagenal et al.* [1987] showed that the observed (averaged into 9.6 s samples) upstream magnetic field was $60.5° \pm 9°$ from the radial direction and $-26° \pm 6°$ from the $(\hat{R}, \hat{T})$ plane with a magnitude of 0.19 nT. Thus, with the spacecraft $\sim 25°$ from the Uranus-Sun line at the crossing, the angle between the shock normal and the magnetic field was $\theta_{Bn} \sim 85° \pm 9°$ [*Bagenal et al.*, 1987].

Figure 2.2 shows Voyager 2 observations of the magnetic field strength B, velocity components, plasma number density n, and ion and electron temperatures as a function of the spacecraft event time (SCET), as published by *Bagenal et al.* [1987]. The magnetic field samples have a 9.6 s cadence. On closer examination the regions typical for super-Alfvénic quasi-perpendicular shocks, such as the foot (near 0715-0720 SCET), ramp and overshoot (near 0725 and 0730 SCET), are identifiable. The magnetic field increased to a maximum value $B_{\max} \sim 3.2$ nT at the overshoot and oscillated strongly for ~ 1 hour, before settling down towards an average value of 0.7 nT [*Bagenal et al.*, 1987]. In addition, the velocity components and the ion temperature reached downstream values after only one overshoot-undershoot cycle, yet show considerable fluctuations immediately afterwards. Upstream parameters ($B_1 = 0.19$ nT, $n_1 = 5 \times 10^4$ m^{-3}) were taken at 0716 SCET, just before the magnetic field, density and temperature began to increase [*Bagenal et al.*, 1987].

Figure 2.3 shows the mean magnetic field, the direction angles (λ, δ), and the root mean squared (RMS) magnitude of the field about the mean during Voyager 2's encounter with the Uranian bow shock, using vector magnetic data with a cadence of 1.92 s. These data were obtained from the Planetary Data System (PDS). The angle λ is defined as $\tan \lambda = B_T / B_R$ and the angle δ defined as $\sin \delta = B_N / B$ (subscripts denote the magnitude of $\mathbf{B}$ in unit vectors). The magnetic angles exhibit high variability, particularly downstream from the shock. The variability of the magnetic field is evident upon examining the RMS magnitude, as large deviations from the mean are observed well past the nominal shock crossing.

Three major points are emphasized here. First, the maximum observed compression ratio $B_{\max}/B_1 \sim 16$, corresponding to the initial overshoot, exceeds by a factor of four the maximum value of 4 predicted by the R-H conditions. Note that this ratio is even greater for the 1.92 s averaged data set, with $B_{\max}/B_1 \sim 25$. Second, the field increases multiple times up to values near $B_{\max}$ for ~ 1.5 hours after the initial shock crossing. Peaks near $B_{\max}$ are

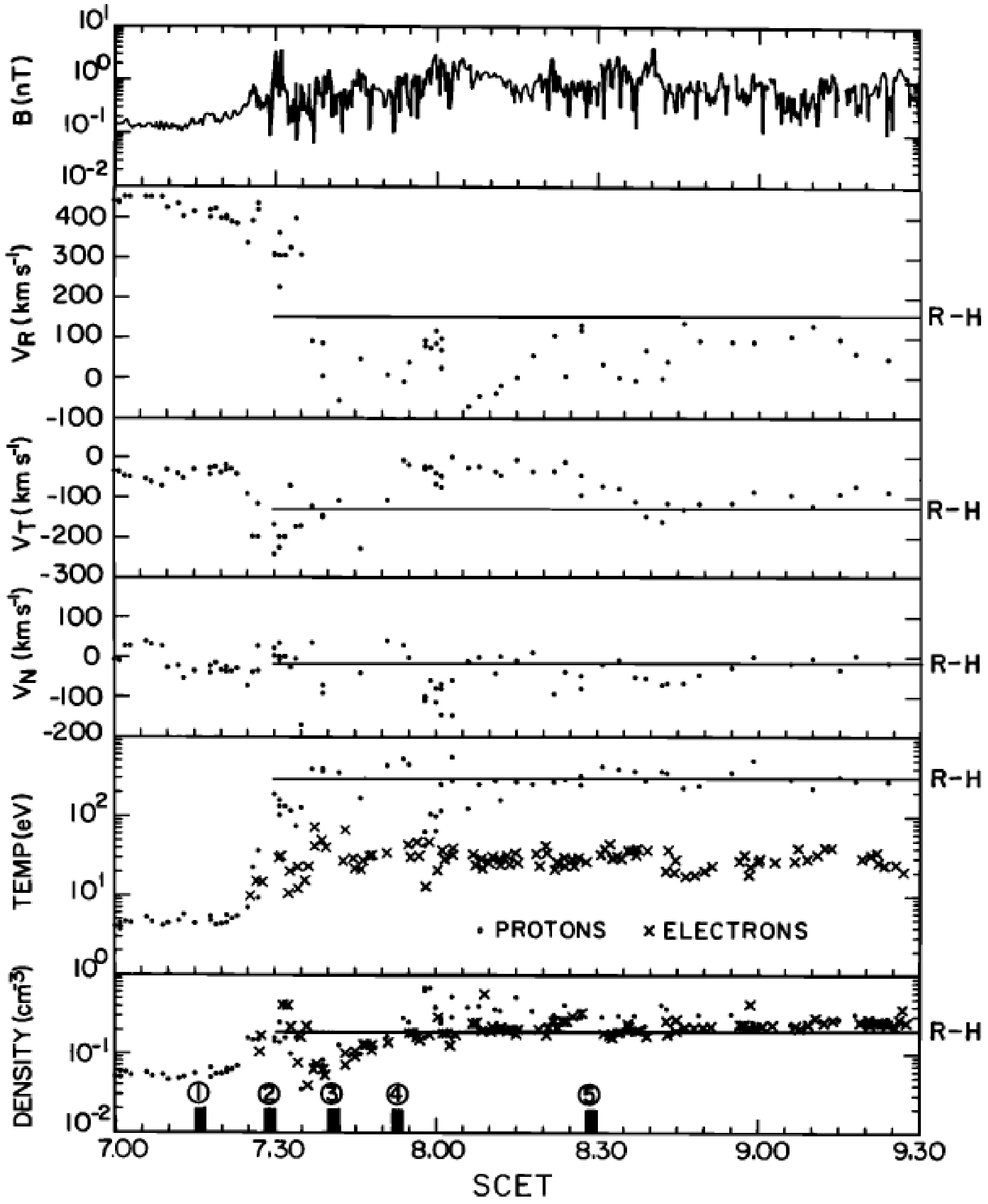

Figure 2.2: Profiles of the magnetic field (9.6 s cadence), velocity components, temperature and density as a function of the spacecraft event time (SCET) observed during Voyager 2's encounter with the Uranian bow shock [*Bagenal et al.*, 1987]. Horizontal lines denote the Rankine-Hugoniot prediction for a high M_A quasiperpendicular shock. Figure reproduced from *Bagenal et al.* [1987].

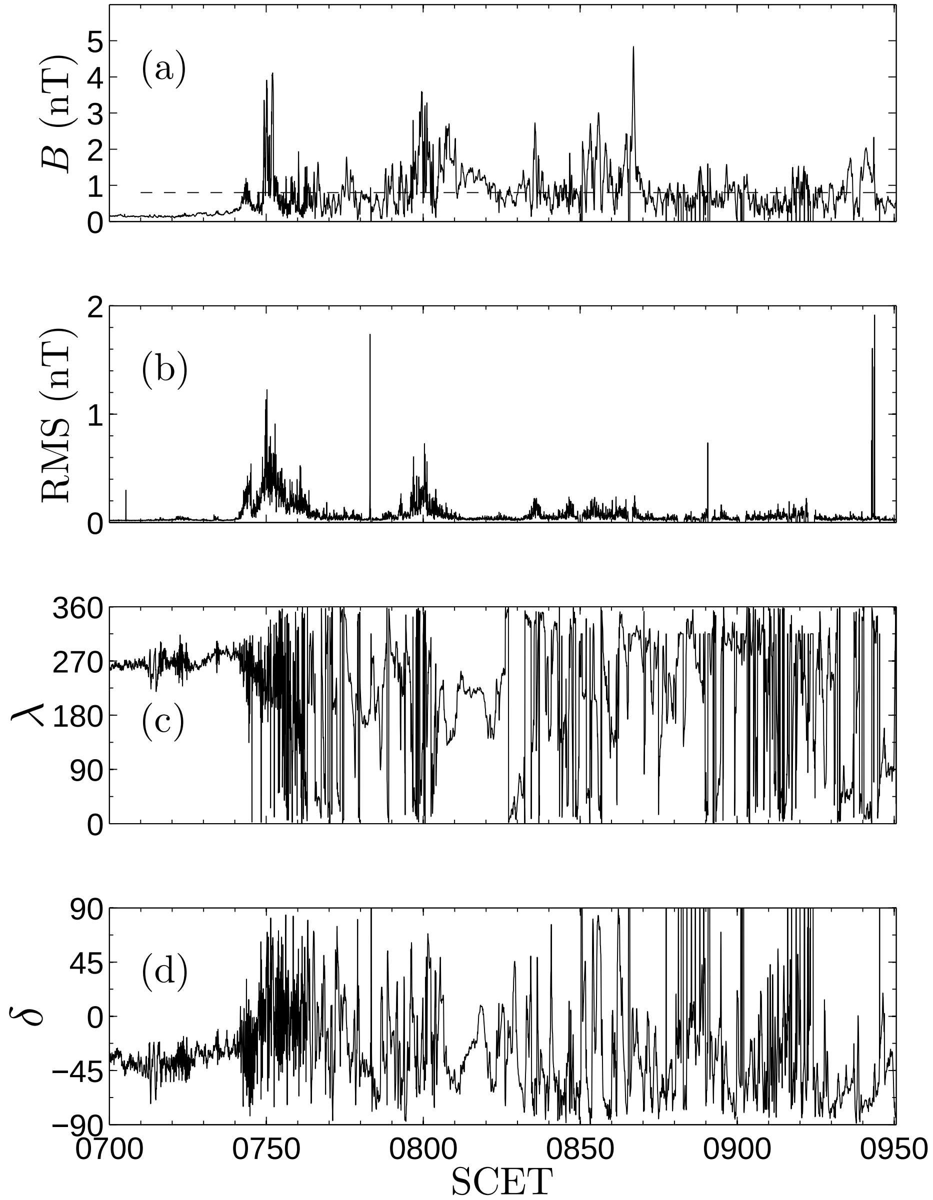

Figure 2.3: Mean magnetic field, RMS magnetic field and magnetic direction angles (λ, δ) at a 1.92 s cadence as a function of spacecraft event time (SCET) observed during Voyager 2's encounter with the Uranian bow shock. The dashed line in panel (a) denotes the R-H prediction for the downstream magnetic field strength.

found specifically at about 0725, 0730, 0800, and 0845 SCET. Furthermore, for much of the period downstream from the initial shock crossing, the maximum magnetic enhancement ratios exceed by a factor of 4–6 the maximum asymptotic value $B_{\mathrm{max}}/B_1 \approx 4$ predicted by the R-H conditions (Figure 2.3). These anomalies do not appear to have been addressed in previous investigations of Voyager 2 observations and have been left unexplained. Third, the field takes $\approx$ 2 hours to settle down to the average downstream value of $\langle B_{\mathrm{down}}\rangle \approx 0.7$ nT, regarded by *Bagenal et al.* [1987] as the downstream state for their R-H calculations. With $\langle B_{\mathrm{down}}\rangle/B_1 = 3.7$, *Bagenal et al.* [1987] found good agreement with the observed magnetic and plasma parameters. A detailed analysis of Uranus's bow shock motions by *Xue et al.* [1996], using upstream Langmuir waves and magnetic connection conditions, gave strong evidence that the bow shock was in fact moving away from the Sun, towards Uranus, just before the Voyager 2 encounter. Below we specifically address and interpret all three of these points, finding that shock reformation and the planetwards shock motion provide a consistent interpretation of the Voyager data.

2.4 Simulation Code and Setup

In this paper, we use a standard 1-D hybrid simulation code [*Winske et al.*, 2003] developed by *Yuan et al.* [2007]. The simulation code calculates the plasma velocity and electromagnetic fields in 3-D. Electrons are treated as a massless fluid whereas ions are treated as massive particles whose trajectories are followed using the standard PIC method. The electromagnetic fields are calculated in 3-D using Maxwell's equations in the Darwin approximation, with currents and charge densities summed over the electrons and ions. A small but nonzero resistivity ($\eta = 1.0 \times 10^{-2}\ \mu_0 v_A^2 \Omega_{ci}^{-1}$) is incorporated into the code to ensure it runs smoothly, via the resistive term $\eta\mathbf{j}$ in Ohm's law. Below the code's effective numerical resistivity is estimated and found to be within an order of magnitude of estimates inferred from observations of Earth's bow shock by *Scudder et al.* [1986]. The simulation grid has a spatial resolution of $dx = 0.3\ v_A/\Omega_{ci}$, 10^3 particles per cell, and a time step of $dt = 1.0 \times 10^{-5}\ \Omega_{ci}^{-1}$.

The shock is induced by injecting a high speed plasma from the left-hand boundary of the simulation cell, which is then specularly reflected off the infinitely conducting right-hand wall. In our simulations we chose plasma parameters very similar to those observed by Voyager 2 upstream of Uranus, as estimated by *Bagenal et al.* [1987]: $M_A \sim 23$, $\theta_{Bn} = 85°$, $\beta_e = 1.0$ and $\beta_i = 2.1$.

The simulation frame is transformed into the shock normal incidence frame by a Lorentz transformation. Furthermore, a Lorentz transformation and rotation transforms the simulation frame into the heliographic coordinates of the Voyager 2 spacecraft.

2.5 Results

Figure 2.4 is a contour plot of B/B_1 in the simulation's space-time domain for the upstream parameters assumed for the Uranian bow shock. A shock is visible moving upstream from the top-left to the mid-right, as seen from the leftmost contours of high B/B_1. At a glance several crucial results are clear. First, maximum localized compression ratios of $B_{\max}/B_1 \sim 20$ are found. Second, the shock reforms periodically as evidenced by the high B/B_1 contours occurring in discrete segments along the shock locus. The high B/B_1 regions occur approximately every $T_{ci} \sim 1.8\ \Omega_{ci}^{-1}$. Third, several overshoot-undershoot oscillations occur downstream of the shock, but this region is spatially bounded. Thus Figure 2.4 predicts that Uranus's bow shock should be reforming for the parameters inferred by *Bagenal et al.* [1987], and should have high values of $B_{\max}/B_1$ close to those observed.

Now consider trajectories on which an observing (virtual) spacecraft moves through the simulation domain towards Uranus. A trajectory moving rapidly parallel to the shock normal will move immediately across the shock and through the downstream region, likely seeing no reformation but only a large magnetic compression ratio. In contrast, a trajectory moving slowly relative to the shock will see many shock reformations and stay close to the ramp for a long time. Figure 2.4 illustrates these two classes of trajectories (from here on referred to as the fast and slow trajectories), while Figures 2.5 and 2.6 show the two corresponding $B[x(t)]$ and plasma profiles. The slow trajectory, corresponding to a slow planetwards shock motion similar to that of *Xue et al.* [1996], would qualitatively correspond to a spacecraft trajectory similar to the red trajectory in Figure 2.4.

The magnetic field, ion flow velocity, ion temperature, and ion density predicted along the two trajectories are shown in Figures 2.5 and 2.6. Qualitatively, Figures 2.2 and 2.6 demonstrate the same trends in plasma parameters across the shock. These plasma parameters are averaged over a simulation time ($0.03\ \Omega_{ci}^{-1}$) equivalent to the 9.6 s time averages given in *Bagenal et al.* [1987]. The simulated time in Figures 2.5, 2.6, and 2.7 corresponds to 1 hour

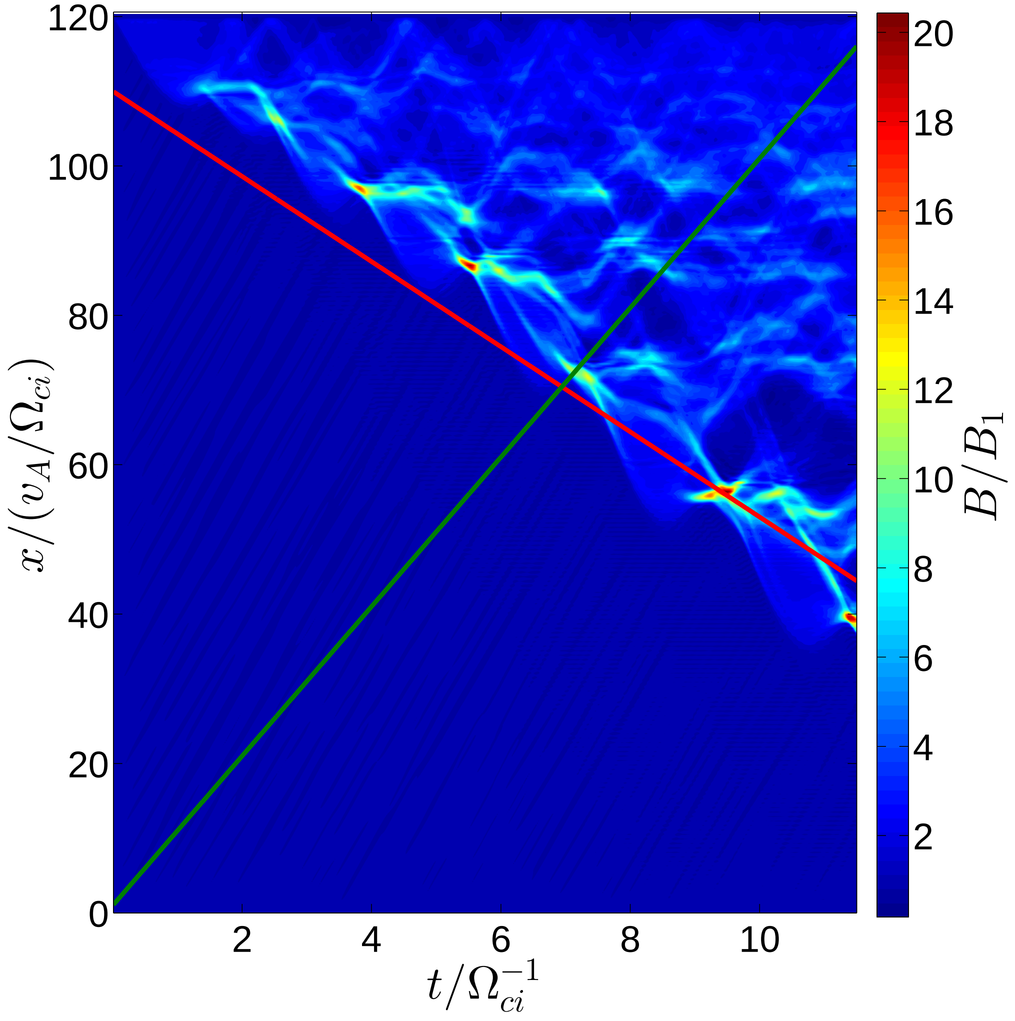

Figure 2.4: The magnetic enhancement profile $B(x,t)/B_1$ as a function of space and time of a simulation using similar plasma parameters ($M_A \sim 23$, $\theta_{Bn} = 85°$, $\beta_e = 1.0$ and $\beta_i = 2.1$) to those observed at Uranian bow shock. Large magnetic enhancements ($B/B_1 \sim 20$) above the R-H predictions are clearly observed. The green and red lines show two test spacecraft trajectories, one moving rapidly relative to the shock (green) and one moving slowly relative to shock (red).

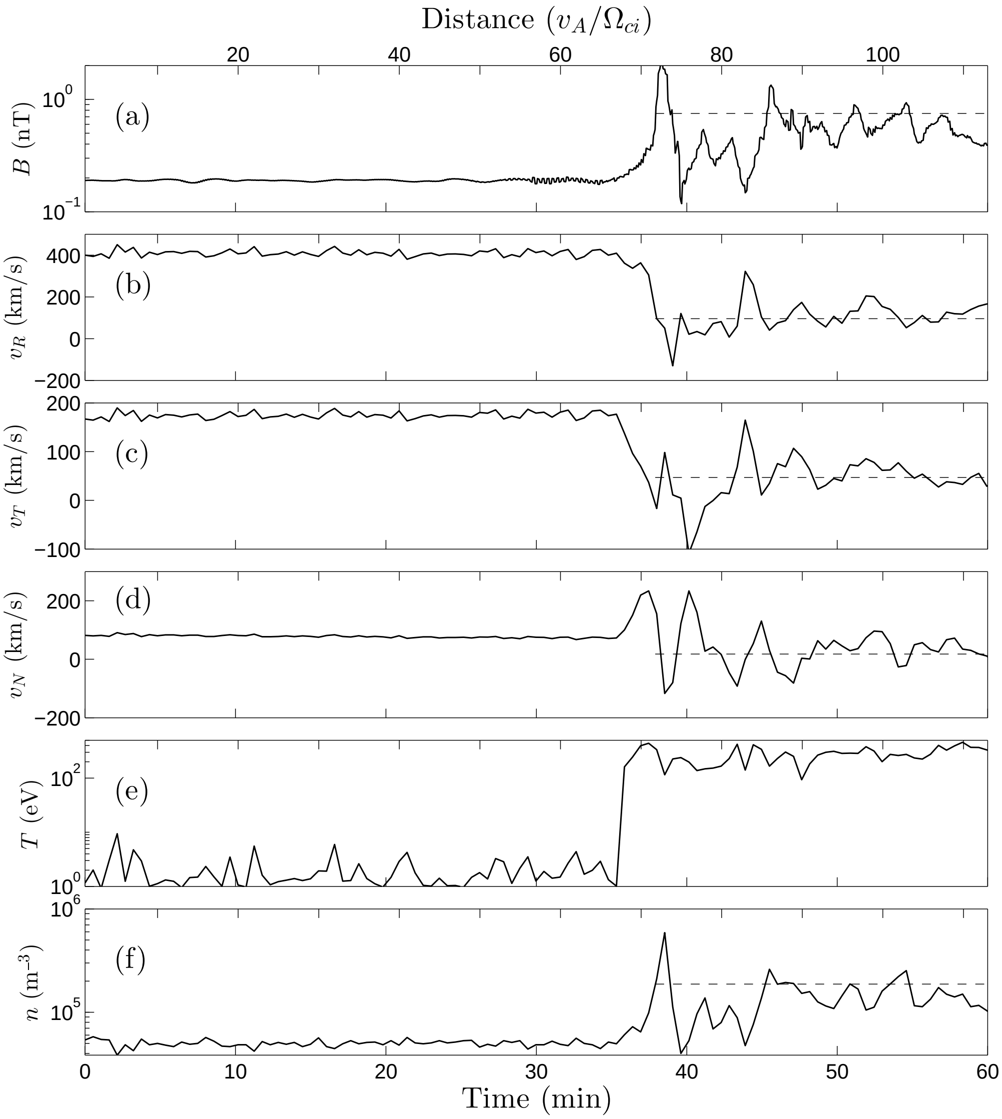

Figure 2.5: The simulated (a) magnetic field, (b)–(d) velocity components, (e) ion temperature and (f) number density along the fast (green) trajectory in Figure 2.4 with the downstream averaged values (dashed lines) predicted by the R-H conditions. Note the rapid transition of the plasma parameters to steady downstream values after only one to two overshoot-undershoot oscillations.

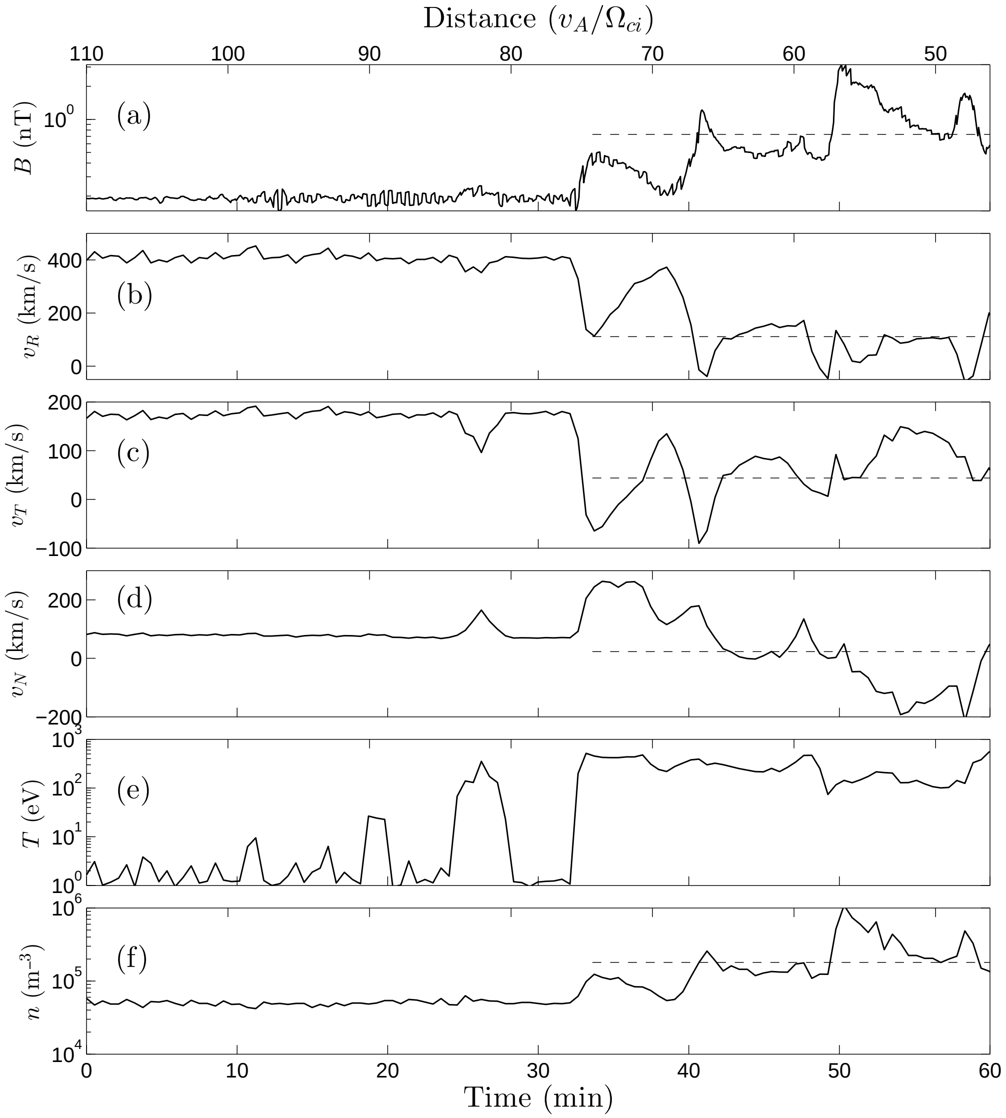

Figure 2.6: Simulated (a) magnetic field, (b)–(d) velocity components, (e) ion temperature and (f) number density along the slow (red) trajectory in Figure 2.4, using the same format as Figure 2.5.

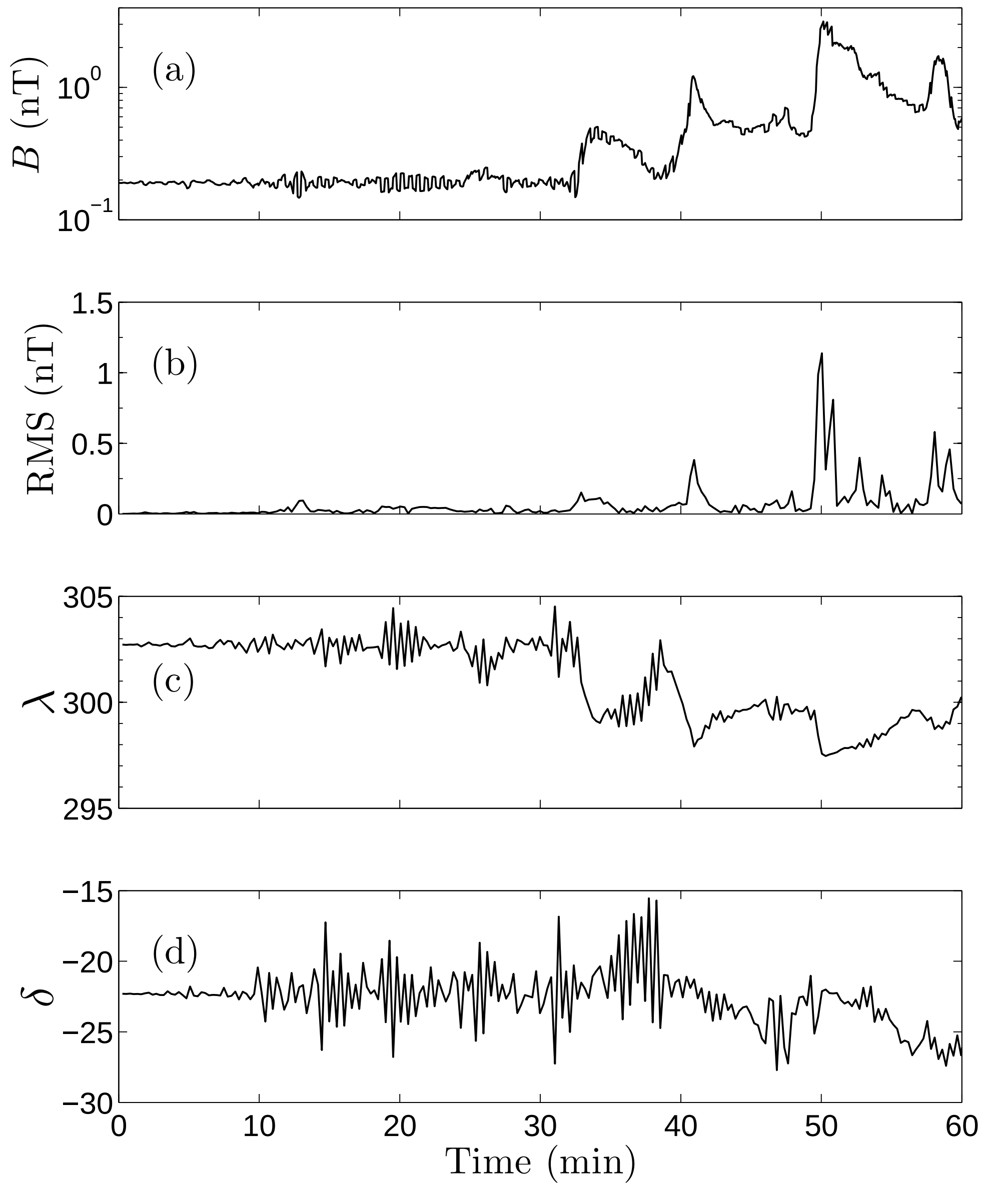

Figure 2.7: Simulated (a) mean magnetic field, (b) RMS field, and direction angles (c) λ and (d) δ, calculated over 0.03 Ω_{ci}^{-1} as a function of time along the slow (red) trajectory in Figure 2.4.

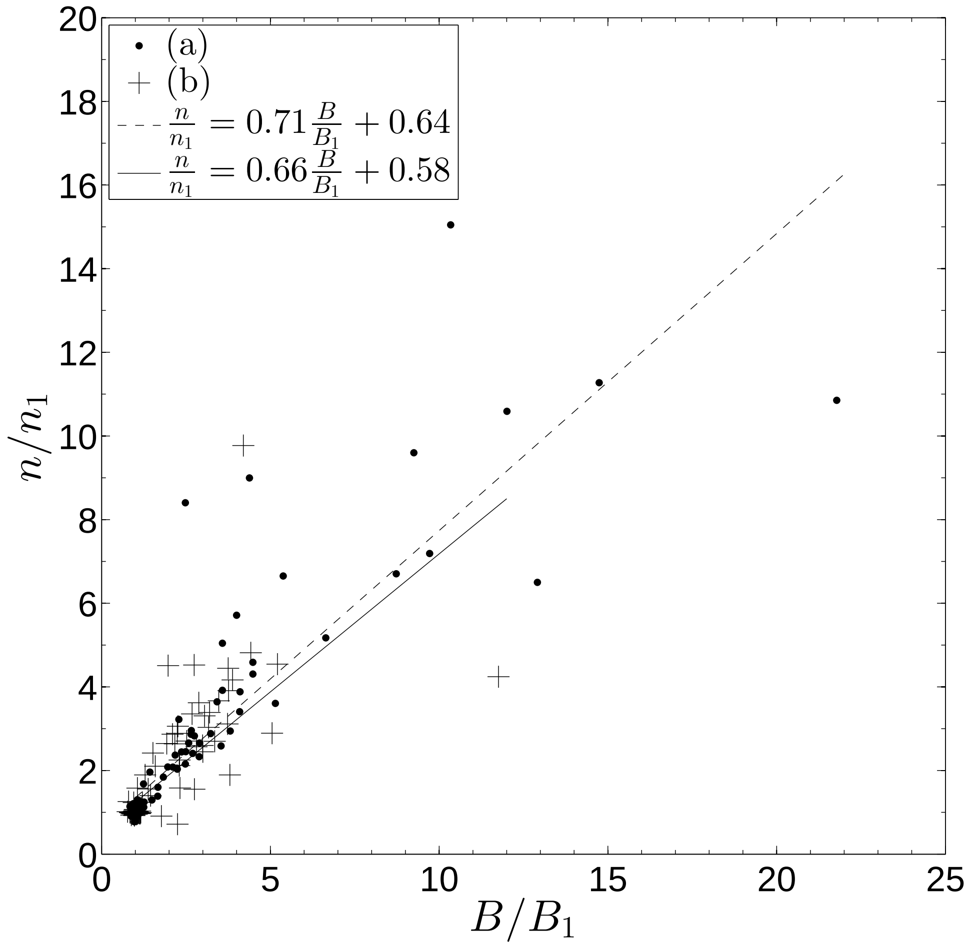

Figure 2.8: Scatter plot of the normalized number density n/n_1 versus the magnetic enhancement ratio B/B_1 along the fast trajectory (●) in Figure 2.5 and slow trajectory (+) in Figure 2.6.

SCET, while the corresponding speeds for the observing point are $v \sim 10v_A$ and $v \sim -5.7v_A$ for the fast/green and slow/red trajectories, respectively.

The velocity components and temperature in Figures 2.5 and 2.6 show rapid transitions to the predicted downstream values, even before the observing location is more than two overshoot-undershoot oscillations downstream of the nominal location of the shock front. Due to it being determined almost exclusively by the ring distribution of the specularly reflected ions, the ion temperature achieves the downstream value in the foot, and is essentially constant once the ramp is crossed for the first time. The flow velocity does oscillate as reformation events occur, but quickly reaches downstream averaged values of order those predicted by the R-H conditions (as shown in Figure 2.5). In contrast, the density shows large oscillations with reformation events and also attains compression ratios $n/n_1 \sim 20$ comparable to those for the magnetic field. Indeed, it is striking how well n and B track each other across the shock (Figures 2.2, 2.5, and 2.6). This is further evident upon examining Figure 2.8, which is a scatter plot of n/n_1 and B/B_1 for both trajectories.

Figure 2.6 shows very large magnetic compression ratios $B/B_1 \sim 10 - 20$ persisting for $\lesssim 30$ minutes and occurring in oscillations with periods ~ 10 minutes along the nominal slow trajectory chosen. This is qualitatively very similar to the Voyager observations but quantitatively slightly different since the observed peaks occur 20 minutes apart. This is plausibly due to Voyager's trajectory being slightly different from that chosen in the simulation.

The magnetic increase near 0725 SCET in the Voyager data (Figures 2.2(a) and 2.3(a)) might sometimes be regarded as the magnetic foot of the shock. However, upon further examination, the maximum magnetic enhancement ratio of this event is $B/B_1 \sim 7.4$. This value exceeds the maximum R-H prediction by almost a factor of two and is much larger than typical enhanced factors for a magnetic foot ($\leq 30\%$). Another interpretation is that this event is associated with reformation of the shock: Voyager is observing a partial reformation of the shock that is similar to the one near time 35 minutes in Figure 2.6 for the red trajectory in Figure 2.4. On detailed inspection, then, additional reformation events when Voyager is very near the shock (within several v_A/Ω_{ci}) are believed to occur near times 0725, 0730, 0800, 0805, 0822, 0830–0840, and 0925 SCET in Figures 2.2 and 2.3. The rapid transitions for the whole period 0720–0930 SCET in B between B_1 and values well above the R-H predictions, as well as enhanced values of n, are considered strong evidence of Voyager being near a reforming shock for the whole period 0720–0930 SCET.

On the other hand, it is recognized that some of the observed oscillations in B occur much faster (Figure 2.2) than predicted by the simulations shown in Figures 2.5 and 2.6, requiring us to either appeal to other waves or else to more rapid back-and-forth movements of the shock. The existence of such back-and-forth motions appears consistent with the observed radial velocities, which fluctuated significantly between values of -100 km s^{-1} and 100 km s^{-1} for a period ~ 1 hour past the shock. Furthermore, the observed perturbations in ion density, ion flow velocity, and ion temperature downstream from the shock support such variable motions and are more plausible than slow one-way transitions like that in Figure 2.5 for the green trajectory in Figure 2.4.

In summary, comparisons of Figures 2.2, 2.3, 2.6, and 2.7 show that good agreement exists between the simulation and observations. The high compression ratios of the reforming shock in the simulations account naturally and convincingly for the observations of $B/B_1 \sim 20$ and $n/n_1 \sim 15$ seen in the Voyager observations. Thus, the simulation provides simple explanations of these long unanswered questions and provides strong evidence that the Uranian bow shock was undergoing reformation during the Voyager encounter.

Furthermore, comparisons between the simulation and observations also provide evidence that the shock moved planetwards and remained very close (several v_A/Ω_{ci}) to the spacecraft during the period 0730–0900 as Voyager approached Uranus. However, it is recognized that the simulation results for the magnetic field's direction angles (Figure 2.7) do not exhibit the extreme variability shown in the Voyager observations (Figure 2.3). These differences may be attributed to the neglect of particular wave physics not incorporated into our hybrid simulation model (note that the electron parameters could not be determined due to the assumption of an electron fluid in the hybrid simulations). Nevertheless, the predicted RMS magnitudes do correspond relatively well to spacecraft observations, as seen by comparing Figures 2.3(b) and 2.7(b).

2.6 Discussion

Shocks routinely produce magnetic compression ratios at the overshoot greater than the maximum downstream compression ratio of 4 predicted by the R-H conditions [*Livesey et al.*, 1982; *Russell et al.*, 1982; *Russell*, 1985], although this is not widely known. Likewise, large magnetic compression ratios $B/B_1 \gg 4$ are commonly exhibited in high M_A reforming shocks in our simulations. Therefore, one can ask more generally what is the degree of correlation between large magnetic enhancements and the existence of reformation? The previous work makes it unclear if large magnetic compression ratios can be used to infer the existence of a reforming shock. It is emphasized here, though, that the simulations show that the downstream plasma density, flow velocity, and magnetic field rapidly approach the R-H prediction. That is, in Figure 2.5 the large magnetic and density enhancements are found only in the near vicinity of the ramp and first overshoot.

Currently, there is no convincing theory which accounts for the existence of the large magnetic enhancement ratios observed in simulations and spacecraft data. One possible model is that these large ratios in n and B arise from detailed balance between upstream ram pressure P_{ram} and the magnetic pressure

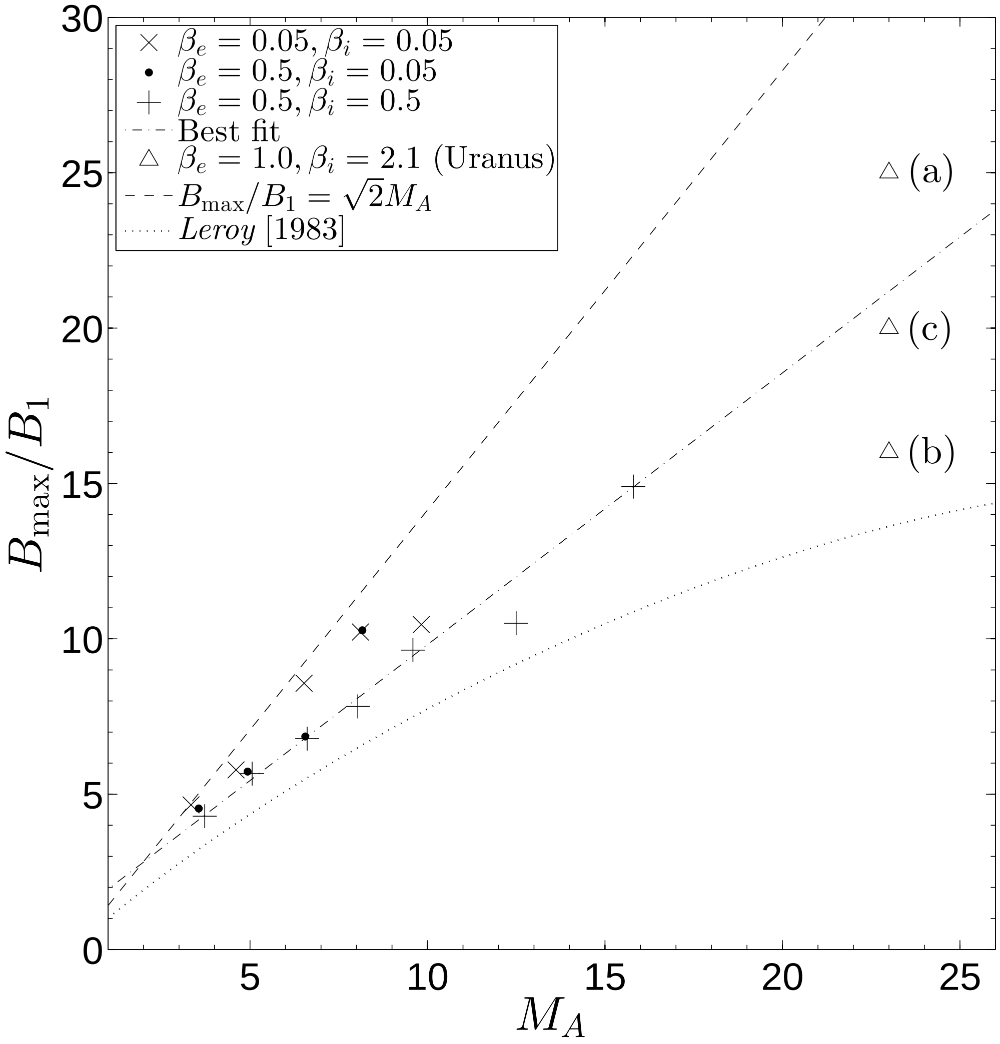

Figure 2.9: Scatter plot of B_{max}/B_1 versus M_A for multiple simulations with various β_i and β_e, but a single $\theta_{Bn} = 85°$. The dash-dot line represents the line of best fit for $\beta_e = \beta_i = 0.5$. The corresponding values observed by Voyager 2 at the Uranian bow shock are plotted with triangle symbols (△) and labels (a) and (b) for 1.92 s and 9.6 s cadence data, respectively. Label (c) denotes Figure 2.4's simulation run with a square symbol (□). The dashed and dotted lines show the predictions from (2.1) and (2.2) respectively.

P_B at the overshoot. Given that $P_{\text{ram}} = \rho_1 v_1^2$ and $P_B = B_{\text{max}}^2/2\mu_0$, equating the two pressures and simplifying we find:

$$\frac{B_{\text{max}}}{B_1} = \sqrt{2}M_A. \tag{2.1}$$

Equation (2.1) implies a linear relationship between the magnetic overshoot and the Alfvén Mach number. Figure 2.9 is a scatter plot between B_{max}/B_1 and M_A derived from multiple simulations with a range of plasma beta. The observations at the Uranian bow shock of Voyager 2 are also plotted in Figure 2.9. The simulation results conform relatively well to the theoretical line at low $M_A \sim 4 - 10$. However, at much larger $M_A \sim 23$, the simulated and observed results depart significantly from the predicted value. Recognizing that the simulation results for high ion beta β_i lie routinely below the simulation results for the lower β_i, the best fit line for $\beta_i = 0.5$ is obtained: $B_{\text{max}} = 0.87M_A + 1.1$. This line lies close to the Voyager 2 results and associated simulation for Uranus. Thus, Figure 2.9 provides strong evidence that (1) the simulation results of Figures 2.4-2.10 are not atypical and (2) the strength of the maximum magnetic overshoot increases approximately linearly with M_A with a gradient that depends on β_i. It also suggests that models involving balance of the magnetic pressure and ram pressure are attractive for explaining the strength of the magnetic overshoot of the shock.

Earlier, *Leroy* [1983] investigated the macrostructure of perpendicular shocks in the supercritical regime and derived an expression for the magnetic overshoot as a function of M_A:

$$\frac{B_{\text{max}}}{B_1} = \frac{M_A^{7/6}}{4\beta_R^{1/4}} \left[\frac{10(\beta_R^{1/4}/M_A^{1/2}) - 2}{4 + (M_A^{1/2}/\beta_R^{1/4})} \right]^{1/3}, \tag{2.2}$$

where β_R is proportional to the upstream ion beta ($\beta_R \approx \frac{3}{2}\beta_i$). *Leroy* [1983] and *Bagenal et al.* [1987] both approximated (2.2) to leading order as $B_{\text{max}}/B_1 \propto M_A^{7/6}$. Nevertheless, we retain the original expression as plotted in Figure 2.9. We find that (2.2) underestimates the magnetic overshoot for large M_A compared to the simulation results and observations. Moreover, (2.2) turns over for high M_A and is not directly proportional to $M_A^{7/6}$, so that consideration of the leading order term alone, as done by *Leroy* [1983] and *Bagenal et al.* [1987], is not correct at high enough M_A ($\gtrsim 5$).

Basic shock theory and observations suggests that the transition from perpendicular shocks to parallel shocks induces turbulence in the magnetic field

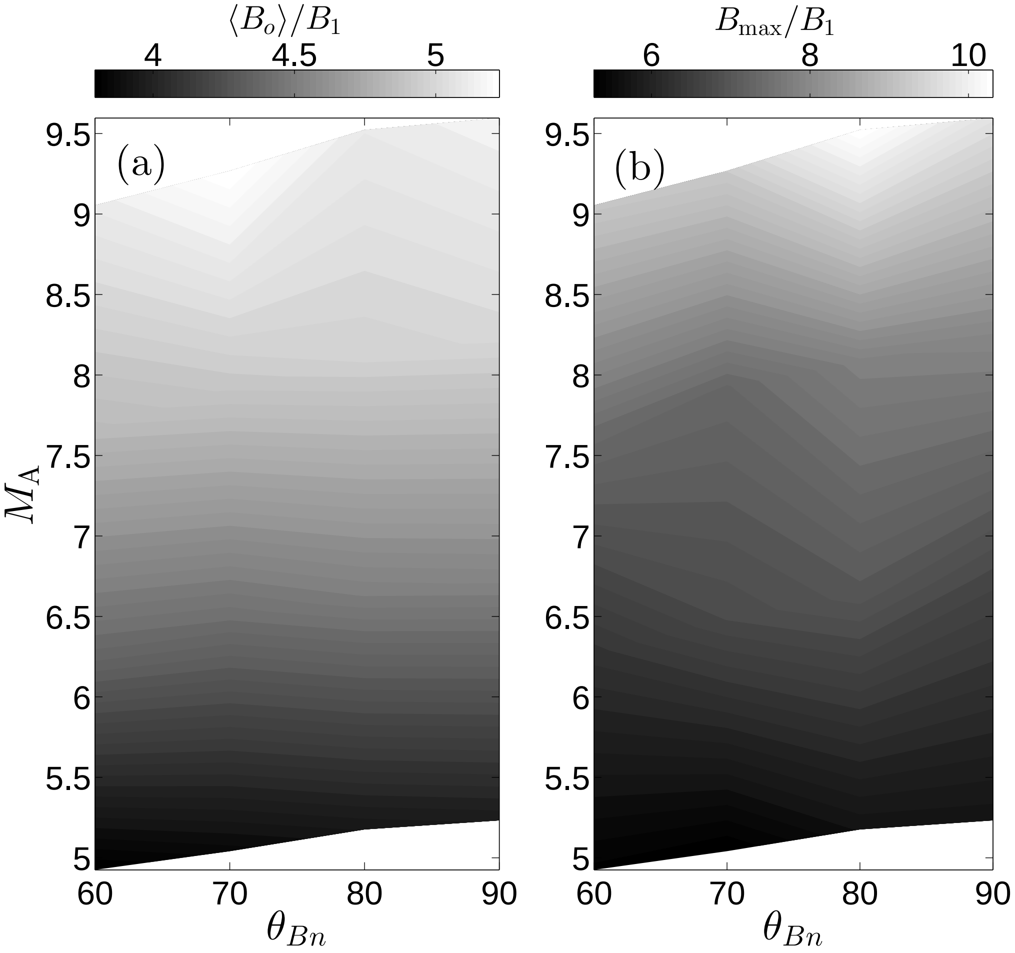

Figure 2.10: Simulated (a) average magnetic overshoot $\langle B_{\rm os} \rangle / B_1$ and (b) maximum magnetic enhancement ratio $B_{\max}/B_1$ as functions of M_A and θ_{Bn}. The contour plots reveal the relative insensitivity of $\langle B_{\rm os} \rangle / B_1$ and $B_{\max}/B_1$ to varying θ_{Bn}.

and also affects the magnetic compression ratio [*Russell*, 1985]. In the context of reformation, it has also been unclear how variations in θ_{Bn} affect the dynamics of nonstationarity, although *Yuan et al.* [2009] did not find a strong dependence in the range $\theta_{Bn} \sim 80 - 90°$. We have therefore performed a parametric study of θ_{Bn} between the values of $45°$ and $90°$ using multiple simulation runs. Figures 2.10(a) and 2.10(b) show the spatio-temporal average (between and including the first two overshoots) of the normalized magnetic overshoot $\langle B_o \rangle / B_1$ and $B_{\max}/B_1$, respectively, as functions of θ_{Bn}. The results show that reformation is relatively insensitive to varying θ_{Bn}, in particular in the range of values $\theta_{Bn} \sim 85° \pm 9°$ found by *Bagenal et al.* [1987] at Voyager 2's inbound Uranian bow shock crossing. Thus our claim for evidence of reformation is robust for changes in $\theta_{Bn} = 85° \pm 9°$, both within and well outside the range of measurement uncertainty.

Hybrid simulations have both an effective numerical resistivity and an applied resistivity. We have estimated the effective numerical resistivity in our code using a qualitative approach and found a value $\eta_s \sim 0.1 - 1\ \mu_0 v_A^2/\Omega_{ci}$; details are in the Appendix. This is comparable with the value $\eta_s \sim 0.5\ \mu_0 v_A^2/\Omega_{ci}$ observed by *Scudder et al.* [1986] for Earth's bow shock. This implies that our simulation should produce reasonable results for the Uranian bow shock provided η does not scale significantly with heliocentric distance. Note that this effective numerical resistivity includes the physical resistivity associated with included wave interactions, as well as numerical resistivity associated with the code algorithm and implementation.

These findings have numerous applications in fields of space physics. In particular, the theory for type II solar and interplanetary radio bursts [*Knock et al.*, 2001, 2003a,b; *Knock and Cairns*, 2005] relies explicitly on the magnitude of the maximum magnetic compression. This is because type II emissions depend on electron beams produced by the shock wave via the mechanism of shock drift acceleration, so the number of reflected electrons and their distribution function depend on the compression ratio B/B_1, as then do the levels of Langmuir waves and radio emission. *Yuan et al.* [2008b] test-particle calculations demonstrate that magnetic overshoots significantly affect electron reflection and should not be neglected. In addition, test-particle simulations of electrons reflected from reforming and non-reforming shocks [*Yuan et al.*, 2008a] show that reformation gives rise to bursty electron reflection events and that the electron characteristics are substantially different from those predicted using a simple linear shock with no overshoot and a compression ratio given by the R-H conditions. Thus our simulations, specifically their demonstrations of both reformation and the dependence of the maximum overshoot on M_A, suggest that the predicted intensities of type II bursts could be significantly underestimated, since the theory currently includes neither the magnetic overshoot nor enhanced magnetic compression, but instead uses the R-H prediction.

2.7 Conclusions

Extensive analyses of Voyager data at the Uranian bow shock showed localized magnetic and density enhancements a factor of $4-6$ above the asymptotic predictions of the R-H relations near the initial shock ramp and for the following 2 hours downstream. We performed simulations using a 1-D standard hybrid code with similar plasma parameters observed at the Uranian bow shock. Our simulation results provide strong evidence that the Voyager observations (particularly the extremely high and long-duration magnetic and density compressions) can be explained simply in terms of the bow shock reforming and receding planetwards with the spacecraft. This interpretation is further supported by the rapid spatial transition (within one or two undershoot-overshoot cycles) in the simulations and observations of the velocity components, and ion temperature into the R-H downstream values. Hence, the results of this paper show very strong evidence that the Uranian bow shock was undergoing reformation. Additional simulations showed that the magnetic overshoot increased approximately linearly with M_A and is robust against variations in magnetic field orientation. These large overshoots may be important in applications involving particle acceleration and type II solar radio bursts. Future work could investigate the existence of reformation in other planetary bow shocks and the heliosphere termination shock using a similar analysis to the one developed in this paper.

Appendix: Effective resistivity in the code and at Earth's bow shock

At low M_A resistivity is typically believed [*Coroniti*, 1970; *Kennel et al.*, 1985] to provide the main dissipation source for a collisionless quasiperpendicular shock. However, at higher M_A an additional dissipative effect is required in order to satisfy the R-H conditions. This extra mechanism is the reflection of a substantial fraction of the upstream ions at the shock front, known as specular reflection. At a sufficiently high resistivity, we would expect damping of high frequency waves and the tendency for the shock structures to smooth out.

In standard hybrid simulations, a small finite resistivity is typically included to ensure the simulation runs smoothly. This applied resistivity is incorporated by including the resistive term $\eta \mathbf{j}$ in the Ohm's law:

$$\mathbf{E} + \mathbf{u} \times \mathbf{B} = \eta \mathbf{j} + \frac{1}{ne} \mathbf{j} \times \mathbf{B} - \frac{1}{ne} \nabla P_e + \frac{m_e}{ne^2} \frac{\partial \mathbf{j}}{\partial t}. \tag{2.3}$$

A qualitative approach is used to estimate the numerical resistivity η by varying the applied resistivity and observing the evolution of the magnetic profile: the profiles will become smoother once the applied resistivity exceeds the numerical resistivity and a reforming shock may stop reforming.

We performed simulations of reforming ($M_A = 9.7$) and non-reforming ($M_A = 2.7$) shocks for applied values of η in the range $0.001 - 10\ \mu_0 v_A^2/\Omega_{ci}$. For each simulation $\theta_{Bn} = 85°$ and $\beta_e = \beta_i = 0.5$. Figures 2.11 and 2.12 depict the magnetic profiles of the nonstationary and stationary shocks respectively for various η. Each profile is taken at the same elapsed computation time.

On inspection, Figures 2.11 and 2.12 show that a large applied η tends to smooth out the shock structures, as expected. Specifically, the ramp length increases and the upstream waves and under-overshoot oscillations in the downstream region are less apparent at high η. In the high M_A case reformation is affected by η, with the $\eta = 1$ run only marginally reforming and the $\eta = 10$ run not reforming. For non-reforming and reforming shocks Figures 2.11 and 2.12 imply $\eta \sim 1\ \mu_0 v_A^2/\Omega_{ci}$ and $\eta \sim 0.1 - 1\ \mu_0 v_A^2/\Omega_{ci}$ respectively.

A corresponding observational estimate comes from *Scudder et al.* [1986] analyses of an ISEE-1 crossing of Earth's bow shock on November 7, 1977. Table 2.1 lists the observed plasma parameters. *Scudder et al.* [1986] determined an empirical value of the effective resistivity by performing a regression analysis between the measured current density $\mathbf{j}$ and electric field $\mathbf{E}$. They found $\eta = 1.8 \times 10^3\ \Omega\ \mathrm{m}^{-1}$ for Earth's bow shock. Converting *Scudder et al.* [1986] resistivity into simulation units yields $\eta = 0.5\ \mu_0 v_A^2/\Omega_{ci}$. Comparing the effective resistivity of the simulation code implies that the observed value agrees to within an order of magnitude.

An anomalous resistivity is one greater than the Spitzer resistivity,

$$\eta_{\mathrm{spitz}} = \frac{1}{64\pi\epsilon_1\omega_{pe}} \frac{\ln \Lambda}{\Lambda}, \tag{2.4}$$

where ω_{pe} and $\Lambda = n_e \lambda_D$ (λ_D is the Debye length) are the plasma frequency and plasma parameter, respectively. This may be the case in plasmas in which

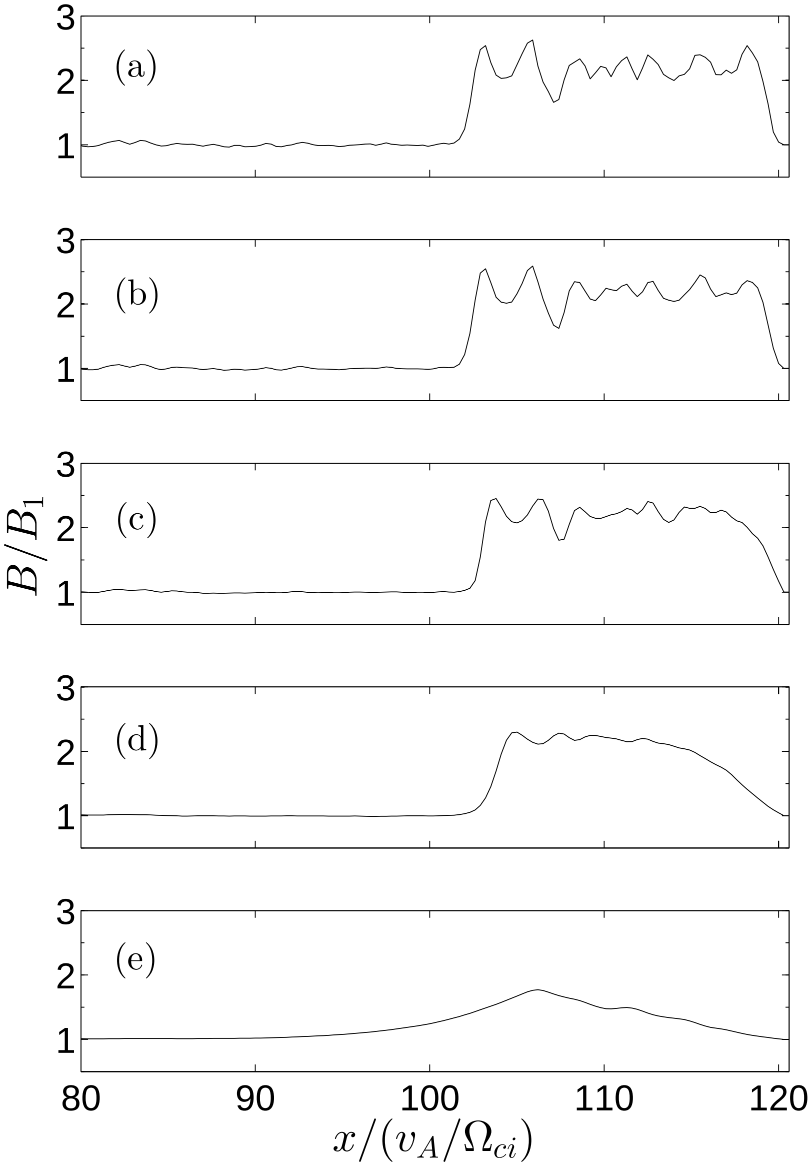

Figure 2.11: Evolution of the simulated magnetic profile for a stationary shock ($M_A = 2.7, \theta_{Bn} = 85°$, $\beta_e = \beta_i = 0.5$) as a function of applied resistivity (a) $\eta = 10^{-3}$, (b) $\eta = 10^{-2}$, (c) $\eta = 10^{-1}$, (d) $\eta = 1$, and (e) $\eta = 10$.

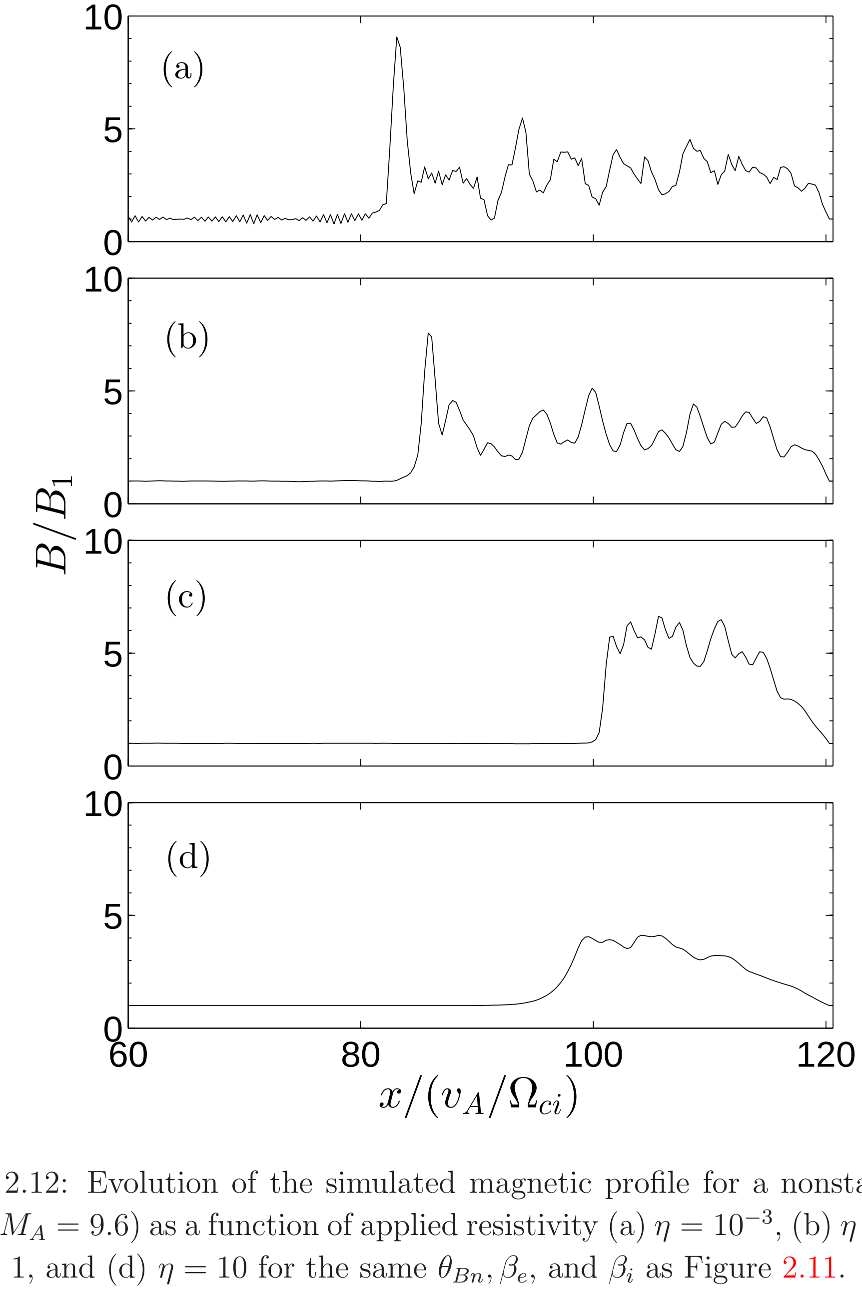

Figure 2.12: Evolution of the simulated magnetic profile for a nonstationary shock ($M_A = 9.6$) as a function of applied resistivity (a) $\eta = 10^{-3}$, (b) $\eta = 10^{-1}$, (c) $\eta = 1$, and (d) $\eta = 10$ for the same θ_{Bn}, β_e, and β_i as Figure 2.11.

collective interactions, such as wave-particle interactions, have superseded collisions in scattering the electrons. Using the plasma parameters in Table 2.1, the Spitzer resistivity for Earth's bow shock is estimated to be $\eta \sim 10^{-9}$ in simulation units. Clearly the resistivity in Earth's bow shock and in our simulations are strongly anomalous.

To some extent, the effective numerical resistivity in the hybrid simulation code is physical. This is because the code includes wave-particle interactions due to the modelling of ion particle dynamics. Specifically, specularly reflected ions develop ring distribution functions at the shock and generate waves in the vicinity of the shock front as they complete their gyromotion. These waves can subsequently interact and scatter other incoming particles. The fraction of the code's effective numerical resistivity that is due to wave-particle interactions is not currently known.

In conclusion, the effective numerical resistivity determined for the simulation code is consistent with *Scudder et al.* [1986] observations of Earth's bow shock. The numerical resistivity and that observed at Earth's bow shock are anomalous, being much larger than the Spitzer resistivity. Hence, we can be quite confident in applying the code to planetary bow shocks, as done in this paper.

Chapter 3

New Model for the Initial Reflection and Transmission of Thermal Ions at Quasi-Perpendicular Collisionless Shocks

3.1 Abstract

It is widely believed that the electrostatic potential $\Delta\phi_E$ is primarily responsible for the reflection of thermal ions at the ramps of quasiperpendicular collisionless shock waves, and so for associated heating downstream. Specifically, ions with insufficient kinetic energy to overcome the electrostatic potential barrier are specularly reflected. However, measurements from our 1-D hybrid simulations indicate that $\Delta\phi_E$ is typically smaller than the kinetic energy of the incoming thermal ions, implying that very few ions will be reflected for a purely electrostatic specular reflection model. Nevertheless, we still observe up to 70% of the initial population being reflected in our hybrid simulations. We investigate this issue in detail by exploring the forces acting on the ion particles along their trajectories, and propose a new analytic model for the ion reflection process which includes magnetic field effects. Specifically, we calculate analytically the magnetic deflection of the ion distribution antiparallel to the convection electric field and the associated slowing along the normal direction due to the Lorentz force. We then derive an expression for a total effective potential which is the sum of the electrostatic potential plus the net work done along the normal direction by magnetic field effects. The reflection efficiency as a function of Mach-number is predicted using the total effective potential and an analytic expression for the reflection cutoff and its rotation is also derived. We find excellent agreement between the simulations and the new model for

ion reflection by the shock front, and show that both the electrostatic potential and magnetic deflection are vital in the ion reflection process.

3.2 Introduction

More than one mechanism or process exists for ion reflection at shocks, e.g., shock drift acceleration, magnetic mirror reflection, diffusive shock acceleration, and specular reflection. The mechanism by which thermal ions are specularly reflected off quasiperpendicular shocks is widely attributed to an electrostatic potential $\Delta\phi_E$ across the shock layer that essentially reverses the incident normal velocity (the so-called specular reflection) [*Leroy et al.*, 1982; *Gosling et al.*, 1982]. The potential's magnitude and variation are vital in determining the fraction α of the incoming ion distribution that is initially reflected at the shock. This is important to the thermalization of the plasma because ions that are initially reflected and then gyrate downstream are believed to carry most of the thermal energy in the downstream distribution. Therefore ion reflection is an important dissipation process which can redistribute energy between the total electromagnetic field energy and the total kinetic and thermal energy of the ion distribution. The focus of the present Chapter is the reflection of ions at the shock front and their gyration downstream (e.g. "specular reflection"), not the production of upstreaming particles by shock drift acceleration [e.g. *Armstrong et al.*, 1985] or diffusive shock acceleration [e.g. *Scholer*, 1985], or the reflection of particles downstream of the shock ramp [e.g. *Gedalin*, 1996].

The time-averaged jumps in plasma properties between the upstream and downstream regions of a macroscopic shock are governed by the Rankine-Hugoniot (R-H) conditions [e.g., *Scudder et al.*, 1986]. The R-H conditions are derived from the conservation of mass, energy, momentum, transverse electric field, and normal magnetic field, and depend on the Alfvén Mach number M_A, angle θ_{Bn} between the upstream magnetic field and normal flow direction, and plasma beta β. The Alfvén Mach number is defined as the upstream normal fluid speed u_{x1} (we define the normal direction to be along x) divided by the upstream Alfvén speed v_A. The plasma beta β is the ratio of the upstream thermal pressure $P_{th} = n_1 k_B T_1$ to the upstream magnetic pressure $P_B = B_1^2/2\mu_0$ where n_1 is the upstream number density, k_B is Boltzmann's constant, T_1 is total upstream temperature, B_1 is the upstream magnetic field strength, and μ_0 is the magnetic permeability. We define the upstream ion gyrofrequency as $\Omega_{ci} = eB_1/m_i$ where e is the electric charge and m_i is the proton mass.

The stable formation of collisionless shocks in space plasmas is due to the balance between non-linear wave dispersion and energy dissipation. *Coroniti* [1970] showed that for a fast mode shock, if resistivity is the only dissipation process, then the shock cannot remain steady above a critical Mach number M_A^*. Several mechanisms have been suggested to provide this additional source of dissipation. *Krasnoselskikh et al.* [2002] proposed that the generation and emission of whistler waves from the shock could redistribute the necessary energy from the shock for stability. Another proposed dissipation process is ion reflection by the shock [*Coroniti*, 1970; *Gosling et al.*, 1982].

Spacecraft observations of subcritical ($M_A < M_A^*$) quasiperpendicular ($\theta_{Bn} > 45°$) shocks show that the magnetic field profile is typically laminar [*Livesey et al.*, 1982], i.e., the spatial profile increases monotonically from its upstream value to its downstream value, at the so called "ramp" of the shock. In comparison, spatial profiles of supercritical ($M_A > M_A^*$) quasiperpendicular shocks contain local structures upstream and downstream of the magnetic ramp where the magnetic field strength is enhanced, due to the accumulation of reflected ions there, known as the foot and overshoot respectively. *Livesey et al.* [1982] analyzed measurements of the overshoot from ISEE-1 and -2 spacecraft data for multiple subcritical and supercritical terrestrial bow shocks, with measurements of M_A^* varying between 2 and 3. They discovered that the magnitude of the overshoot $B_o = \max(B)$ relative to B_1 increases dramatically for $M_A > M_A^*$, as confirmed with hybrid simulations [*Burgess et al.*, 1989; *Tiu et al.*, 2011], suggesting that ion reflection as an important dissipation process for supercritical shocks. On the other hand, *Leroy et al.* [1982] performed 1-D hybrid simulations of M_A between 2 and 10, finding that B_o/B_1 is correlated with α, increasing steadily with M_A (see also [*Tiu et al.*, 2011]).

For a narrow shock width $L \ll \lambda_i$, where $\lambda_i = v_A/\Omega_{ci}$ is the ion inertial length, one usually assumes that the magnetic field is unimportant in the ion dynamics, and therefore that the $\mathbf{v} \times \mathbf{B}$ force can be neglected [*Gosling and Thomsen*, 1985]. This model of ion reflection, where only the ion's velocity normal to the shock interface is reversed, is known as specular reflection and depends only on $\Delta\phi_E$ [*Leroy et al.*, 1982; *Gosling et al.*, 1982]. We define the particle's velocity $\mathbf{v}_1 = (v_{x1}, v_{y1}, v_{z1})$ at the leading edge of the foot or ramp, where the magnetic field strength $B(x)$ is first larger by a factor of χ than B_1, or $B(x) > \chi B_1$. The initial gyrophase angle θ_1 and initial thermal speed $v_{\perp 1}$

are then

$$\theta_1 = \tan^{-1}\left(\frac{v_{y1}}{v_{x1}-u_{x1}}\right) \tag{3.1}$$

$$v_{\perp 1} = \sqrt{(v_{x1}-u_{x1})^2 + v_{y1}^2} \tag{3.2}$$

The ion equation of motion is

$$\mathbf{F} = m_i \frac{d\mathbf{v}}{dt} = e(\mathbf{E} + \mathbf{v} \times \mathbf{B}), \tag{3.3}$$

which cannot be solved analytically [*Leroy*, 1983]. If the $\mathbf{v} \times \mathbf{B}$ force is small compared to the electric force $e\mathbf{E}$, then (3.3) simplifies to the expression $d\mathbf{v}/dt = e\mathbf{E}/m_i$, leading to the trivial condition that ions satisfying

$$v_{x1} \le v_c^E \tag{3.4}$$

will be reflected, where $v_c^E = \sqrt{2e\Delta\phi_E/m_i}$ is the specular cutoff speed, and $\Delta\phi_E = \max(\int -E_x dx)$ is the maximum value of the electrostatic potential. Reflected ions can travel upstream for half a gyro-orbit, drifting along the convective electric field, thereby gaining enough energy to now cross the electrostatic cross-shock potential into the downstream plasma. Shock drift acceleration (SDA) [*Armstrong et al.*, 1985] involves similar physics for longer time periods: particles drifting parallel (for ions) or antiparallel (for electrons) to the convective electric field are energized and either transmitted downstream or reflected upstream for good. Under certain conditions multiply reflected ion (MRI) acceleration or "shock surfing" can occur, where ions can be reflected multiple times off the shock, with each reflection accelerating the particle and so reaching energies several to many times larger than the incoming ram energy [*Zank et al.*, 1996; *Lee et al.*, 1996].

However, *Gosling et al.* [1982] acknowledged that the presence of a magnetic field can augment the electrostatic force, and therefore alter the overall reflection process. We hereafter refer to the effect of the magnetic field on the dynamics of the ion reflection process as "magnetic deflection" (We note that particle paths and the associated reflection and transmission must be frame independent, whereas the **E** and **B** fields are frame-dependent. We work in the shock normal frame unless otherwise stated). Magnetic deflection has been investigated previously but in limited ways [*Leroy et al.*, 1981, 1982; *Leroy*, 1983; *Lever et al.*, 2001; *Burgess et al.*, 1989; *Gedalin*, 1996]. *Leroy* [1983] proposed a model for the ion motion across a shock by analyzing the ion trajectory in separate regions of the foot and ramp, and having the ions specularly reflected at the top of the ramp. The model predicts that α increases with M_A, in contrast to the purely specular reflection model which would predict the opposite behavior, i.e. α decreasing with increasing M_A, due to $\Delta\phi_E$ decreasing with increasing M_A [*Dimmock et al.*, 2012]. This anti-correlation between α and $\Delta\phi_E$ is well known [*Gosling and Robson*, 1985; *Goodrich*, 1985] but an analytic model to explain this discrepancy has yet been proposed. *Leroy* [1983] also acknowledged that magnetic deflection plays an important role in the ion dynamics at supercritical shocks and was likely responsible for this discrepancy.

It is important to distinguish these reflected thermal ions that are initially reflected at the shock front and then transmitted downstream, a generalization of specularly reflection ions, from another class of reflected particles, namely ions that are initially transmitted through the shock by overcoming the electrostatic potential barrier but subsequently return to the shock due to their downstream gyromotion. We refer to this class of particles as “returning ions” and note that their properties have been studied in detail by *Gedalin* [1996]; they are not analyzed in this Chapter. Nor are nonthermal ions subject to shock-drift acceleration or diffusive shock acceleration considered here. The problem of the anti-correlation between α and $\Delta\phi_E$ relates only to ions immediately reflected at the shock ramp and not to returning ions.

The evolving dynamics of the ion motion through the shock with increasing M_A has also been noted. *Lee et al.* [1996] stated that for supercritical shocks, the ion motion is no longer a specular reflection, but is rather a “turning” motion until it is either reflected or transmitted. This turning motion is evidenced by the deceleration of the ion velocity in v_y across the foot, observed in both 1-D hybrid and PIC simulations [*Leroy et al.*, 1981, 1982; *Burgess et al.*, 1989; *Gedalin*, 1996; *Yuan et al.*, 2007]. *Leroy et al.* [1981] explained this deceleration by considering the fluid equation of motion for ions including the $\mathbf{v} \times \mathbf{B}$ force,

$$m_i \frac{dv_y}{dt} = e(u_x - v_x)B_z \tag{3.5}$$

where m_i is the ion mass, u_x is the local fluid speed and v_x is the particle's normal speed. The presence of any reflected ions in the region of the shock foot would reduce u_x locally, resulting in $u_x < v_x$ and therefore from (3.5) a negative force in the y direction would be applied to the incoming ions. However, it was not determined whether this turning motion would reduce or enhance the reflection process.

This Chapter develops and proposes a new model for the initial reflection or transmission of thermal ions at collisionless shock fronts. Specifically we

(1) derive the reflection condition using the new model, (2) quantify and investigate magnetic deflection using the new model and both test-particle and 1-D hybrid simulations, (3) show that particle gyromotion causes the reflection cutoff to rotate in velocity phase space depending on M_A and the overall shock thickness, (4) demonstrate the new model's applicability, (5) present 1-D hybrid simulation measurements of a new effective potential $\Delta\phi$ and of α with M_A, (6) show that magnetic deflection is a vital aspect of the ion reflection process and shock behavior for large M_A, and (7) explain the anti-correlation of α and ϕ_E.

The Chapter is organized as follows. In Section 2 we outline relevant analytic theory. The new reflection model is developed and compared in Section 3 with test-particle simulations in Section 4. We test the model with 1-D hybrid simulations in Section 5. Sections 6 and 7 discuss the results and conclude the Chapter, respectively.

3.3 Theory

A theoretical expression for $\phi_E(x)$ can be derived from the electron momentum equation in the normal incidence frame (NIF) [*Leroy et al.*, 1981, 1982] where the shock is at rest and the normal direction is defined to be along the upstream plasma flow velocity. For a perpendicular shock,

$$e\phi_E(x) = e\int_{-\infty}^{x} u_y(x')B_z(x')\,dx' + \frac{\gamma}{\gamma-1}\frac{P_e(x)}{n(x)} + \frac{B_1}{\mu_0 n_1}\left[B(x) - B_1\right] \tag{3.6}$$

where $P_e(x)$ is the local electron pressure and γ is the specific heat ratio. *Zank et al.* [1996] simplified this prediction by introducing a free parameter η_f to include the maximum contribution of first two terms to the last, and so the potential jump is

$$e\Delta\phi_E \simeq \eta_f m_i v_A^2\left(\frac{B_2}{B_1} - 1\right) \tag{3.7}$$

where B_2 is the downstream magnetic field strength. *Kuncic et al.* [2002] also derived a similar expression for $\Delta\phi$ but in the de Hoffmann-Teller frame (HTF),

$$e\Delta\phi_E^{HTF} \simeq \beta_{e\perp,1} m_i v_A^2\left(\frac{B_2}{B_1} - 1\right) \tag{3.8}$$

where $\beta_{e\perp,1}$ is the upstream perpendicular electron beta. The difference between the electric potential in the HTF and the NIF is due to the noncoplanar component of the magnetic field [*Goodrich and Scudder*, 1984],

$$e\phi_E^{HTF} = e\phi_E^{NIF} - \frac{u_{x1}}{c}\tan\theta_{Bn}\int_{-\infty}^{\infty} B_y \, dx \tag{3.9}$$

where c is the speed of light. Accordingly if $B_y = 0$, $\phi_E^{HTF} = \phi_E^{NIF}$ and then (3.7) and (3.8) can be equated. Normalizing (3.7) to the upstream ram energy gives the normalized electrostatic potential jump $\Delta\varphi_E = e\Delta\phi_E/(\frac{1}{2}m_i u_{x1}^2)$,

$$\Delta\varphi_E \simeq \frac{2\eta_f}{M_A^2}(r-1). \tag{3.10}$$

Here r is the R-H compression ratio, which for quasiperpendicular shocks asymptotes to 4 as $M_A \to \infty$. However the denominator can grow without bound, implying $\Delta\varphi_E \to 0$ as $M_A \to \infty$. Recent Cluster spacecraft observations [*Dimmock et al.*, 2012] of multiple terrestrial bow shock encounters between $M_A \sim 2-10$ suggest a similar trend to (3.10).

The reflection efficiency for a specular reflection model α^E can be derived assuming a Maxwellian distribution [*Zank et al.*, 1996],

$$\alpha^E = \frac{1}{2}\text{erfc}\left(\frac{u_{x1}-v_c^E}{\sqrt{2}v_{th1}}\right) \tag{3.11}$$

where $\text{erfc}(x) = 1 - 2/\pi^{1/2}\int_0^x e^{-t^2}dt = 1 - \text{erf}(x)$ is the complementary error function and $v_{th1} \equiv (k_B T_{i1}/m_i)^{1/2}$ is the upstream ion thermal speed where T_{i1} is the upstream ion temperature. In normalized parameters,

$$\alpha^E = \frac{1}{2}\text{erfc}\left[\frac{M_A}{\beta_i^{1/2}}\left(1-\sqrt{\Delta\varphi_E}\right)\right] \tag{3.12}$$

since the upstream ion beta $\beta_i = 2v_{th1}^2/v_A^2$ and $\sqrt{\Delta\varphi_E} = v_c^E/u_{x1}$.

3.4 New model for ion reflection and transmission

To analyze the dynamics of the ion reflection process, we examine the change in an ion's normal kinetic energy across the shock layer, W_{Tx}, in terms of the work done in the x direction by the electric field W_{Ex} and the magnetic field W_{Bx} along its trajectory,

$$W_{Tx} = W_{Ex} + W_{Bx} = \int_0^L F_x \, dx, \tag{3.13}$$

for a perpendicular shock with width L. Here

$$F_x = e(\mathbf{E} + \mathbf{v} \times \mathbf{B}) \cdot \hat{x}, \tag{3.14}$$

$$W_{Tx} = \frac{1}{2} m_i \left[v_{x2}^2 - v_{x1}^2 \right], \tag{3.15}$$

$$W_{Ex} = e \int_0^{t_2} dt \; v_x(t) E_x[x(t)] \leq -e\Delta\phi_E, \tag{3.16}$$

$$W_{Bx} = e \int_0^{t_2} dt \; v_x(t) v_y(t) B_z[x(t)], \tag{3.17}$$

where the transmission time, t_2, is the time it takes for the ion, entering the shock with initial velocity $\mathbf{v}_1$, to reach the downstream edge of the shock having a final velocity of $\mathbf{v}_2 = (v_{x2}, v_{y2}, v_{z2})$. Note the total work done (summed over all 3 directions) by the magnetic field is zero since the velocity is always perpendicular to the direction of the magnetic force, i.e., $\mathbf{v} \cdot (\mathbf{v} \times \mathbf{B}) = 0$ or $W_{By} = -W_{Bx}$. However, we recognize here that the motion in the x direction is of primary importance for understanding the reflection process. We now derive a generalized model for specular reflection which includes magnetic field effects. We then use the new model to derive a modified reflection condition and show that it depends on the parameters, the maximum reflection time and total effective potential.

3.4.1 A magnetic deflection mechanism

In order for (3.17) to correspond to a net deceleration of the ion distribution, meaning a magnetic deflection mechanism, we require that the average contribution of W_{Bx} for the ion distribution is negative, i.e.,

$$\langle W_{Bx} \rangle = \int_{-\infty}^{\infty} dv_{x1} \int_{-\infty}^{\infty} dv_{y1} \; W_{Bx}(v_{x1}, v_{y1}) f(v_{x1}, v_{y1}) < 0 \tag{3.18}$$

where $f(v_{x1}, v_{y1})$ is the distribution function. Here we derive predictions for the average deflections in v_x and v_y due to magnetic and electric forces, which leads to a prediction for $\langle W_{Bx} \rangle$.

Consider an ion at the center of the distribution entering the shock at the upstream fluid velocity $\mathbf{u}_1 = (u_{x1}, 0, 0)$. Let $X(t)$ and $\mathbf{V}(t) = (V_x(t), V_y(t), V_z(t))$

be this particle's position and velocity through the shock, respectively. We choose linear profiles of the magnetic field and normal velocity along the ion's trajectory across the shock as a function of time,

$$B_z[X(t)] = B_1\left[(r_B-1)\frac{t}{T_2}+1\right] \tag{3.19}$$

$$V_x(t) = u_{x1}\left[\left(\frac{1}{r_v}-1\right)\frac{t}{T_2}+1\right] \tag{3.20}$$

where T_2 is its transmission time and its downstream magnetic field strength and downstream normal velocity are related to their upstream quantities through the magnetic enhancement ratio r_B and normal velocity ratio r_v respectively, i.e., $B_z[X(T_2)] = B_2 = r_B B_1$ and $V_x(T_2) = u_{x1}/r_v$. A justification for (3.20) is provided in Section 5 below. Integrating (3.20) from $t=0$ to $t=T_2$ yields

$$T_2 = 2L\left(u_{x1}+\frac{u_{x1}}{r_v}\right)^{-1}. \tag{3.21}$$

We can now obtain an expression for $V_y(t)$ using the ion equation of motion in y,

$$V_y(t) = \frac{e}{m_i}\int_0^t dt'\,[u_{x1}B_1 - V_x(t')B_z[X(t')]] \tag{3.22}$$

where $E_y = u_{x1}B_1$. Substituting (3.19) and (3.20) into (3.22) and writing $C_1 = r_B - 1$ and $C_2 = 1/r_v - 1$ yields,

$$\begin{aligned} V_y(t) &= \frac{e}{m_i}\int_0^t dt'\,\Bigg[u_{x1}B_1 - \\ &\qquad u_{x1}B_1\left(C_1\frac{t'}{T_2}+1\right)\left(C_2\frac{t'}{T_2}+1\right)\Bigg] && (3.23)\\ &= -\frac{eB_1}{m_i}u_{x1}\int_0^t dt'\,\left[C_1C_2\frac{t'^2}{T_2^2}+(C_1+C_2)\frac{t'}{T_2}\right]\\ &= -u_{x1}\Omega_{ci}\left[C_1C_2\frac{t^3}{3T_2^2}+(C_1+C_2)\frac{t^2}{2T_2}\right]. && (3.24)\end{aligned}$$

For a cold plasma we can approximate the downstream fluid velocity $\mathbf{u}_2 = (u_{x2}, u_{y2}, u_{z2})$ as this ion's downstream velocity, i.e., $\mathbf{u}_2 = \mathbf{V}(T_2)$. Thus substituting $t = T_2$ in (3.24) gives

$$u_{y2} = -u_{x1}\Omega_{ci}T_2\left[\frac{C_1C_2}{3}+\frac{C_1+C_2}{2}\right]. \tag{3.25}$$

We can obtain a normalized expression for (3.25) by substituting in (3.21), yielding

$$\frac{u_{y2}}{v_A} = -\frac{l}{3}\left[\frac{2r_B + r_B r_v + 1 - 4r_v}{r_v + 1}\right] \tag{3.26}$$

where $l = L/\lambda_i$ is the normalized shock width. Eq (3.26) can be rewritten as

$$\frac{u_{y2}}{v_A} = -\frac{l(r_v - 1)^2}{3(r_v + 1)} \tag{3.27}$$

for $r_B = r_v$ so that $u_{y2} \leq 0$ for $r_v \geq 1$. In general, one can show (3.26) is always less than zero if $r_B \geq r_v$, given $r_B > 1$ and $r_v > 1$. This implies that the ion distribution is accelerated in the negative v_y direction, in agreement with previous hybrid simulations [*Leroy*, 1983; *Burgess et al.*, 1989; *Yuan et al.*, 2007]. This deflection in v_y arises because in the shock layer $B_z[X(t)]$ and $V_x(t)$, in general, are monotonically increasing and decreasing functions, respectively, and therefore the time-integrated $\mathbf{v} \times \mathbf{B}$ force in the y-direction is no longer balanced by the convection electric field $\mathbf{E}$. The local maximum of (3.26) occurs at $r_B = r_v$, meaning that the ion distribution is deflected more if $r_B > r_v$. This is important since the maximum magnetic enhancement ratio measured in 1-D hybrid simulations is much larger than the R-H prediction in the shock layer, specifically $r_B \simeq B_o/B_1 \propto M_A$ [*Tiu et al.*, 2011].

We now consider how this acceleration in v_y can be translated into a deceleration in v_x via the $\mathbf{v} \times \mathbf{B}$ force, with

$$\Delta u_x^B = \frac{e}{m_i}\int_0^{T_2} dt\ V_y(t) B_z[X(t)]. \tag{3.28}$$

The average velocity shift in v_x can be estimated by applying the trapezoidal rule to (3.28), yielding

$$\Delta u_x^B \simeq \frac{e}{m_i} u_{y2} B_2 \frac{T_2}{2} \tag{3.29}$$

$$\simeq \frac{1}{2}\Omega_{ci} r_B T_2 u_{y2} \tag{3.30}$$

and showing that the average velocity shift in x is proportional to u_{y2} and therefore is negative for $r_B \geq r_v$. In normalized units (3.30) is

$$\frac{\Delta u_x^B}{v_A} \simeq -\frac{r_B r_v l^2}{3M_A}\left[\frac{2r_B + r_B r_v + 1 - 4r_v}{(r_v + 1)^2}\right]. \tag{3.31}$$

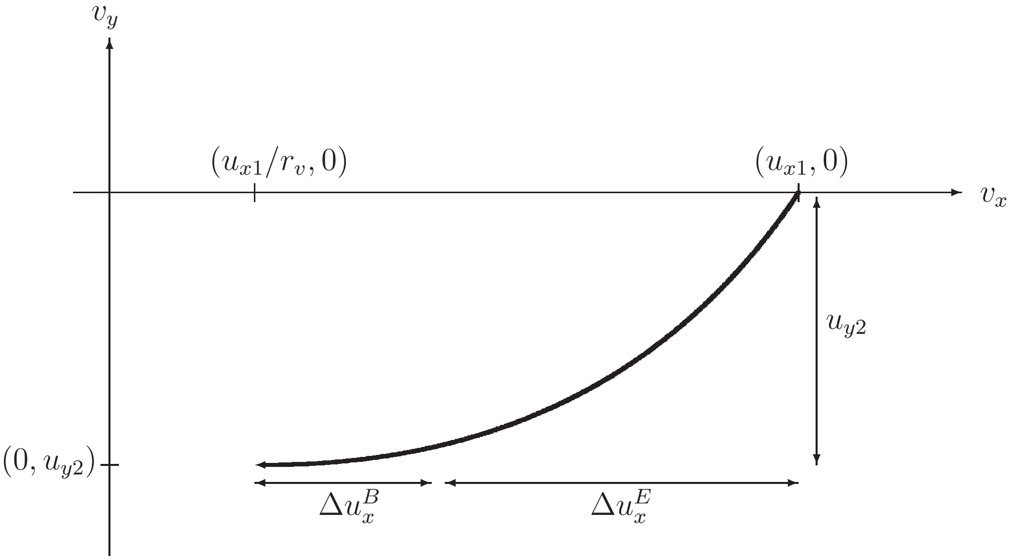

Figure 3.1: The ion distribution is decelerated from its upstream flow velocity $(u_{x1}, 0, 0)$ to its downstream flow velocity $(u_{x1}/r_v, u_{y2}, 0)$ where the spatially-varying fluid velocity moves along the solid curve in $v_x - v_y$ phase space. The deceleration of the ion distribution can be decomposed into a combined deceleration in v_x by electrostatic deceleration, Δu_x^E, and magnetic deflection, Δu_x^B, and an acceleration u_{y2} in v_y due to magnetic deflection.

Therefore the total velocity shift in x

$$\Delta u_x = u_{x2} - u_{x1} = \Delta u_x^E + \Delta u_x^B \tag{3.32}$$

consists of the deceleration associated with the velocity shift in y via (3.31), plus the deceleration from the electrostatic potential $\Delta\phi_E$, with

$$\Delta u_x^E = \left(u_{x1}^2 - \frac{2e\Delta\phi_E}{m_i} \right)^{1/2} - u_{x1}. \tag{3.33}$$

The deceleration of the ion distribution is represented schematically in Figure 3.1 in $v_x - v_y$ phase space which can be decomposed into a combined deceleration in v_x by electrostatic deceleration (Δu_x^E) and by magnetic deflection (Δu_x^B), and an acceleration in v_y due to magnetic deflection (u_{y2}).

3.4.2 A total effective potential

Consider now the change in the average kinetic energy of the ion distribution in terms a total effective potential

$$e\Delta\phi = e\Delta\phi_E - \langle W_{Bx}\rangle \tag{3.34}$$

where $\langle W_{Bx}\rangle$ corresponds to magnetic deflection effects. We estimate

$$\langle W_{Bx}\rangle = e\int_0^{T_2} dt\ V_x(t)V_y(t)B_z[X(t)]. \tag{3.35}$$

This can be approximated using the trapezoidal rule as

$$\begin{aligned}\langle W_{Bx}\rangle &\simeq e u_{x2}u_{y2}B_2\frac{T_2}{2} && (3.36)\\ &\simeq \left(\frac{1}{2}m_i u_{x1}^2\right)\frac{r_B}{r_v}\Omega_{ci}T_2\frac{u_{y2}}{u_{x1}} && (3.37)\\ &\simeq -\left(\frac{1}{2}m_i u_{x1}^2\right)\frac{r_B}{r_v}\Omega_{ci}^2T_2^2\left[\frac{C_1C_2}{3}+\frac{C_1+C_2}{2}\right]. && (3.38)\end{aligned}$$

In normalized units

$$\frac{\langle W_{Bx}\rangle}{\frac{1}{2}m_i u_{x1}^2} \simeq -\frac{2l^2}{3M_A^2}\left[\frac{2r_B^2+r_B^2r_v+r_B-4r_Br_v}{(r_v+1)^2}\right] \tag{3.39}$$

depends only on r_B, r_v and l. For finite $l > 0$ and $r_B \geq r_v$, $\langle W_{Bx}\rangle < 0$ and so the magnetic deflection mechanism always enhances the total effective potential $\Delta\phi > \Delta\phi_E$. For strong shocks $M_A \gg 1$, $r_v \to 4$ and $r_B \propto M_A$ [*Tiu et al.*, 2011] and so the leading term in (3.39) scales as $-l^2$. However, for a thin shock $l \approx 0$, $\langle W_{Bx}\rangle \approx 0$ and so magnetic deflection has little to no effect on the ion reflection process.

Suppose that across the shock layer the normal kinetic energy of the plasma is changed as stipulated by the R-H jump conditions. We then equate this change in bulk normal kinetic energy across the shock to an effective potential

$$e\Delta\phi = \frac{1}{2}m_i u_{x1}^2\left(1-\frac{1}{r^2}\right), \tag{3.40}$$

and in normalized units

$$\Delta\varphi = 1-\frac{1}{r^2}, \tag{3.41}$$

where $\Delta\varphi = e\Delta\phi/(\frac{1}{2}m_i u_{x1}^2)$ is the normalized effective potential. Equation (3.41) also places an upper bound for the effective cutoff speed

$$v_c = \sqrt{\frac{2e\Delta\phi}{m_i}} = u_{x1}\left(1-\frac{1}{r^2}\right)^{1/2} < u_{x1} \tag{3.42}$$

3.4.3 A new reflection cutoff

Now consider a thermal particle in an upstream ion distribution with initial velocity $\mathbf{v}_1 = (v_{x1}, v_{y1}, 0)$. We assume its motion can be decoupled into a deceleration due to the effective potential and a continued upstream gyromotion, i.e.,

$$v_x(t) = V_x(t) + v_{\perp 1} \cos(\Omega_{ci} t - \theta_1) \tag{3.43}$$

$$v_y(t) = V_y(t) - v_{\perp 1} \sin(\Omega_{ci} t - \theta_1). \tag{3.44}$$

The change in its normal kinetic energy as a function of time is

$$W_{Tx}(t) = \frac{1}{2} m_i v_x^2(t) - \frac{1}{2} m_i v_{x1}^2 \tag{3.45}$$

$$\begin{aligned} &= \frac{1}{2} m_i \left[V_x^2(t) - u_{x1}^2\right] + \frac{1}{2} m_i \big[u_{x1}^2 + \\ &\quad 2V_x(t) v_{\perp 1} \cos(\Omega_{ci} t - \theta_1) + \\ &\quad v_{\perp 1}^2 \cos^2(\Omega_{ci} t - \theta_1)\big] - \frac{1}{2} m_i v_{x1}^2. \end{aligned} \tag{3.46}$$

Using the result $\frac{1}{2} m_i [V_x^2(t) - u_{x1}^2] \geq -e\Delta\phi$ from (3.41), (3.46) implies

$$\begin{aligned} W_{Tx}(t) \geq{}& -e\Delta\phi + \frac{1}{2} m_i \big[u_{x1}^2 + 2V_x(t) v_{\perp 1} \cos(\Omega_{ci} t - \theta_1) \\ &+ v_{\perp 1}^2 \cos^2(\Omega_{ci} t - \theta_1)\big] - \frac{1}{2} m_i v_{x1}^2 \end{aligned} \tag{3.47}$$

$$\gtrsim -e\Delta\phi + \frac{1}{2} m_i v_{xu}^2(t) - \frac{1}{2} m_i v_{x1}^2 \tag{3.48}$$

where

$$v_{xu}(t) = u_{x1} + v_{\perp 1} \cos(\Omega_{ci} t - \theta_1) \tag{3.49}$$

is the particle's normal upstream gyromotion in the absence of the shock. If the work done during this gyromotion by the magnetic field in the x direction is

$$w_{Bx}(t) = \frac{1}{2} m_i \left[v_{xu}^2(t) - v_{x1}^2\right] \tag{3.50}$$

then (3.48) becomes

$$W_{Tx}(t) \gtrsim -e\Delta\phi + w_{Bx}(t). \tag{3.51}$$

In other words, we assume that during the period between when an ion first encounters the shock and its reflection or transmission (1) the work done by the magnetic field is $W_{Bx}(t) \gtrsim \langle W_{Bx} \rangle + w_{Bx}(t)$ and (2) the electric field modifies v_x in the usual unmagnetized manner, i.e., $W_{Ex}(t) \approx w_{Ex}(t)$ where

$$w_{Ex}(t) \leq -e\Delta\phi_E \tag{3.52}$$

is the work done by the electric field in the absence of the magnetic field. An ion is reflected if along its trajectory the work done by the fields in the x direction is equal to or greater than its initial normal kinetic energy, i.e.,

$$-e\Delta\phi + w_{Bx}(t_r) \lesssim -\frac{1}{2}m_i v_{x1}^2 \tag{3.53}$$

where the reflection time t_r depends on v_{x1} and v_{y1}. Eq (3.53) is the theoretical reflection condition; substituting (3.50) and (3.49) into (3.53) yields

$$v_{xu}(t_r) \lesssim v_c. \tag{3.54}$$

In the electrostatic case where $\mathbf{B} = 0$ one can show, through conservation of normal kinetic energy, that $t_r \propto v_{x1}$. This implies that ions with the maximum reflection time $\tau = \max(t_r)$ are found at the specular reflection cutoff $v_{x1} = v_c^E$. Likewise, we assume that

$$v_{xu}(\tau) \simeq v_c \tag{3.55}$$

is the theoretical separatrix for reflection, meaning the boundary between reflected and transmitted particles in initial phase space v_{x1} and v_{y1}. Using (3.1), (3.49) and $v_{y1} = v_{\perp 1}\sin\theta_1$, (3.54) can be rearranged into an equation for the reflection condition in terms of v_{x1} and v_{y1},

$$v_{y1} \simeq -\cot(\Omega_{ci}\tau)(v_{x1} - u_{x1}) + \csc(\Omega_{ci}\tau)(v_c - u_{x1}) \tag{3.56}$$

If the origin is $(u_{x1}, 0)$, then the parameters $m = -\cot(\Omega_{ci}\tau)$ and $b = \csc(\Omega_{ci}\tau)(v_c - u_{x1})$ describe the slope and intercept of the reflection cutoff, respectively. Note the important physical point that in general the reflection condition is not $v_{x1} \leq v_c^E$ but is rotated to be dependent on v_{y1}.

In the case of an infinitesimally thin shock $l = 0$ (3.39) gives $\langle W_{Bx} \rangle = 0$, implying that $v_c = v_c^E$. Furthermore $\tau = 0$, and so (3.56) reduces to the familiar specular reflection condition (3.4). For $\tau > 0$, (3.56) predicts an enhancement to the specular cutoff speed $v_c > v_c^E$ as well as the anticlockwise rotation about the origin by an angle $\Omega_{ci}\tau$ of the reflection cutoff $v_{x1} = v_c$. This implies that the ion dynamics across the shock can be modeled as a deceleration that is due to the electrostatic potential and magnetic deflection combined with a rotation due to its initial gyromotion.

Physically this rotation of the cutoff just corresponds to the particles gyrating about $\mathbf{B}$ as they move into the shock and are reflected. The perpendicular distance $h = b\sin(\Omega_{ci}\tau) = v_c - u_{x1}$ from the reflection cutoff to the origin remains constant regardless of τ. If the initial ion distribution $f(v_{x1}, v_{y1})$ is radially symmetric then the effective reflection efficiency is

$$\alpha_T = \int_{-\infty}^{\infty}\int_{-\infty}^{h} f(v_{x1}, v_{y1}) v_{x1} v_{y1}. \tag{3.57}$$

For a Maxwellian distribution, (3.57) reduces to the specular reflection prediction (3.12) but using $\Delta\varphi$ instead of $\Delta\varphi_E$,

$$\alpha_T = \frac{1}{2}\mathrm{erfc}\left[\frac{M_A}{\beta_i^{1/2}}\left(1 - \sqrt{\Delta\varphi}\right)\right]. \tag{3.58}$$

3.5 Test-particle simulation

We now test our new model with test-particle simulations in which the ion trajectories and velocities are integrated along a 1-D shock profile that is constant in time but has spatially varying 3-D electric and magnetic fields. The axes of the simulation are set up with the normal velocity and spatial profiles along $\hat{x}$, the convective electric field along $\hat{y}$, and the upstream magnetic field in the $x - z$ plane and primarily along $\hat{z}$. The simulations are conducted in the NIF with a stationary shock profile and fixed $M_A = 6$ and $\theta_{Bn} = 85°$. Figure 3.2 shows the 3 different spatial profiles of $B(x)$ we use in our test-particle simulations (these profiles are generalized and simplified from those of *Gedalin* [1996]). The magnetic field vector is given by $\mathbf{B}(x) = B(x)(\cos\theta_{Bn}, 0, \sin\theta_{Bn})$ where we ignore the out of plane component of $\mathbf{B}$ since its magnitude is small compared with B_2 or B_o [*Yuan et al.*, 2008a].

Firstly we use a laminar profile with a ramp only, represented in Figure 3.2(a), increasing monotonically from B_1 for $x \ll 0$ to B_2 at $x \gg 0$,

$$B(x) = B_1 + \frac{1}{2}(B_2 - B_1)\left[1 + \tanh\left(\frac{6x}{L_r}\right)\right]. \tag{3.59}$$

Here L_r is the ramp width and also the total shock width, defined to be the distance between the leading edge of the ramp ($x = -L_r/2$) and the trailing

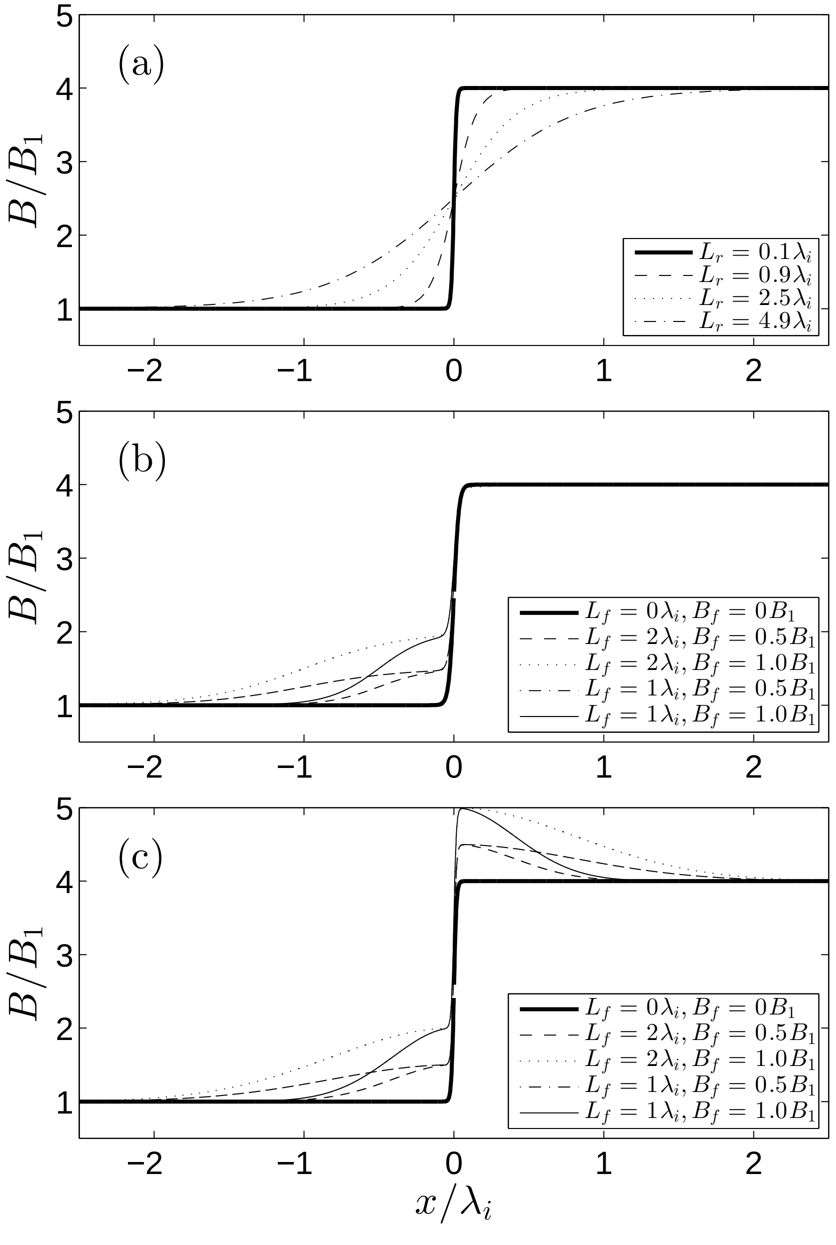

Figure 3.2: Profiles of the magnetic field used in the test-particle simulations: (a) ramp only, (b) a foot and ramp, and (c) a foot, ramp, and overshoot.

edge of the ramp ($x = L_r/2$). Figure 3.2(a) plots (3.59) for $L_r/\lambda_i = 0.1, 0.9, 2.5$ and 4.9.

Secondly, we use a profile with foot and ramp structures, shown in Figure 3.2(b) with

$$B(x) = B_1 + \frac{1}{2}(B_2 - B_f - B_1)\left[1 + \tanh\left(\frac{6x}{L_r}\right)\right] + \\ \frac{1}{2}B_f\left[1 + \tanh\left(\frac{6(x + L_f/2)}{L_f}\right)\right]. \tag{3.60}$$

Here L_f and B_f are the length scale and magnitude of the foot, respectively, and the spatial regions of the profile are divided into the foot ($x = -L_f$ to $x = 0$) and the ramp ($x = 0$ to $x = L_r$). Therefore the total shock width is $L = L_f + L_r$, which is the distance from the leading edge of the foot to the trailing edge of the ramp. Figure 3.2(b) plots (3.60) for $L_f = 1.0\ \lambda_i$ and $2.0\ \lambda_i$ and $B_f = 0.5\ B_1$ and $1.0\ B_1$.

Thirdly, we use a profile with a foot, ramp, and overshoot, shown in Figure 3.2(c) and modelled with

$$B(x) = B_1 + \frac{1}{2}(B_2 - B_1)\left[1 + \tanh\left(\frac{6x}{L_r}\right)\right] + \\ B_f \exp\left(\frac{-3x^2}{L_f^2}\right) \tag{3.61}$$

where the maximum magnetic field strength is $B_o = B_2 + B_f$. Likewise, the spatial profile is divided between the foot ($x = -L_f$ to $x = 0$), ramp ($x = 0$ to $x = L_r$) and overshoot ($x = L_r$ to $x = L_f$), and the total shock width is $L = L_f + L_r$, the distance from the leading edge of the foot to the end of the overshoot. Figure 3.2(c) plots (3.60) for values of $L_f = 1.0\ \lambda_i$ and $2.0\ \lambda_i$ and $B_f = 0.5\ B_1$ and $1.0\ B_1$.

In each simulation the profile of the electrostatic potential mimics $B(x)$ via

$$\phi_E(x) = \Delta\phi_E\left(\frac{B(x) - B_1}{B_2 - B_1}\right), \tag{3.62}$$

for instance by analogy with *Kuncic et al.* [2002], and the electric field has components $\mathbf{E}(x) = (-d\phi_E(x)/dx, u_{x1}B_1 \sin\theta_{Bn}, 0)$. The parameters $\Delta\phi_E$ and τ are varied in this investigation, where the former is directly controlled and the latter is controlled indirectly by varying the total shock width L. The upstream ion distribution has initial velocities between $\theta_1 = 0°$ and $360°$ and $v_{\perp 1} = 0$ and $2\ v_A$ and is injected at the leading edge of the foot or ramp.

3.5.1 Analysis for a ramp only

For the laminar profile we performed simulations with fixed $B_d = 4B_0$ but varying $\Delta\phi_E$ corresponding to cutoff speeds $v_c^E/v_A = 5$, 6, and 7, and $l_r = L_r/\lambda_i = 0.1$, 0.4, 0.9, 1.6, 2.5, 3.6, and 4.9. In Section 3's derivation of our new model we considered first the trajectory of a particle at the drift center of the ion distribution. In the same way we study test-particles entering the shock with $\mathbf{v}_1 = (6v_A, 0, 0)$ for simulations with $M_A = 6$, $v_c^E = 6v_A$ and $l_r = 0.1$, 0.9, 2.5, and 4.9. For each particle we calculate $W_{Tx}(t)$ using $v_x(t)$, $W_{Ex}(t)$ and $W_{Bx}(t)$ from the prescribed electric and magnetic fields, and $w_{Bx}(t)$ from v_{x1} and v_{y1}, using (3.15), (3.16), (3.17), and (3.50) respectively. We also calculate $w_{Ex}(t)$ in a separate test-particle simulation for which $\mathbf{E}$ is the same but $\mathbf{B} = 0$. We normalize $W_{Tx}(t)$, $W_{Bx}(t)$, $W_{Ex}(t)$, $w_{Bx}(t)$, and $w_{Ex}(t)$ to the particle's initial normal kinetic energy $\frac{1}{2}m_i v_{x1}^2$ and plot them as a function of time in Figure 3.3. We see that W_{Ex} is very well approximated by its unmagnetized counterpart w_{Ex} through the shock. The time t_p indicated by the dashed vertical line is when $W_{Tx}(t_p) = -0.98(\frac{1}{2}m_i v_{x1}^2)$. Given that this particle has $v_{\perp 1} = 0$ and so $w_{Bx} = 0$ and $W_{Bx} \approx \langle W_{Bx}\rangle$; the final value of $W_{Bx}(t)$, taken to be $W_{Bx}(t_p)$, represents the work done by the magnetic deflection mechanism.

For the same input parameters as these test-particle simulations, $r_v = r_B = B_2/B_1 = 4$ and $M_A = 6$, (3.39) yields

$$\frac{\langle W_{Bx}\rangle}{\frac{1}{2}m_i u_{x1}^2} \simeq -\frac{2l_r^2}{75} \tag{3.63}$$

when we assume $l = l_r$, and

$$\frac{\langle W_{Bx}\rangle}{\frac{1}{2}m_i u_{x1}^2} \simeq -\frac{l_r^2}{150} \tag{3.64}$$

for $l = l_r/2$. By way of contrast we plot $W_{Bx}(t_p)$ as a function of l_r against (3.63) and (3.64) in Figure 3.4. We see that (3.63) greatly overpredicts the work done by magnetic deflection but (3.64) gives comparable values to the test-particle results. The substitution $l = l_r/2$ is justified by noting that the linear portion of the magnetic profiles in Figure 3.2(a) are primarily between $x = -L_r/4$ and $x = L_r/4$ and also that $B_z(-L_r/4)/B_0 \approx 1.14$ and $B_z(L_r/4)/B_0 \approx 3.86$. Using the values of $W_{Bx}(t_p)$ to calculate $\Delta\phi$ from (3.34) and therefore v_c from (3.42) shows that the effective cutoff speed will be little modified from the specular cutoff speed for $l_r \leq 2.5$; specifically $v_c \leq 1.04 v_c^E$.

We now test how well (3.56) matches the true reflection cutoff in initial phase space for varying $\Delta\phi_E$ and $l_r \leq 2.5$ where $v_c \simeq v_c^E$ in these simulations.

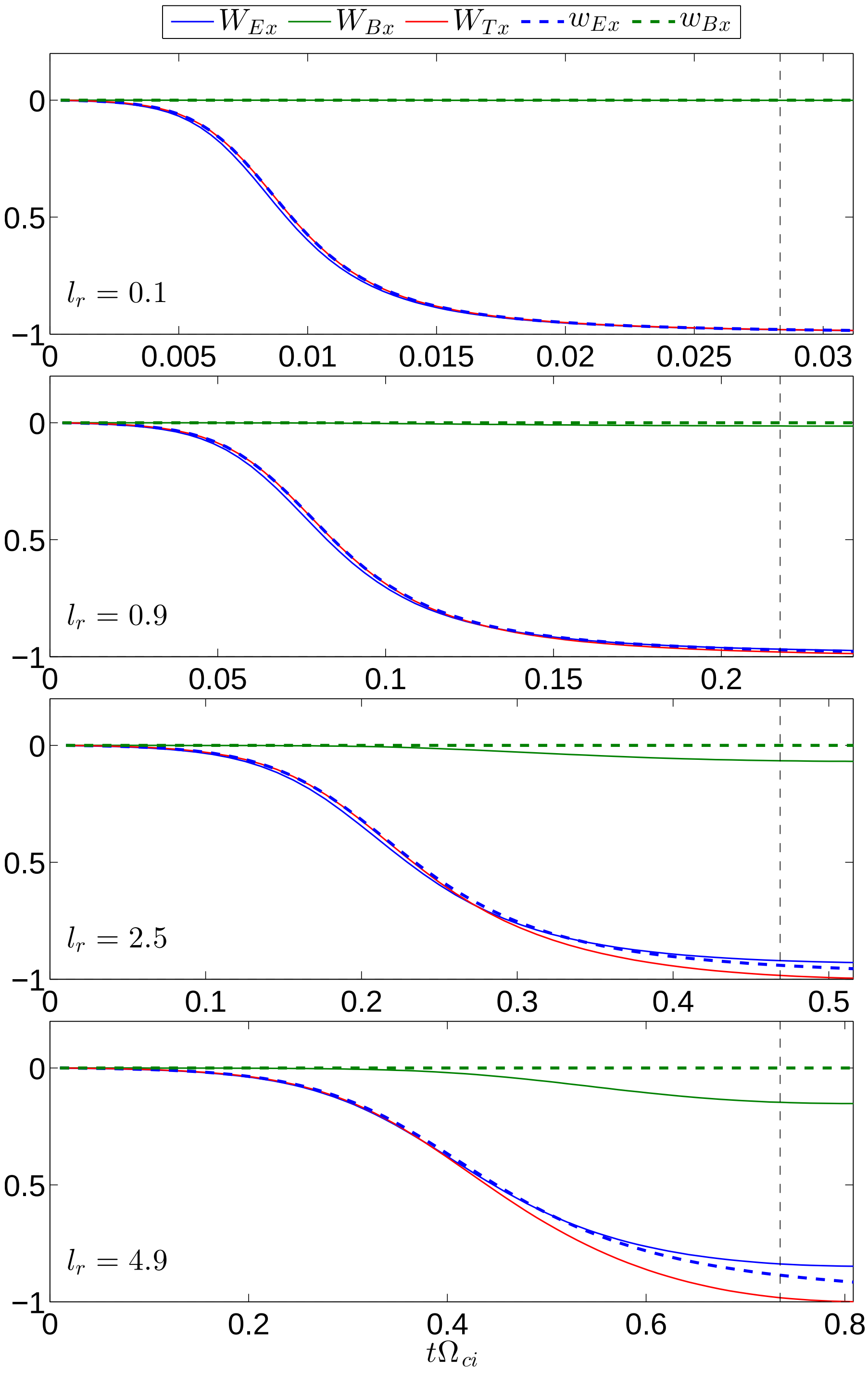

Figure 3.3: For an ion at the initial fluid speed $(u_{x1}, 0, 0)$ entering a laminar shock profile of various l_r (Figure 3.2), the quantities $W_{Tx}(t)$, $W_{Ex}(t)$, $W_{Bx}(t)$, $w_{Bx}(t)$ and $w_{Ex}(t)$ are plotted along its trajectory. The dashed vertical line indicates when $W_{Tx} = -0.98(\frac{1}{2}m_i u_{x1}^2)$.

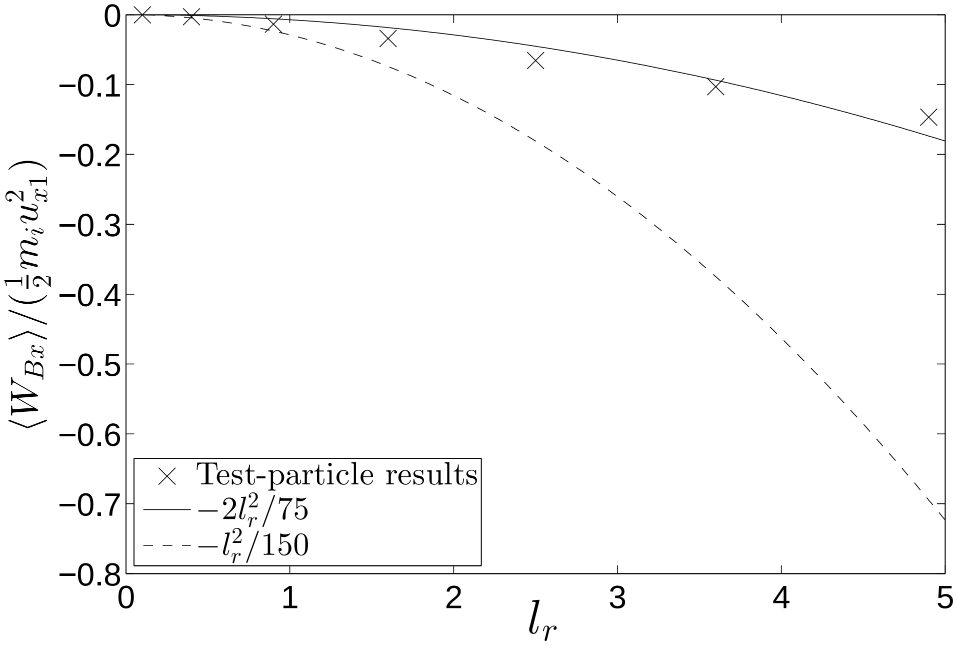

Figure 3.4: The normalized work done by magnetic deflection for the particle in Figure 3.3 as a function of l_r. This is compared to the theoretical predictions (3.63) (dashed line) and (3.64) (solid line).

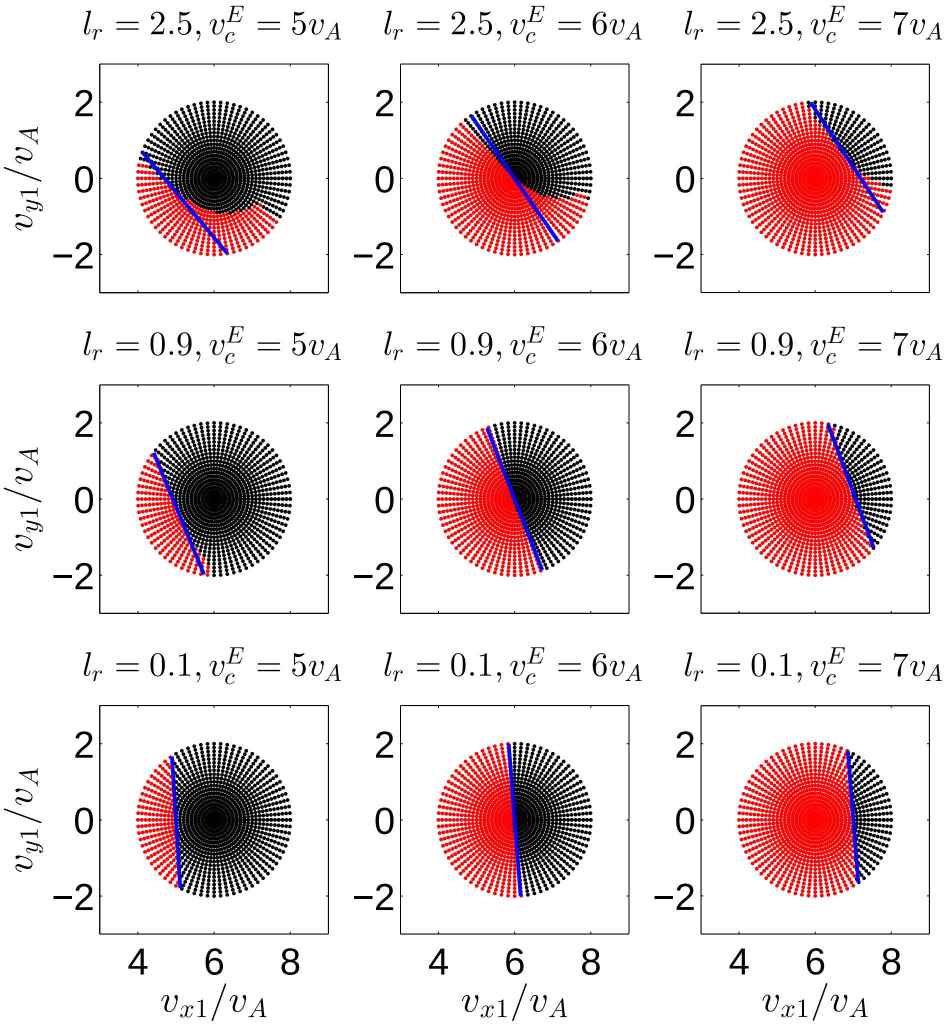

Figure 3.5: Multiple scatter plots of reflected (red) and transmitted (black) ions in test-particle simulations with only a ramp and varying l_r and v_c^E. The blue lines plot (3.56), the theoretical reflection cutoff from our model.

In the test-particle simulations, reflected ions are identified as those which have a positive change in their normal kinetic energy, i.e. $W_{Tx}(t) > 0$, across the shock profile. The maximum reflection time τ is calculated from this sample of reflected ions. Figure 3.5 plots the reflected (red) and transmitted (black) particles as a function of their initial velocities v_{x1} and v_{y1} for different $\Delta\phi_E$ and L_r. From left to right $\Delta\phi_E$ increases in magnitude, corresponding to specular cutoff speeds $v_c^E/v_A = 5, 6$, and 7. From bottom to top the shock width increases, with $L_r/\lambda_i = 0.1, 0.9$ and 2.5. Qualitatively, Figure 3.5 shows that h, the perpendicular distance from the origin $(u_{x1}, 0)$ to the reflection cutoff, is constant for fixed $\Delta\phi_E$ but varying L_r. Specifically $h \approx -v_A, 0$ and v_A, for test-particle simulations with $v_c^E/v_A = 5, 6$, and 7, respectively. This is consistent with the theoretical prediction $h = v_c - u_{x1}$. Figure 3.5 also shows that the angle of rotation $\Omega_{ci}\tau$ increases with L_r but is independent of $\Delta\phi_E$. This suggests that the location and rotation of the reflection cutoff are independent of each other, consistent with the theoretical reflection cutoff derived in (3.56).

As a comparison, we plot (3.56) in Figure 3.5 (indicated by the blue lines) using the empirically determined τ and $v_c = v_c^E$, showing extremely good agreement with the test-particle results except at large $L_r = 2.5\ \lambda_i$ where extra reflected particles occur. This confirms that v_c^E is little modified for these values of L_r. Analysis of the motions of the extra reflected particles (not shown) suggests that they are returning ions, that is, these particles are firstly transmitted through the shock into the downstream region and then return back upstream as part of their downstream gyromotion.

3.5.2 Analysis for profiles with a foot and ramp

Recent Cluster spacecraft measurements of the ramp thickness at the terrestrial bow shock suggest L_r is on the order of the electron inertial length $\lambda_e = c/\omega_{ce}$ [*Mazelle et al.*, 2010; *Hobara et al.*, 2010]. At these scales magnetic deflection and the rotation of the reflection cutoff would be unimportant, as shown by the test-particle simulation for $L_r = 0.1\lambda_i$ in Figure 3.5. However, calculations of the foot length from hybrid and PIC simulations [*Gedalin*, 1996; *Gosling et al.*, 1982; *Schwartz et al.*, 1983] and older spacecraft measurements [*Livesey et al.*, 1984; *Balikhin et al.*, 1995] suggest $L_f \gtrsim \lambda_i$, which could increase τ and therefore produce an observable rotation.

We test this hypothesis by using a narrow ramp profile, $L_r = 0.1\ \lambda_i$, fixed $B_2 = 4\ B_1$ and $v_c = 6v_A$, but varying foot length ($L_f = 0.5\ \lambda_i$ and $1.0\ \lambda_i$)

and magnitude ($B_f = 0.5\ B_1$ and $1.0\ B_1$). Figure 3.6 plots the initial phase space of reflected (red) and transmitted (green and black) ions using these foot and ramp profiles. Qualitatively, we observe a rotation in the reflection cutoff due to the finite width of the foot, since the degree of rotation increases with L_f. Moreover, the theoretical prediction (3.56) with $v_c = v_c^E$ (blue lines) is consistent with the reflection cutoff that is observed. However, increasing B_f has no noticeable effect on the reflection cutoff for the same L_f, as expected since this quantity does not enter the prediction (3.56). These results show that the finite width of the magnetic profile, regardless of whether it be in the foot or the ramp, produces an appreciable rotation in the reflection cutoff.

3.5.3 Analysis for profiles with a foot, ramp and overshoot

We use the same parameters for the foot and ramp cases in Section 4.2 but add an overshoot with the same magnitude and length as the foot. In the same manner, we vary the length ($L_f = L_o = 0.5\ \lambda_i$ and $1.0\ \lambda_i$) and magnitude ($B_f = B_o = 0.5\ B_1$ and $1.0\ B_1$) of the foot and overshoot. Figure 3.6 plots the initial phase space separated into reflected (red and green) and transmitted (black) particles from these foot, ramp and overshoot profiles. On inspection, the rotation of the cutoff remains unchanged compared to the foot and ramp profiles, as evidenced by the slopes being the same for the foot-ramp and foot-ramp-overshoot cases. Clearly the rotation depends only on the distance from the leading edge of the foot to the location of the overshoot; in this case $L = L_f + L_r$. However, the location of the cutoff has shifted to the right, since $\Delta\phi_E$ increases by a factor of $(B_2 + B_o - 1)/(B_2 - 1)$ because of the overshoot, from (3.62). Accordingly, we account for this change when calculating the theoretical cutoff (blue lines) and once again find excellent agreement with the true reflection cutoff in Figure 3.6.

3.5.4 Analytic expression for τ

Does τ, and therefore the rotation, depend only on the total shock width L? Ignoring the magnetic field, let x_r be the distance a specular reflected particle travels from the leading edge of the foot or ramp until its reflection, defined as when $v_x < 0$. Then

$$x_r = \int_0^{t_r} v_x(t)\ dt \simeq \frac{1}{2} v_{x1} t_r. \tag{3.65}$$

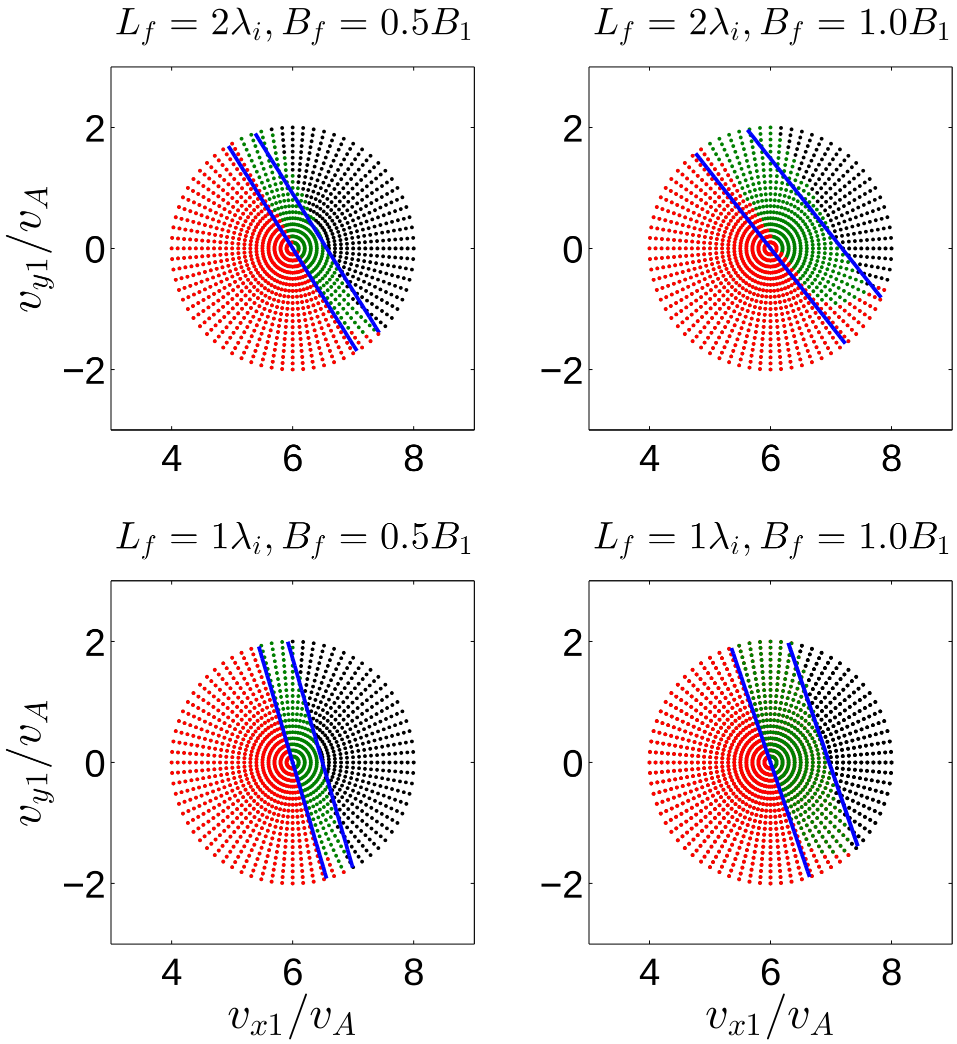

Figure 3.6: Scatter plots of reflected (red) and transmitted (green and black) ions in test-particle simulations with a foot and ramp profile and varying L_f and B_f. Adding an overshoot gives reflected (red and green) and transmitted (black) ions. The blue lines show (3.56), the theoretical reflection cutoff from our model without (left) and with (right) an overshoot.

If $\phi_E(x)$ is a linear function from $\phi_E(0) = 0$ to $\phi_E(L) = \Delta\phi$, i.e., $\phi_E(x) \approx \Delta\phi_E x/L$, then energy conservation implies $\Delta\phi_E x_r/L \approx \frac{1}{2}m_i v_{x1}^2$, whence

$$x_r \approx \left(\frac{v_{x1}}{v_c^E}\right)^2 L. \tag{3.66}$$

Equating (3.65) and (3.66) and solving for t_r gives

$$t_r = \frac{2v_{x1}}{(v_c^E)^2}L, \tag{3.67}$$

implying that in the source region of reflected particles, $v_{x1} < v_c^E$, the maximum reflection time τ must occur at the specular reflection separatrix $v_{x1} = v_c^E$, with

$$\tau = \frac{2L}{v_c^E}. \tag{3.68}$$

For test-particle simulations with the laminar profile (3.59) we measured τ as a function of L, v_c^E and B_2. We find $\tau \propto m_\tau L/v_c^E$ with m_τ a function of the magnetic profile. The values of m_τ are summarized in Table 3.1 for different values of v_c^E and B_2. A regression analysis of m_τ in B_2 shows

$$m_\tau \simeq A_1\frac{B_2}{B_1} + A_2 \tag{3.69}$$

where $A_1 \approx 0.33 \pm 0.01$ and $A_2 \approx 0.47 \pm 0.03$, where the errors are 95% confidence bounds. For $B_2 = 4B_1$, (3.69) gives $m_\tau \approx 1.8 \pm 0.1$ which is close to the value of 2 in the electrostatic case in (3.68). Thus (3.68) is a reasonable prediction for τ, thereby providing an analytic prediction for the rotation of the reflection separatrix (3.56).

3.6 1-D hybrid simulation

Although the test-particle simulations show excellent agreement with the theoretical reflection cutoff (3.56), values for $\Delta\phi_E$ and L need to be specified. In this section we perform 1-D hybrid simulations to obtain self-consistent values of $\Delta\phi_E$ and $\langle W_{Bx}\rangle$ as a function of M_A and as a result examine the relative importance of each mechanism in the total ion reflection process. Similarly we compare the theoretical reflection cutoff (3.56) with the hybrid simulation results. We use a 1-D hybrid simulation code [*Yuan et al.*, 2007, 2008a]

Table 3.1: m_τ recorded for test-particle simulations with a ramp only profile (the errors are 95% confidence bounds).

v_c^E/v_A	B_2/B_1	m_τ
5	1	0.79 ± 0.04
6	1	0.79 ± 0.03
7	1	0.80 ± 0.03
5	2	1.13 ± 0.03
6	2	1.10 ± 0.02
7	2	1.12 ± 0.02
5	3	1.44 ± 0.03
6	3	1.45 ± 0.02
7	3	1.44 ± 0.05
5	4	1.71 ± 0.11
6	4	1.77 ± 0.07
7	4	1.83 ± 0.04

with time step $\Delta t = 10^{-4}\Omega_{ci}^{-1}$, grid spacing $\Delta x = 0.05\lambda_i$, applied resistivity $\eta = 0.01\mu_0 v_{\mathrm{A}}^2 \Omega_{ci}^{-1}$, $\beta_e = \beta_i = 0.5$, and $\theta_{Bn} = 85°$. We performed multiple simulations with $M_A \sim 1.8$, 2.3, 3.4, 4.0, 4.7, 5.4, 6.2, 6.8, 7.6, 8.9, and 10.4. The axes of the simulation are set up in the same manner as the test-particle simulations and the shock is initiated by reflecting the injected plasma off an infinitely conducting wall.

3.6.1 Determining the reflection cutoff

Figure 3.7(a) is a histogram of t_r for ions which are reflected either at the shock or in the downstream region, for the simulation with $M_A \sim 3.4$. We observe two ion populations: those with $0.5\Omega_{ci}^{-1} \lesssim t_r \lesssim 1.0\Omega_{ci}^{-1}$ are immediately reflected by the shock, and those with $t_r \gtrsim 1.0\Omega_{ci}^{-1}$ are "reflected" from downstream of the overshoot due to their downstream gyromotion. Panels (b), (c), (d), and (e) represent the initial phase spaces for ions with $t_r < t^*$ (red) and $t_r > t^*$ (black), with $\Omega_{ci}t^* = 0.6$, 1.0, 1.4, and 1.8, respectively.

We also observe two histogram peaks near $t_r \approx 1.4\Omega_{ci}^{-1}$ and $\approx 2.8\Omega_{ci}^{-1}$ which are explained as follows: the electrostatic potential decelerates the directly transmitted ions nonlinearly in v_x, i.e., $v_{x2} = (v_{x1}^2 - \Delta\varphi_E)^{1/2}$, whereas magnetic deflection decelerates ions linearly in v_y, i.e., $v_{y2} = v_{y1} - u_{y2}$. This would produce an anisotropic distribution of the directly transmitted ions with a

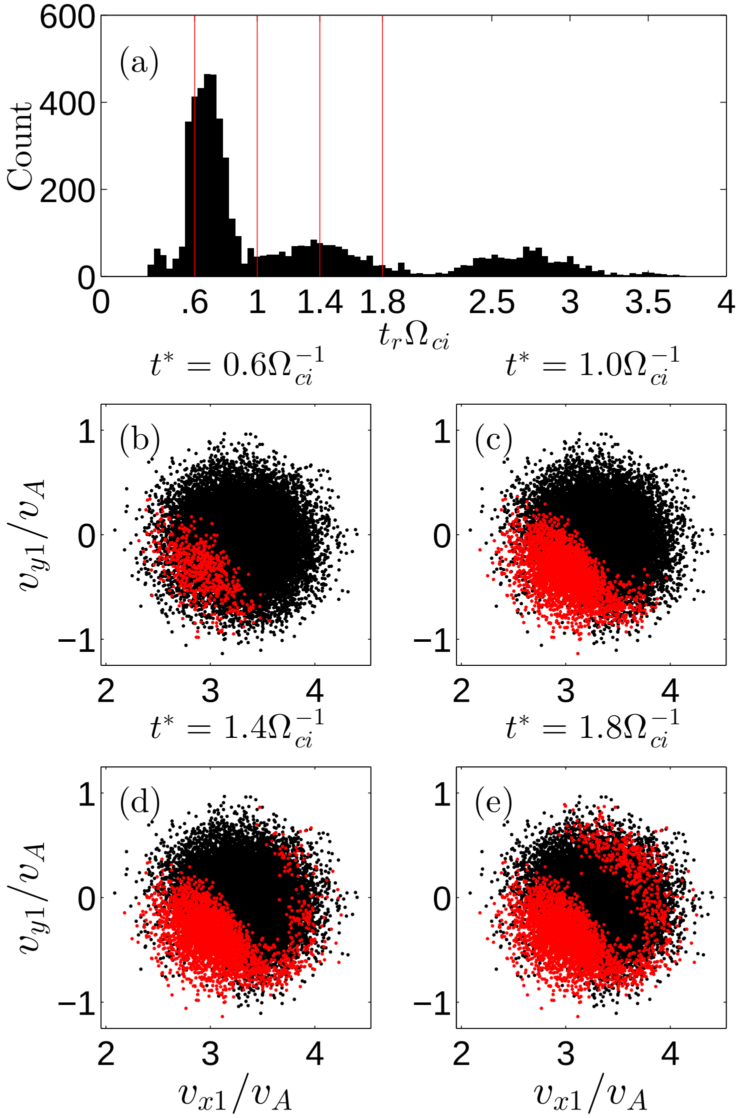

Figure 3.7: (a) Histogram of the reflection time t_r of ions reflected at or downstream from the shock for the hybrid simulation of $M_A \sim 3.4$. Panels (b), (c), (d), and (e) are the initial phase space described by ions reflected at $t_r < t^*$ (red) and $t_r > t^*$ (black) for $t^*\Omega_{ci} = 0.6$, 1.0, 1.4, and 1.8, respectively.

greater spread in v_x than in v_y immediately behind the shock. However, due to the natural gyromotion of the ions through the finite width of the shock, the distribution is rotated $\approx 90^\circ$ in $v_x - v_y$ phase space and as a result the distribution has a larger spread in v_y rather than in v_x. Now as the distribution gyrates about the downstream gyrocenter particles with $v_{\perp 2} \gtrsim u_{x2}$ will reach $v_x < 0$ as part of their downstream gyromotion and so are tallied in the histogram count. However, since the distribution has a greater spread in v_y, more particles are tallied when the distribution gyrates through another $\approx 90^\circ$ and $\approx 270^\circ$, therefore producing the two peaks observed. This is consistent with the fact that the two peaks differ in time by exactly one-half of the calculated downstream gyroperiod $\approx 2.7\Omega_{ci}^{-1}$ (note that $r_B \approx 2.3$ for this shock).

Panels (b) and (c) show that ions immediately reflected by the shock come from a similar phase space domain to that predicted by the model and the test-particle simulations; that is, a reflection boundary indicated by a line in v_{x1} and v_{y1} space. In comparison, panels (c) and (d) show that the ions reflected downstream originate from a shell region in the initial phase space with $-70^\circ \lesssim \theta_1 \lesssim 100^\circ$ and $v_A \lesssim v_{\perp 1} \lesssim 2\, v_A$; these ions have a source region which is consistent with the returning ions identified previously in the test-particle simulations (Figure 3.5). However, in the present analysis it is not identified which of the ions in this shell region actually do return to the foot and ramp as part of their downstream gyromotion, and so are classified as returning particles.

We can now determine τ empirically as equal to the smallest t^* for which the source region prescribed by $t_r < t^*$ contains only the ions reflected in the ramp. For example, from Figure 3.7 we find $\tau \sim 0.96\ \Omega_{ci}^{-1}$ for the simulation with $M_A \sim 3.4$. This empirical method to determine τ is used to distinguish between reflected and transmitted particles in the hybrid simulations.

3.6.2 Determining the effective potential

Here we examine the work done on ions entering the shock at approximately the incoming flow velocity $\mathbf{u}_1 = (u_{x1}, 0, 0)$ for the simulation case $M_A \sim 2.8$. A sample of 138 ions is identified using the criterion $v_{\perp 1} < 0.02 v_A$ at the upstream release point. Figure 3.8's panels (a), (b), (c), and (d) show how Δv_x, Δv_y, W_{Bx}, and W_{Ex}, respectively, vary as a function of time for each of these 138 ions (black lines). Furthermore, each quantity is averaged over the sample (red lines) and compared to the average over the entire ion distribution of 28,358 particles (dashed green lines). Figure 3.8 shows excellent agreement between the red and dashed green lines, meaning that the quantities averaged the entire distribution agree very well with the averages for the incoming particles very near to the incoming flow velocity. This result supports the model assumptions in Section 3, where we approximate the downstream fluid velocity as the downstream velocity of particles entering at the incoming flow velocity. Furthermore, Figure 3.8 shows that the average deceleration of these ions decreases almost linearly with time, supporting the use of linear dependencies in our model. Panel (a) compares the normal velocity shift predicted for deceleration by the electrostatic potential (blue line). Clearly the electrostatic result underpredicts the actual deceleration of the ion distribution, demonstrating that the contribution of magnetic deflection to the deceleration must also be considered.

We now investigate how the effective potential varies as a function of M_A. We measure $\Delta\phi_E$ directly from the hybrid simulations as the electrostatic potential averaged over the total simulation run. The magnetic deflection contribution (3.38) is calculated by taking r_B as the time averaged maximum magnetic enhancement ratio $\langle B_o(t)/B_1\rangle$, r_v as the time averaged ratio of the downstream to upstream fluid speed, and T_2 as the average transmission time estimated by examining the phase space evolution of the ion distribution from analyses of Figure 3.7. Time averaging is needed because for $M_A \gtrsim 4$ the shock undergoes shock reformation and does not have a time stationary profile [*Lembège and Savoini*, 1992; *Yuan et al.*, 2007, 2008a; *Lembège et al.*, 2009; *Tiu et al.*, 2011].

Figure 3.9 plots the normalized quantities $\Delta\varphi_E$, $-\langle W_{Bx}\rangle/(\frac{1}{2}m_i u_{x1}^2)$, and the prediction (3.34) for $\Delta\varphi$ as a function of M_A. Qualitatively, the simulations predict that $\Delta\varphi_E$ attains a maximum value around $M_A \approx 3$ and then decreases steadily with increasing M_A. We compare this with the analytic theory (3.7) for $\eta_f = 2$ [*Zank et al.*, 1996], plotted as the dashed line, which also predicts the same trend. However, it is unclear in the hybrid simulations if $\Delta\varphi_E$ reaches zero, as predicted by (3.7), since $\Delta\varphi_E$ appears to saturate at a value of ≈ 0.5. The magnetic deflection term is found to be proportional to M_A, reaching values that are comparable to $\Delta\varphi_E$ at the maximum $M_A \sim 10.3$. This demonstrates the increasing importance of magnetic deflection to the ion reflection process as M_A increases. In addition, we plot the predicted potential (3.41) for the case where the normal kinetic energy is exactly conserved. Figure 3.9 shows that the simulation results for $\Delta\varphi$ closely match the prediction (3.41). This suggests that the magnetic deflection contribution can be simply estimated by subtracting $\Delta\varphi_E$ from (3.41). More importantly, the approximate conservation of the particle's kinetic energy in the normal direction on average suggests that,

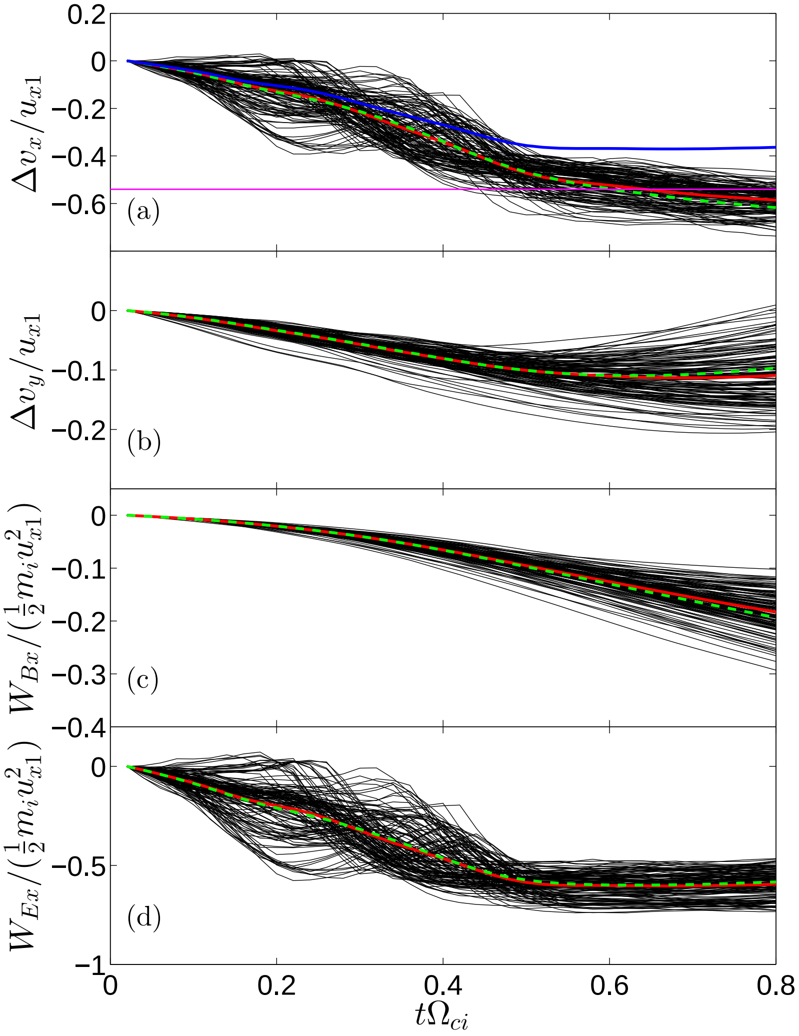

Figure 3.8: For the hybrid simulation $M_A \sim 2.8$, a line series plot of (a) $\Delta v_x/v_A$, (b) $\Delta v_y/v_A$, (c) $W_{Bx}/(\frac{1}{2}m_i u_{x1}^2)$, and (d) $W_{Ex}/(\frac{1}{2}m_i u_{x1}^2)$, as functions of time for 138 particles entering the shock at approximately the upstream flow speed ($v_{\perp 1} < 0.02 v_A$). In each panel, the solid red line plots the quantity averaged over these 138 ions whereas the dashed green line plots the quantity averaged over the entire ion distribution of 28,358 particles. Panel (a) also plots the average deceleration of the ion distribution considering only the work done by the electrostatic potential (blue line) and the normal fluid velocity shift $u_{x2}/u_{x1} - 1 \approx -0.54$ (pink line).

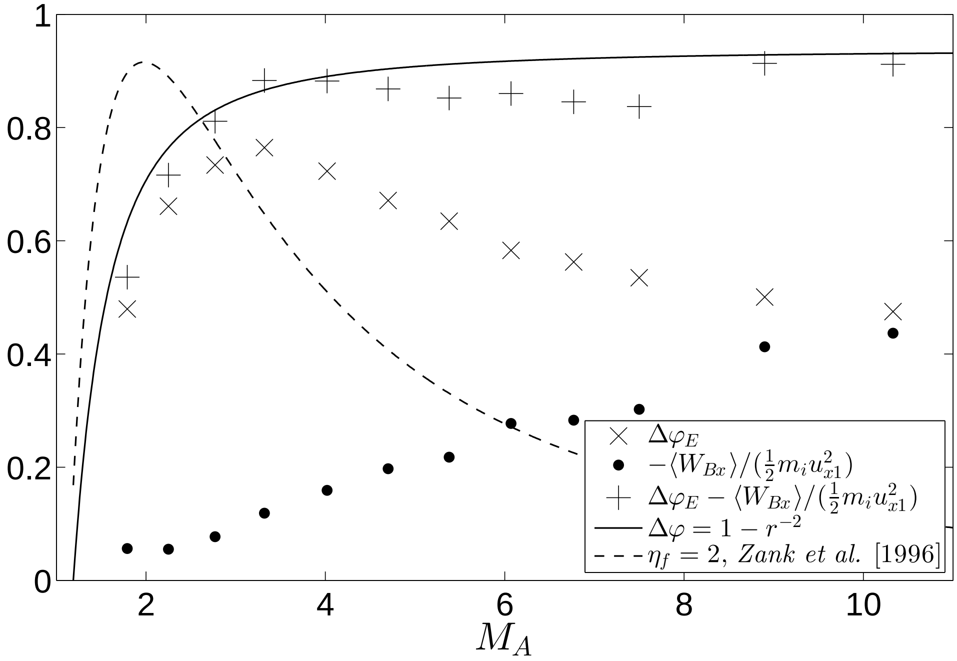

Figure 3.9: In normalized units, the electrostatic potential $\Delta\phi_E$, work done $-\langle W_{Bx}\rangle$ by magnetic deflection, and their sum $\Delta\phi = \Delta\phi_E - \langle W_{Bx}\rangle$ measured from the hybrid simulations as a function of M_A. These are compared with the prediction (3.41) for normal energy conservation, using the R-H compression ratio r, and the prediction (3.10) for $\Delta\phi_E$ with $\eta_f = 2$.

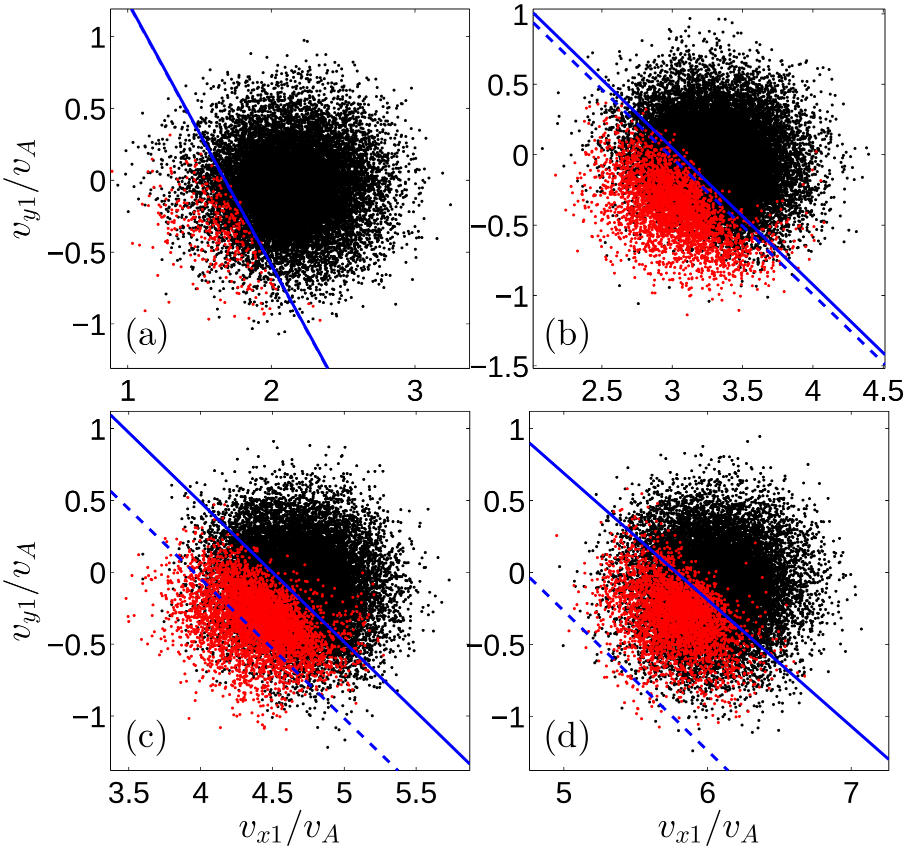

Figure 3.10: Scatter plots of the initial phase space of reflected versus transmitted ions for (a) $M_A \sim 2.3$, (b) $M_A \sim 3.4$, (c) $M_A \sim 4.7$, and (d) $M_A \sim 6.2$. The blue lines show the theoretical prediction (3.56) using $\Delta\phi_E$ (dashed) and $\Delta\phi$ (solid).

at least in the shock layer, the plasma is heated primarily in the $\pm y$ directions and not parallel to $\mathbf{B}$ (in the x-z plane but very close to the z direction) or in the normal direction.

3.6.3 Comparisons between the new model and the reflection cutoff

The phase space distributions of reflected (red) versus transmitted and returning (black) particles are compared in Figure 3.10 for (a) $M_A \sim 2.3$, (b) $M_A \sim 3.4$, (c) $M_A \sim 4.7$, and (d) $M_A \sim 6.2$. Clearly, the hybrid simulations predict the same anticlockwise rotation in the reflection cutoff, even at

$M_A \sim 2.3$, predicted by (3.56). Furthermore, the rotation appears to saturate at a constant angle as M_A increases, since the same slope is observed in the cutoff in panels (b), (c), and (d).

The theoretical cutoff (3.56) depends on v_c and τ which determine the location and rotation of the cutoff, respectively. In Figure 3.10 we plot (3.56) by calculating τ as outlined in Section 5.2 but calculate v_c in two ways: using first the electrostatic potential $\Delta\phi_E$ (dashed blue line) and second the total effective potential $\Delta\phi$ (solid blue line). The electrostatic prediction agrees very well with the simulations in panels (a) and (b), consistent in both the rotation and the location in phase space. However, in panels (c) and (d) the electrostatic prediction, despite having the correct rotation, lies mostly left of the ion distribution and fails to account for the observed separatrix between reflected and transmitted particles. However, the total effective potential leads to extremely good agreement between the theoretical cutoff and the hybrid results for all M_A considered. It is also clear from Figure 3.10 that the contribution from magnetic deflection grows with M_A, as also suggested by the increase in $-\langle W_{Bx}\rangle/(\frac{1}{2}m_i u_{x1}^2)$ with M_A in Figure 3.9.

3.6.4 The reflection efficiency

We can also predict the reflection efficiencies. Figure 3.11 predicts α_E and α_T as functions of M_A from $\Delta\varphi_E$ in (3.12) and $\Delta\varphi$ in (3.58), respectively, using the hybrid simulation results. We also calculate the reflection efficiency directly from the hybrid simulations, plotting the temporal average $\langle\alpha\rangle$ and its minimum and maximum values as error bars, in Figure 3.11 as a function of M_A. Overall α_E shows the opposite behavior to $\langle\alpha\rangle$: α_E reaches a maximum of $\sim 40\%$ at $M_A \sim 3$ but then steadily decreases to zero with M_A whereas $\langle\alpha\rangle$ increases steadily with M_A to an average value of $\approx 19\%$ and a maximum value of $\approx 70\%$ at $M_A \sim 10.3$. Our values of $\langle\alpha\rangle$ are consistent with previous calculations of $\langle\alpha\rangle \approx 10-30\%$ reported in other hybrid simulations [*Leroy et al.*, 1982; *Quest*, 1986; *Lembège and Savoini*, 1992]. *Leroy* [1983] also noted this anti-correlation between $\langle\alpha\rangle$ and α_E as measured in his 1-D hybrid simulations for large M_A, and attributed this difference to the growing importance of magnetic effects in the ion dynamics as a function of M_A.

We propose that this discrepancy between $\langle\alpha\rangle$ and α_E is due to neglecting the contribution (3.39) of magnetic deflection to the total effective potential. Now including magnetic deflection, the predicted reflection efficiency α_T reaches larger but comparable values $\sim 20-30\%$ to $\langle\alpha\rangle \sim 10-20\%$ at the maximum

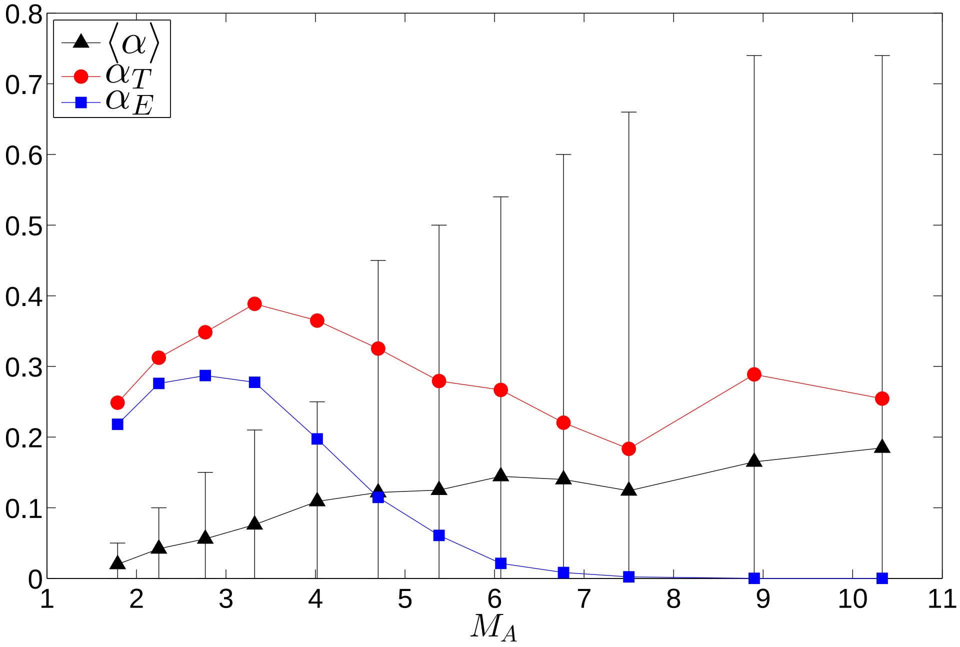

Figure 3.11: Scatter plot of the time-averaged reflection efficiency $\langle\alpha\rangle$ calculated from the hybrid simulations, together with its maximum and minimum values shown as errorbars. This is compared with the electrostatic prediction α_E from (3.12) and the prediction using the effective potential α_T from (3.58).

Mach numbers, although having a nominal discrepancy of $\alpha_T - \langle\alpha\rangle \sim 20\%$ for $M_A \lesssim 5$. This is a major improvement over α_E which predicts that no ions will be reflected at all at high-Mach numbers. Put another way, the time-averaged reflection efficiencies from hybrid simulations are consistent within the error bars with the predictions of our new analytic model, given by (3.58).

A possible explanation as to why $\alpha_T > \langle\alpha\rangle$ is because in Figure 3.10 not all of the transmitted ions lie to the right of the reflection cutoff, i.e., there are some transmitted ions which also occupy the same source region as the reflected ions. This is most likely due to temporal variations in $\Delta\phi$ when $\Delta\phi_E$ is weakened or similarly when L or r_B is small so that magnetic deflection is weak. These temporal variations will cause the reflection cutoff to drift to the left causing the transmitted ions to overlap in initial phase space with ions reflected at other times. Therefore, since α_T is calculated assuming a reflection cutoff which is independent of time, (3.58) would overpredict the actual value of the reflection efficiency.

3.6.5 Source of the rotation

As demonstrated in the test-particle simulations, the rotation of the reflection cutoff can be attributed to particle gyromotion through the finite width of the magnetic foot and ramp. However, is the foot or the ramp the primary source of the rotation in the hybrid results? Figure 3.12 shows how the shock's magnetic profile evolves with M_A and time. The magnetic profile is plotted at times when $B_o(t)$ is maximized and minimized as solid and dashed lines, respectively. For the simulations with $M_A = 1.8$ and 2.3 the two profiles are very similar in magnitude and shape, showing a shock that is stationary in time. However, for $M_A \gtrsim 3$ the profiles for maximum $B_o(t)$ exhibit clear foot and overshoot structures while the profiles for minimal $B_o(t)$ closely resemble laminar profiles.

This shows that for $M_A \gtrsim 3$ the shock profile is significantly variable in time, so that the features of the foot and ramp may disappear and reappear, varying the overall width of the shock and therefore the rotation in the reflection cutoff. Importantly, Figure 3.12 shows that the ramp thickness is approximately constant with M_A, with $L_r \approx 0.2\lambda_i$, consistent with spacecraft measurements [*Mazelle et al.*, 2010; *Hobara et al.*, 2010]. This is compared to the foot which increases up to $L_f \approx 1.5\lambda_i$. Since $L_f > L_r$, we conclude that the magnetic foot is primarily responsible for the rotation of the reflection cutoff in the hybrid simulations.

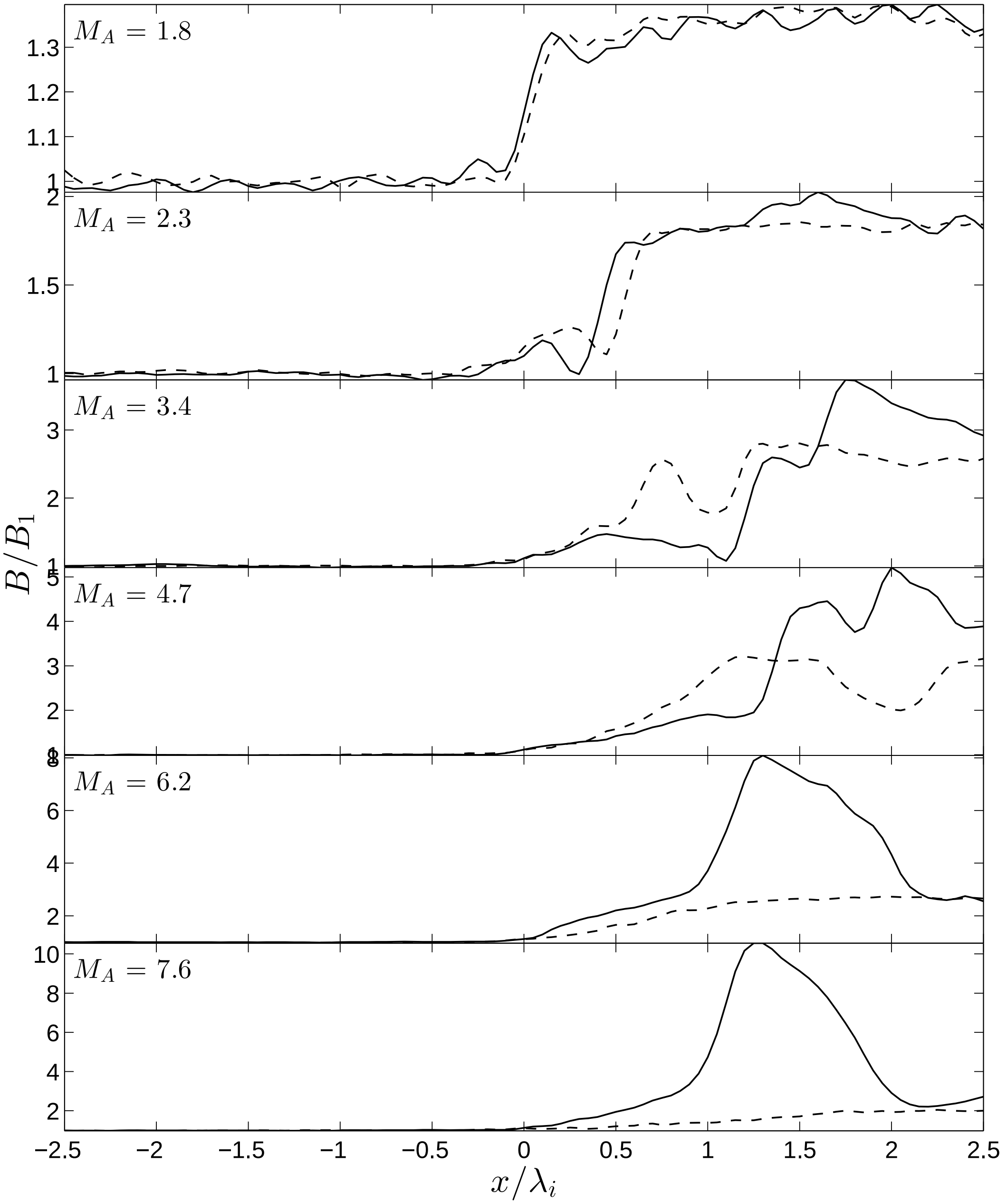

Figure 3.12: Spatial profiles of B/B_1 when B_o is at a maximum (solid line) and at a minimum (dash line) for different M_A, showing the onset of reformation for $M_A \approx 3$.

3.7 Conclusions

In this Chapter we demonstrated that magnetic field effects are vital for the reflection of thermal ions at and upstream of the shock overshoot. Specifically, we developed an accurate new analytic model for a magnetic deflection mechanism which enhances the electrostatic reflection process and is dominant for $M_A \gtrsim 3$. The magnetic deflection mechanism arises because in the shock layer the time-integrated $\mathbf{v} \times \mathbf{B}$ force in the y-direction is no longer balanced by the convection electric field $\mathbf{E}$, thus inducing a net deceleration of the ion distribution in the negative y direction. This is then translated into a deceleration in the negative x direction via the $\mathbf{v} \times \mathbf{B}$ force. Our model predicts that the average work done $\langle W_{Bx} \rangle$ by magnetic deflection on the ion distribution is determined by the magnetic enhancement ratio r_B in the shock layer, the R-H compression ratio r, and the total width L of the shock. Therefore we proposed a new effective potential (3.34) which is the sum of the electrostatic potential $\Delta\phi_E$ and work done by magnetic deflection $-\langle W_{Bx} \rangle$.

A theoretical reflection cutoff (3.56) was derived and shown to depend on the maximum reflection time τ and the effective cutoff speed v_c, which determine the rotation and location of the reflection cutoff respectively. Equation (3.56) was compared extensively with test-particle and 1-D hybrid simulations. The theoretical model agreed remarkably well with the test-particle simulations, being able to accurately predict which ions will be reflected as a function of L and $\Delta\phi_E$. We also found that in the simple case of a laminar shock profile, the maximum reflection time τ is proportional to L, with a gradient depending on B_2 and v_c. This will allow us to predict the rotation of the reflection cutoff using the parameters L, B_2, and v_c, without empirically determining τ in future analyses.

Furthermore, 1-D hybrid simulations of quasiperpendicular shocks with a wide range of $M_A \sim 1.8 - 10.3$ showed that the electrostatic potential decreases with M_A whereas the work done by magnetic deflection increases with M_A. However, the combination of these processes seems to conserve normal kinetic energy, as indicated by their combined effective potential agreeing extremely well with (3.41) as a function of M_A. This suggests that the thermalization of the ion distribution occurs primarily in the v_y component. Overall, our results show that magnetic deflection must be included in descriptions of the ion reflection process at quasiperpendicular shocks, especially at high-Mach numbers where its contribution to the ion deceleration becomes dominant. Consequently a purely specular reflection model is inadequate in explaining the ion motion across shocks of finite width. Failing to include the magnetic deflection contribution leads to an incorrect reflection cutoff and underpredicts the true reflection efficiency.

Future work includes linking the new understanding of ion reflection developed here with previous work on reflection immediately downstream of the magnetic shock overshoot [e.g. *Gedalin*, 1996]. Extensions of magnetic deflection to nonthermal particles, especially those subject to shock drift acceleration should also be considered. In addition, the contributions to shock thermalization from magnetic deflection needs to be quantified and related to that required by the Rankine-Hugoniot conditions.

Chapter 4

Source Regions, Energization, and Populations of Different Classes of Ion Trajectories at Perpendicular Collisionless Shocks

4.1 Abstract

There exist multiple classes of particles that are reflected at perpendicular shocks but have markedly different trajectories across the shock. We propose a new classification scheme that distinguishes these different classes of reflected particles and calculate their energization, fractions, and source regions in initial phase space using multiple test-particle simulations. We first simulate the same shock parameters and field profiles as *Gedalin* [1996] and *Lever et al.* [2001], recovering and extending their results. We then investigate changes in the particle source regions and energization as functions of the shock thickness, electrostatic potential, and spatial variations in the electromagnetic field profile. We find that multiply reflected ions (MRI), particles reflected multiple times off the shock front, are more strongly energized for thin shocks. Mild energy gains are observed for shocks with an overshoot, whereas the addition of a foot structure dramatically changes the MRI source region. Moreover, we determine that particle energization is primarily by particle drifts along the upstream convective electric field and compare the relative importance of each particle class by calculating their fractional population as functions of the upstream thermal speed. In general we find that particle populations and their energization are difficult to predict in detail since they depend on shock parameters such as the electrostatic potential and the shock thickness which are not a priori predictable. Finally, we develop and test new analytic reflection

conditions for particles that are: (1) initially reflected by the electrostatic potential, complete half a gyro-orbit upstream, and finally escape downstream, and (2) initially transmitted downstream but return to the shock as part of their downstream gyromotion, complete half a gyro-orbit upstream, and finally escape downstream. We find in most cases the first reflection condition agrees extremely well with numerical results, whereas in the latter case we only find good agreement for shocks with a thin ramp.

4.2 Introduction

Particles can travel along markedly different trajectories across a shock layer. These trajectories depend on the detailed spatio-temporal structure of the shock's electromagnetic field and the initial particle velocity. As a result several different (and perhaps overlapping) models are used to describe the reflection and acceleration of ions at collisionless shocks. These include but are not limited to: shock drift acceleration (SDA) [e.g. *Armstrong et al.*, 1985], specular reflection [e.g. *Gosling et al.*, 1982], multiply reflected ions (MRI) [e.g. *Zank et al.*, 1996; *Lee et al.*, 1996], and ions that are initially transmitted but are "reflected" in the downstream region, return upstream, and are then eventually transmitted [e.g. *Gedalin*, 1996]. These classes of reflected and accelerated particles are important for the overall redistribution of energy between the total electromagnetic field energy and the total kinetic and thermal energy of the ion distribution.

We define the shock geometry as follows: the normal flow velocity is in the $+x$ direction, the upstream convective electric field is along the y axis, and the magnetic field vector is in the $x - z$ plane with angle θ_{Bn} between the upstream magnetic field B_1 and normal direction $-\hat{x}$. The Alfvén Mach number is $M_A = u_{x1}/v_A$ where u_{x1} is the incoming flow speed, $v_A = B_1/(\mu_0 n_i m_i)^{1/2}$ is the upstream Alfvén speed, n_i is the upstream ion number density, m_i is the ion mass, and μ_0 is the permeability of free space. For quasiperpendicular shocks ($45° < \theta_{Bn} < 90°$), spatial regions with enhanced magnetic field strength can arise upstream and downstream of the shock ramp due to the local presence of reflected ions [*Livesey et al.*, 1982]; these spatial structures are called the foot and overshoot, respectively. The shock ramp is idealized as a discontinuous jump in the magnetic field strength but typically has an almost linear increase in magnetic field strength. The foot upstream of the ramp is associated with ions reflected by the cross-shock electrostatic potential [*Gosling et al.*, 1982] and magnetic deflection [e.g. Chapter 2]. The overshoot is associated with the gyromotional return of initially reflected ions that now have larger gyrospeed, thereby enlarging the maximum magnetic field near the ramp. The gyrating ions cause additional undershoot-overshoot patterns in B downstream, which disappear as the ions are thermalized and spread out in $\mathbf{x} - \mathbf{v}$ phase space.

Historically, the term “specular reflection” involves ions that are initially reflected by an electrostatic barrier (the cross-shock electrostatic potential $\Delta\phi_E$) in the shock layer. The term “specular” is given because if the ramp thickness is small compared to the ion gyroradius and inertial length $\lambda_i = v_A/\Omega_{ci}$, i.e. $L_r \ll \lambda_i$, then these ions will have the normal component of their incoming velocity reversed and so have a “mirror-like” reflection [*Gosling et al.*, 1982]. After reflection these ions travel upstream for half a gyro-orbit (or possibly multiple orbits) while drifting along the convective electric field, thereby gaining sufficient energy to now cross the electrostatic barrier into the downstream region. Here the distinction between single or multiple orbits describes particles that undergo shock drift acceleration (SDA) versus multiply reflected ion (MRI) acceleration [*Zank et al.*, 1996] (sometimes called “shock surfing”) [*Zank et al.*, 1996; *Lee et al.*, 1996], respectively. In principle both mechanisms involve particle energization by drifting along the upstream convective electric field.

These reflected particles with large $v_\perp$ start their final transmission downstream and develop into a ring distribution, historically with a downstream gyrospeed of twice the incoming flow speed, i.e. $v_\perp \approx 2u_{x1} \sin\theta_{Bn}$ for a quasiperpendicular shock. However, analyses of particle trajectories from 1-D hybrid simulations in Chapter 2, in particular for large M_A shocks, show that ions reflected at the ramp undergo a significant deflection in v_y through the shock and hence the particle trajectory can no longer be described as “specular” but rather a turning motion until the ion reaches $v_x < 0$. Furthermore, this magnetic deflection leads to a significant normal deceleration of the ion distribution at the shock, quantitatively supplementing the electrostatic deceleration by the cross-shock potential. On the other hand, there are ions that are initially transmitted through the shock but are then “reflected” in the downstream region and return upstream via their downstream gyromotion. Presumably they can then undergo either SDA or MRI before being finally transmitted downstream.

Thus there are several models which describe the reflection and/or acceleration of incident ions at quasiperpendicular shocks. However, does reflection necessarily imply energization? Or vice-versa: can a particle be accelerated without being reflected? This Chapter seeks to distinguish between the multiple types of particles at perpendicular shocks that are generally classified as "reflected" in order to definitively determine their energization mechanism and to compare their properties with analytic theory. Note that limiting our discussion to only perpendicular shocks means that no ions escape upstream since all particles will have their guiding centers directed downstream [*Gosling et al.*, 1982].

This Chapter is outlined as follows. Section 1 introduces the simple criteria to classify different ion trajectories across a perpendicular shock, discussing the new classification scheme in the context of *Lever et al.*'s [2001] similar classification scheme. Section 2 develops new analytic predictions for the source regions of certain particle classes, specifically, extending the previous prediction of *Gedalin* [1996] and the "specular" reflection condition found in Chapter 3. In Section 3 we analyze multiple test-particle simulations, investigating the particle source regions and associated energization by the shock. Finally, Section 4 presents and discusses calculations of fractional populations of each class of particle and their relative importance.

4.3 Classifying reflected and transmitted ions

We identify different classes of reflected and transmitted ions by considering the various trajectories that a particle can take across the shock layer. We work in the normal incidence frame (NIF) where the shock is at rest, unless otherwise stated. First we define the ramp region to be between $x = 0$ and $x = L_r$, where L_r is the ramp thickness. A particle's initial velocity is defined to be $\mathbf{v}_1 = (v_{x1}, v_{y1}, v_{z1})$ as it enters the shock front at the leading edge of the foot at $x = -L_f$ at time $t = 0$. We consider thermal and mildly superthermal particles that have $v_{x1} > 0$ at all locations upstream of the shock foot. If a particle is reflected, meaning that it has $v_x < 0$, then let the time of first reflection be $t = t_r$ and the x-position along its 3-D trajectory be $x_r = x(t_r)$. The particle will then turn around, i.e. have $v_x > 0$, along its subsequent trajectory at position $x = x_t$ at a time t_t, where $t_t > t_r$.

We first categorize particles by their initial reflection location: particles reflected before $x_r < L_r$, particles reflected in the overshoot or downstream region $x_r > L_r$, and particles which are never reflected. These groups can then be divided further by considering their subsequent turnaround locations using a similar criterion: particles turnaround in the upstream and foot region $x_t < 0$, particles turnaround in the ramp region $0 < x_t < L_r$, and particles turnaround in the overshoot or downstream region $x_t > L_r$. Therefore we can identify 7 possible trajectories and using the following labelling scheme: Each uppercase letter indicates the region in which the particle is first reflected. These are: S (ramp), D (downstream), and NR (not reflected). Superscripts "u","r", and "d" indicate the particle's turnaround location in either the upstream, ramp, or downstream region, respectively, while "MRI" indicates that the particle is reflected multiple times off the shock front. Table 4.1 lists these 7 possible trajectories and their description across the shock profile in detail. To illustrate the differences in trajectories, Figures 4.1 and 4.2 plot example trajectories of these particle classes in $x - y$ and $x - v_x$ phase space, respectively, where the ramp region is indicated by the two dashed vertical lines.

Lever et al. [2001] classified 3 types of reflected ions in test-particle simulations by recording at each time step from a particle's initial shock encounter until its first reflection: (1) $E_x < v_y B_z$, i.e., "dominating electric force" (2) $E_x > v_y B_z$, i.e., "dominating Lorentz force", or (3) if the particle has crossed from the downstream region into the upstream region. Those particles having a majority count in either of the first two groups were labelled as "Surfing" or "Drifting" ions, respectively, although Drifting and Surfing particles are both associated with shock drift acceleration. Any particles with any counts in the third group were called "Crossing" ions. From *Lever et al.*'s [2001] Figure 3, which shows particle trajectories in $x - y$ space, Surfing/Drifting particles are initially reflected at the ramp and have their turnaround location upstream but Crossing particles are initially transmitted, reflected in the downstream region, and then turn around upstream. Therefore in our classification, Surfing/Drifting particles are S^u particles and Crossing particles are D^u particles.

Gedalin [1996] also investigated ion reflection using an analytic model and test-particle simulations. Specifically, he studied the classes of D^r and D^u ions, investigating how the reflection efficiencies of these particles vary with the cross-shock potential $\Delta\phi_E$ and magnetic enhancement ratio B_2/B_1 where B_2 is the downstream magnetic field strength. He found from test-particle calculations that the reflection efficiencies of D^r and D^u particles are correlated with B_2/B_1 but have little to no dependence on $\Delta\phi_E$.

4.4 Theory

4.4.1 Reflection cutoff for S^u and S^r particles

The reflection cutoff for ions that are initially reflected at the potential ramp (by either electrostatic reflection and/or magnetic deflection) and not transmitted

Table 4.1: Particle classes based on trajectories through the shock layer. Each uppercase letter indicates the region in which the particle is first reflected: S (ramp), D (downstream), and NR (not reflected). Superscripts "u","r", and "d" indicate the particle's turnaround location in either the upstream, ramp, or downstream region, respectively, while "MRI" indicates that the particle is reflected multiple times off the shock front.

Particle label	**Particle trajectory**
NR	The ion is transmitted through the shock and is never reflected.
S^u	The ion is reflected in the shock ramp $0 < x_r < L_r$, it turns around in the upstream region $x_t < 0$, it drifts along the upstream convective electric field and is subsequently transmitted through the shock and not reflected again.
S^r	The ion is reflected once in the ramp $0 < x_r < L_r$ but does not enter the upstream region; instead it turns around within the ramp region $0 < x_t < L_r$, and is not reflected again.
MRI	The ion is reflected multiple times in the upstream and ramp region $x < L_r$.
D^u	The ion is first transmitted through the shock, then reflected downstream beyond the ramp $x_r > L_r$, its turnaround location is in the upstream region $x_t < 0$, and it is eventually transmitted.
D^r	The ion is first transmitted through the shock, then reflected downstream where $x_r > L_r$, its turnaround location is in the ramp region $0 < x_t < L_r$, and it is eventually transmitted.
D^d	The ion is first transmitted through the shock, then reflected in the downstream region at $x_r > L_r$, turns around in the downstream region at $x_t > L_r$, and is transmitted downstream.

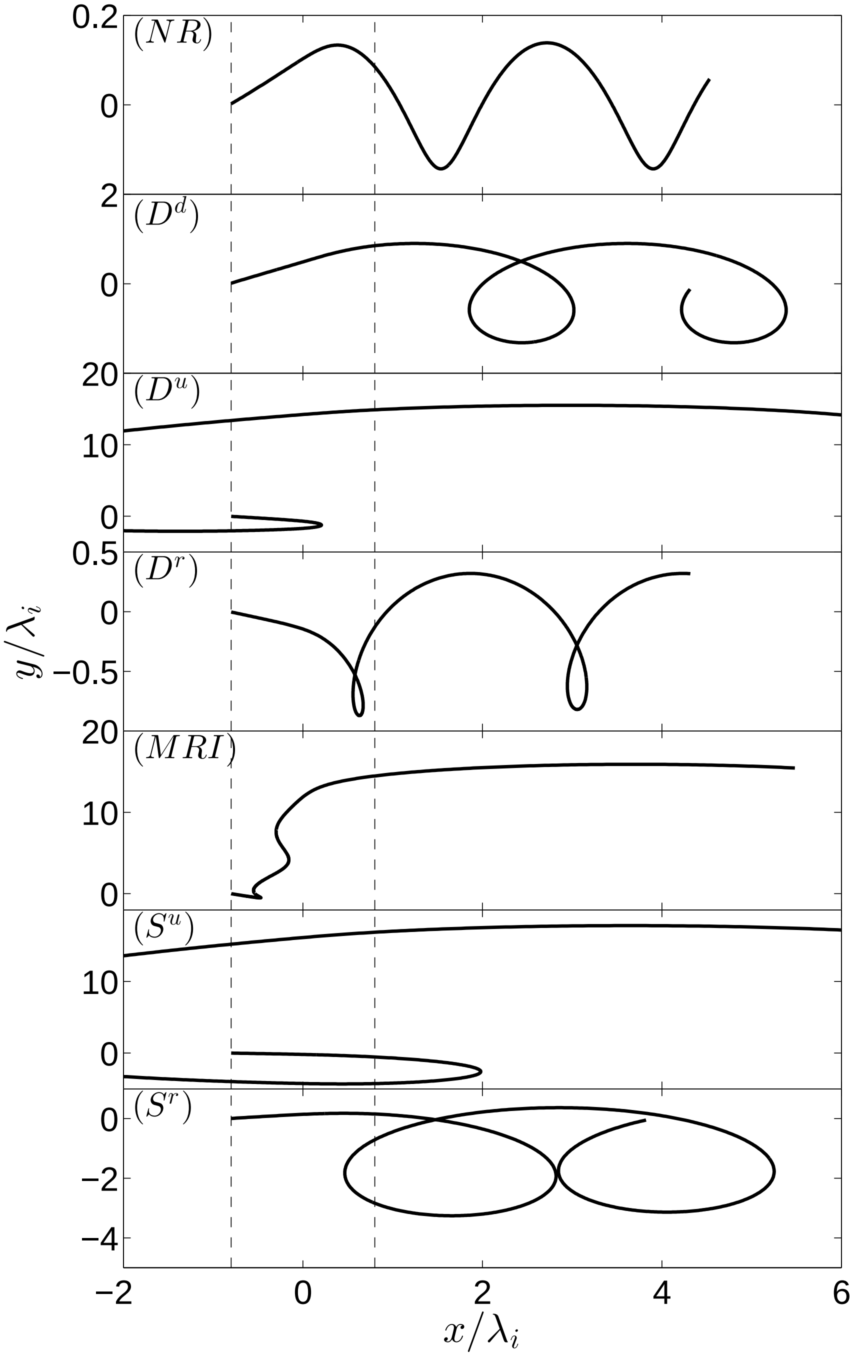

Figure 4.1: Represented in $x-y$ phase space, the different classes of ion trajectories in Table 4.1 where the ramp region is between the dashed vertical lines.

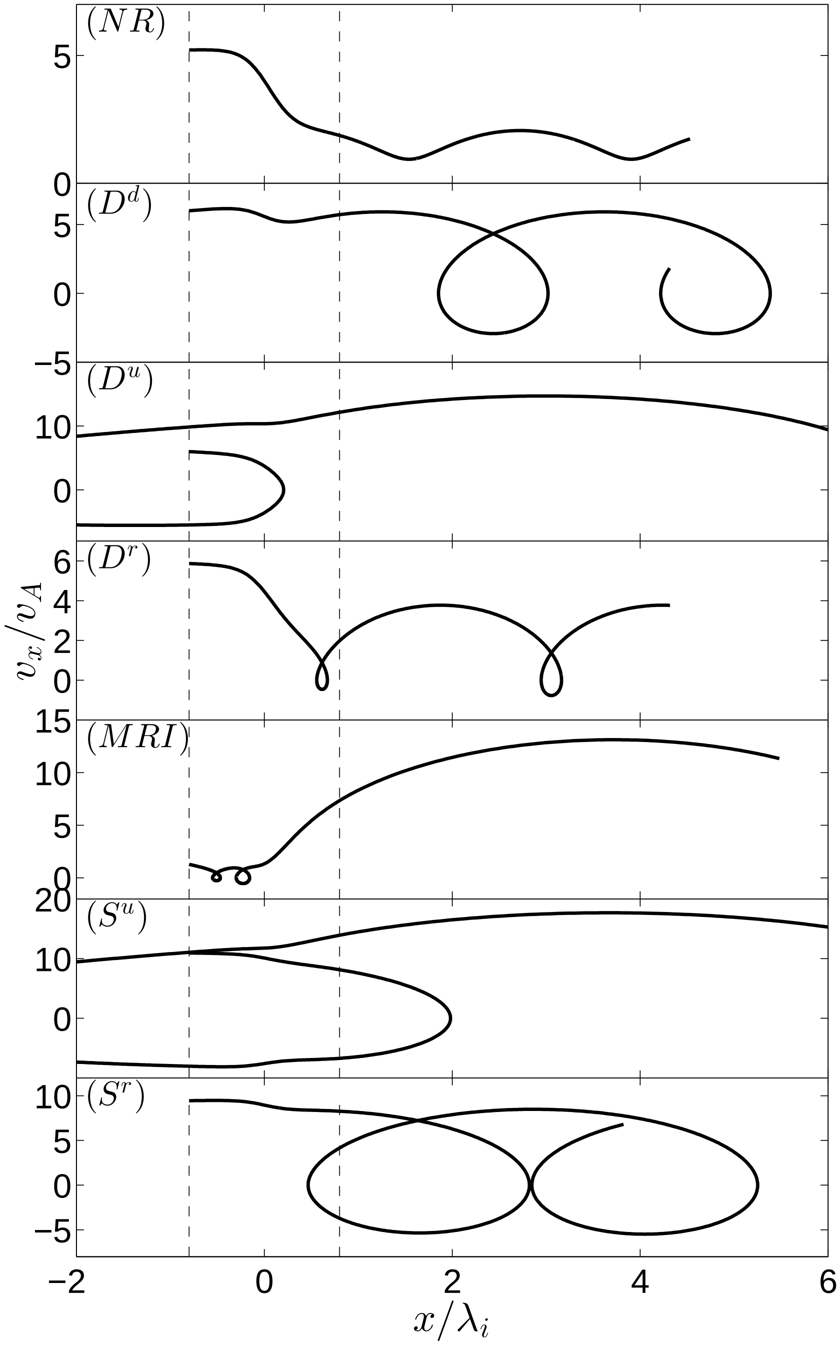

Figure 4.2: Represented in $x - v_x$ phase space, the different classes of ion trajectories in Table 4.1 where the ramp region is between the dashed vertical lines.

directly, i.e. S^u or S^r particles, is derived in Chapter 2:

$$v_{y1} \simeq -\cot(\Omega_{ci}\tau)(v_{x1} - u_{x1}) + \csc(\Omega_{ci}\tau)(v_c - u_{x1}) \tag{4.1}$$

where τ is the maximum reflection time, which determines the rotation of the reflection cutoff in $v_{x1} - v_{y1}$ phase space. We will now refer to (4.1) as the S-separatrix. The effective cutoff speed v_c is defined as

$$v_c = \sqrt{\frac{2e\Delta\phi}{m_i}} \tag{4.2}$$

where $\Delta\phi$ is the effective potential that equals the sum of the electrostatic potential $\Delta\phi_E$ and the work $-\langle W_{Bx}\rangle$ done by magnetic deflection, i.e.,

$$e\Delta\phi = e\Delta\phi_E - \langle W_{Bx}\rangle, \tag{4.3}$$

where $\langle W_{Bx}\rangle$ is estimated from (3.39) in Chapter 3 to be

$$\frac{\langle W_{Bx}\rangle}{\frac{1}{2}m_i u_{x1}^2} \simeq -\frac{2l^2}{3M_A^2}\left[\frac{2B_o^2 + B_o^2 B_2 + B_o - 4B_o B_2}{(B_2+1)^2}\right]. \tag{4.4}$$

Here B_o is the magnetic overshoot strength, B_2 is the downstream magnetic field strength, and $l = L/\lambda_i$ is the normalized shock thickness. In Chapter 3 an analytic prediction for the maximum reflection time was derived,

$$\tau = 2\frac{L}{v_c^E} \tag{4.5}$$

assuming a shock with an electrostatic potential but with a constant background magnetic field, where $v_c^E = 2e\Delta\phi_E/m_i$ is the electrostatic cutoff speed.

In general, the fractional population of a particle class Σ can be calculated as follows

$$\alpha_\Sigma = \frac{\displaystyle\int_0^\infty \int_{-\pi}^{\pi} \delta_\Sigma(v_{\perp 1}, \theta_1) v_{\perp 1} f(v_{\perp 1}, \theta_1)\; dv_{\perp 1} d\theta_1}{\displaystyle\int_0^\infty \int_{-\pi}^{\pi} v_{\perp 1} f(v_{\perp 1}, \theta_1)\; dv_{\perp 1} d\theta_1} \tag{4.6}$$

where

$$f(v_{\perp 1}, \theta_1) = \frac{1}{\pi v_{th1}^2}\exp\left(-v_{\perp 1}^2/v_{th1}^2\right) \tag{4.7}$$

is the 2-D Maxwellian distribution in polar coordinates, $v_{th1} \equiv (k_B T_{i1}/m_i)^{1/2}$ is the upstream ion thermal speed, T_{i1} is the upstream ion temperature, and δ_Σ

is the Dirac delta function which equals unity for all elements of phase space $(v_{\perp 1}, \theta_1)$ that are identified as a Σ particle. The fractional population for S^u particles, α_{S^u}, was derived in Chapter 3,

$$\alpha_{S^u} = \frac{1}{2}\mathrm{erfc}\left(\frac{u_{x1} - v_c}{\sqrt{2}v_{th1}}\right) \tag{4.8}$$

where $\mathrm{erfc}(x) = 1 - 2/\pi^{1/2}\int_0^x e^{-t^2}dt = 1 - \mathrm{erf}(x)$ is the complementary error function.

The 1-D hybrid simulation results in Chapter 3 show that the downstream ion fluid velocity is comparable to the downstream $\mathbf{E} \times \mathbf{B}$ drift velocity immediately behind the shock ramp, independent of the size of the electrostatic potential. This implies that the total effective potential can also be written as the change in the normal kinetic energy of the plasma stipulated by the Rankine-Hugoniot jump conditions; i.e.

$$\Delta\varphi = \frac{e\Delta\phi}{\frac{1}{2}m_i u_{x1}^2} = 1 - \frac{1}{r^2}, \tag{4.9}$$

where r is the Rankine-Hugoniot compression ratio.

4.4.2 Reflection cutoff for D^u and D^r particles

Gedalin [1996] showed that particles reflected downstream of the ramp will return to the ramp as part of their downstream gyromotion, i.e. be D^u or D^r particles, if they satisfy the condition

$$\begin{aligned} &v_{\perp 2}\sin\theta_2 - \left(v_{\perp 2}^2 - w_{x2}^2\right)^{1/2} \\ &+ w_{x2}\left[\pi + \theta_2 + \cos^{-1}\left(\frac{w_{x2}}{v_{\perp 2}}\right)\right] < 0. \end{aligned} \tag{4.10}$$

Here $\mathbf{w}_2 = (w_{x2}, w_{y2})$ is the downstream gyrocenter and

$$v_{\perp 2}^2 = (v_{x2} - w_{x2})^2 + (v_{y2} - w_{y2})^2 \tag{4.11}$$

$$\theta_2 = \tan^{-1}\left(\frac{v_{x2} - w_{x2}}{v_{y2} - w_{y2}}\right), \tag{4.12}$$

are the downstream gyrospeed and gyrophase of transmitted ions, respectively. For convenience, (4.10) will be referred to as the D-separatrix.

To calculate (4.10), we require an analytic prediction for the velocity of transmitted particles $\mathbf{v}_2 = (v_{x2}, v_{y2})$ at the trailing edge of the ramp. *Gedalin*

[1996] followed the thin ramp approximation by *Leroy* [1983] to write

$$v_{x2} = \left(v_{x1}^2 - \Delta\varphi_E\right)^{1/2} \tag{4.13}$$

$$v_{y2} = v_{y1} - u_{y2} \tag{4.14}$$

where $\Delta\varphi_E = 2e\Delta\phi_E/m_i$ is the normalized electrostatic potential, u_{y2} is the velocity shift in v_y due to magnetic deflection and v_{x2} takes the electrostatic deceleration into account. *Gedalin* [1996] predicted the velocity shift by magnetic deflection to be

$$u_{y2} = L_r(B_2 - 2B_1)/2 \tag{4.15}$$

whereas in Chapter 2 we found

$$u_{y2} = \frac{L_r(B_2-1)^2}{3(B_2+1)}, \tag{4.16}$$

where L_r is the ramp thickness. By substituting (4.11)-(4.12) into (4.10) one can predict the source region of D^u and D^r ions in initial phase space. However, (4.13) and (4.14) neglect the normal deceleration by magnetic deflection and the rotation of the distribution by its natural gyromotion through the finite width of the foot and ramp. Accordingly, following the analysis in Chapter 2, we modify (4.13) and (4.14) to

$$v_{x2} = \left(v_{xg}^2 - \Delta\varphi\right)^{1/2} \tag{4.17}$$

$$v_{y2} = v_{yg} - u_{y2} \tag{4.18}$$

where $\Delta\varphi = 2e\Delta\phi/m_i$ is the normalized total potential and

$$v_{xg} = u_{x1} + v_{\perp 1}\cos(\Omega_{ci}\tau - \theta_1) \tag{4.19}$$

$$v_{yg} = -v_{\perp 1}\sin(\Omega_{ci}\tau - \theta_1). \tag{4.20}$$

That is, we replace the initial velocity components v_{x1} by v_{xg} and v_{y1} by v_{yg}, respectively, as so to include the deceleration by magnetic deflection and an anticlockwise rotation by an angle $\Omega_{ci}\tau$ due to the gyromotion through the foot and ramp. The prediction (4.10) with (4.11), (4.12), and (4.17)-(4.20) is then the revised prediction for the D-separatrix in $v_{x1} - v_{y1}$ phase space.

4.4.3 Particle energization

In the normal incidence frame an ion in its upstream gyromotion has

$$v_{xg}(t) = u_{x1} + v_{\perp 1}\cos(\Omega_{ci}t - \theta_1) \tag{4.21}$$

$$v_{yg}(t) = -v_{\perp 1}\sin(\Omega_{ci}t - \theta_1), \tag{4.22}$$

having a total perpendicular energy of

$$\begin{aligned} U(t) &= \frac{1}{2}m_i\left[v_{xg}^2(t)+v_{yg}^2(t)\right] && (4.23)\\ &= \frac{1}{2}m_i\big[u_{x1}^2+2u_{x1}v_{\perp 1}\cos(\Omega_{ci}t-\theta_1)+ \\ &\qquad v_{\perp 1}^2\cos^2(\Omega_{ci}t-\theta_1)+v_{\perp 1}^2\sin^2(\Omega_{ci}t-\theta_1)\big] && (4.24)\\ &= \frac{1}{2}m_i\left[u_{x1}^2+2u_{x1}v_{\perp 1}\cos(\Omega_{ci}t-\theta_1)+v_{\perp 1}^2\right]. && (4.25)\end{aligned}$$

using (4.19)-(4.20). Its perpendicular energy thus varies periodically about the average energy

$$U_1=\frac{1}{2}m_iu_{x1}^2+\frac{1}{2}m_iv_{\perp 1}^2, \tag{4.26}$$

consisting of the kinetic energy corresponding to its upstream convective motion and its perpendicular thermal energy. Likewise its average downstream perpendicular energy is

$$U_2=\frac{1}{2}m_iu_{x2}^2+\frac{1}{2}m_iv_{\perp 2}^2. \tag{4.27}$$

If the downstream convective speed is $u_{x2}=u_{x1}/r$, where r is the Rankine-Hugoniot compression ratio, then the change in a particle's total perpendicular energy across the shock is

$$\begin{aligned} U_2-U_1 &= \frac{1}{2}m_i\left(u_{x2}^2-u_{x1}^2\right)+\frac{1}{2}m_i\left(v_{\perp 2}^2-v_{\perp 1}^2\right) && (4.28)\\ &= \frac{1}{2}m_iu_{x1}^2\left(\frac{1}{r^2}-1\right)+\frac{1}{2}m_i\left(v_{\perp 2}^2-v_{\perp 1}^2\right). && (4.29)\end{aligned}$$

We define the energization factor

$$\varepsilon=\frac{U_2}{U_1}-1 \tag{4.30}$$

as the fractional increase in an ion's average energy, so ions that are energized by the shock have $\varepsilon>0$. If (4.9) is satisfied then from (4.29) the condition $\varepsilon>0$ corresponds to

$$v_{\perp 2}^2>v_{\perp 1}^2+v_c^2 \tag{4.31}$$

since $v_c^2=u_{x1}^2(1-r^{-2})=2e\Delta\phi/m_i$ from (4.9).

Equation (4.31) predicts that all particles that are energized have $v_{\perp 2}>v_{\perp 1}$, but that not all particles with $v_{\perp 2}>v_{\perp 1}$ are energized, i.e., $v_{\perp 2}>v_{\perp 1}$

is a necessary but not sufficient condition for energization. This is because all particles will lose an energy of at least $-e\Delta\phi$ through the shock before considering other acceleration or heating effects.

On the other hand, taking into account the cross-shock potential and drift along the convection electric field, the energization factor ε can also be expressed independently of (4.30) as

$$\varepsilon = U_1^{-1}\left(E_y\Delta y_{gc} - e\Delta\phi\right). \tag{4.32}$$

Here $E_y = u_{x1}B_1$ is the convective electric field and $\Delta y_{gc} = y_{gc2} - y_{gc1}$ is the particle's displacement of its guiding center in y, where y_{gc1} and y_{gc2} are the y-positions of the upstream and downstream guiding centers, respectively.

4.5 Test-particle simulations

4.5.1 Confirmation and extension of *Gedalin*'s [1996] test-particle simulations

Gedalin [1996] used a supercritical shock profile with foot and overshoot regions for the magnetic field, as shown in Figure 4.3(a), and the initial distribution is injected at $x_1 = -4.275\lambda_i$. We perform a test-particle simulation with the same parameters and field profiles as *Gedalin* [1996]: $M_A = 7.5$, $l_r = 0.225$, $B_2/B_1 = 3.2$, and $\Delta\varphi_E = 0.5$ where $l_r = L_r/\lambda_i$ is the normalized ramp thickness. However, we examine a larger area of initial phase space $v_{x1} - v_{y1}$ in our simulation, specifically investigating the range $\max(v_{\perp 1}) = u_{x1}$ whereas *Gedalin*'s [1996] range was $\max(v_{\perp 1}) = 0.2u_{x1}$.

Figure 4.4 displays our simulation results with *Gedalin*'s [1996] shock parameters. Panel (a) plots the source region for each particle class in initial phase space. We find most of the phase space domain corresponds to particles reflected downstream of the ramp (D^u and D^d): approximately 50% of the initial domain corresponds to D^d particles. A small region of NR particles exists within the domain of the D^d particles. MRI particles are found to be a subset of the S^u particles, both covering significant domains. Since the ramp region is relatively thin ($l_r = 0.225$) no S^r or D^r ions are found in the simulation. By way of contrast, *Gedalin*'s [1996] domain of interest lies within the red dashed circle, meaning that only D^d and D^u particles were detected in his test-particle simulation. This is because the electrostatic cutoff speed is much smaller than the incoming flow speed ($v_c^E \ll u_{x1}$) and therefore lies outside his

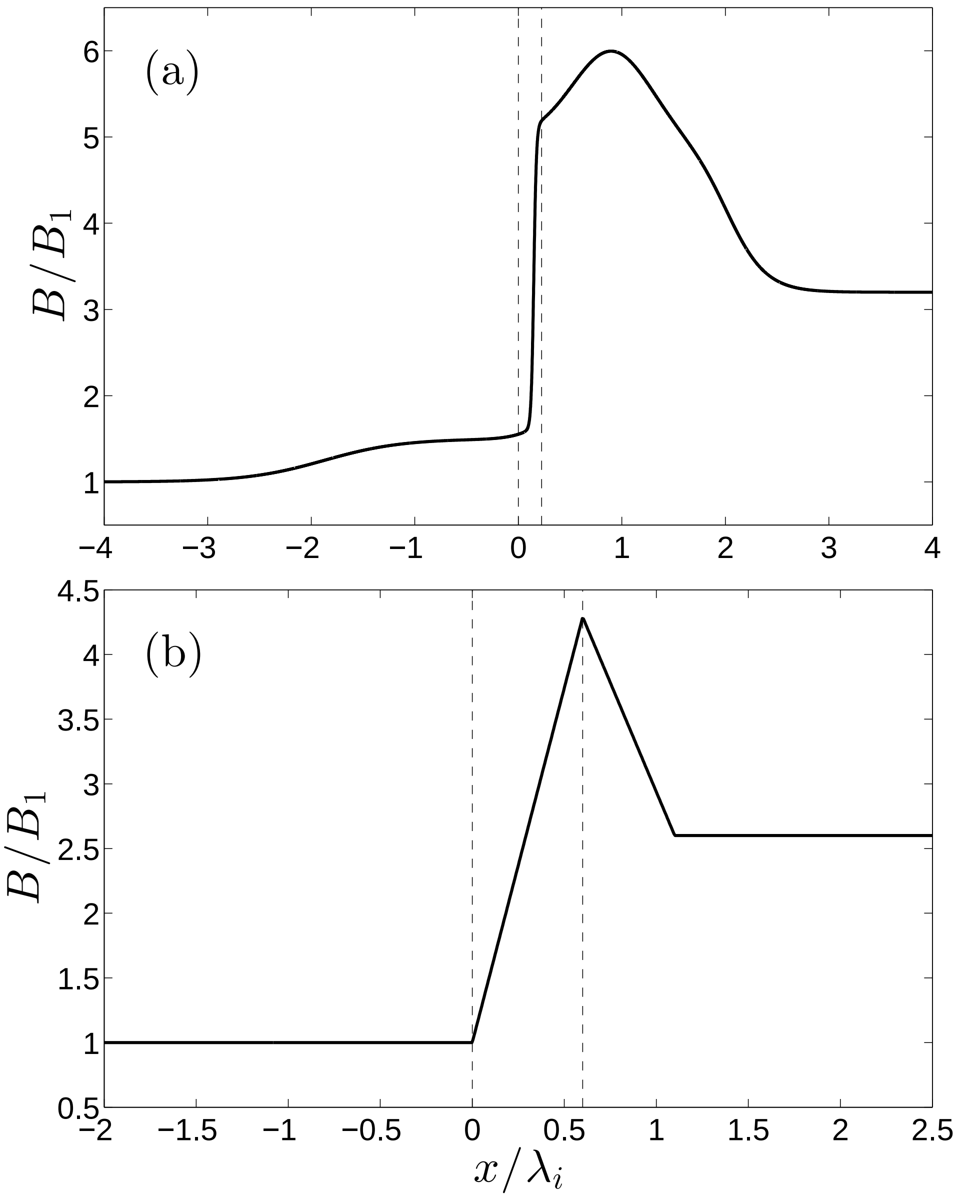

Figure 4.3: The magnetic field profile used in (a) *Gedalin*'s [1996] test-particle simulation, and (b) *Lever et al.*'s [2001] test-particle simulation. Here the region between the dashed vertical lines is the ramp region used to classify the different ion trajectories in Table 4.1.

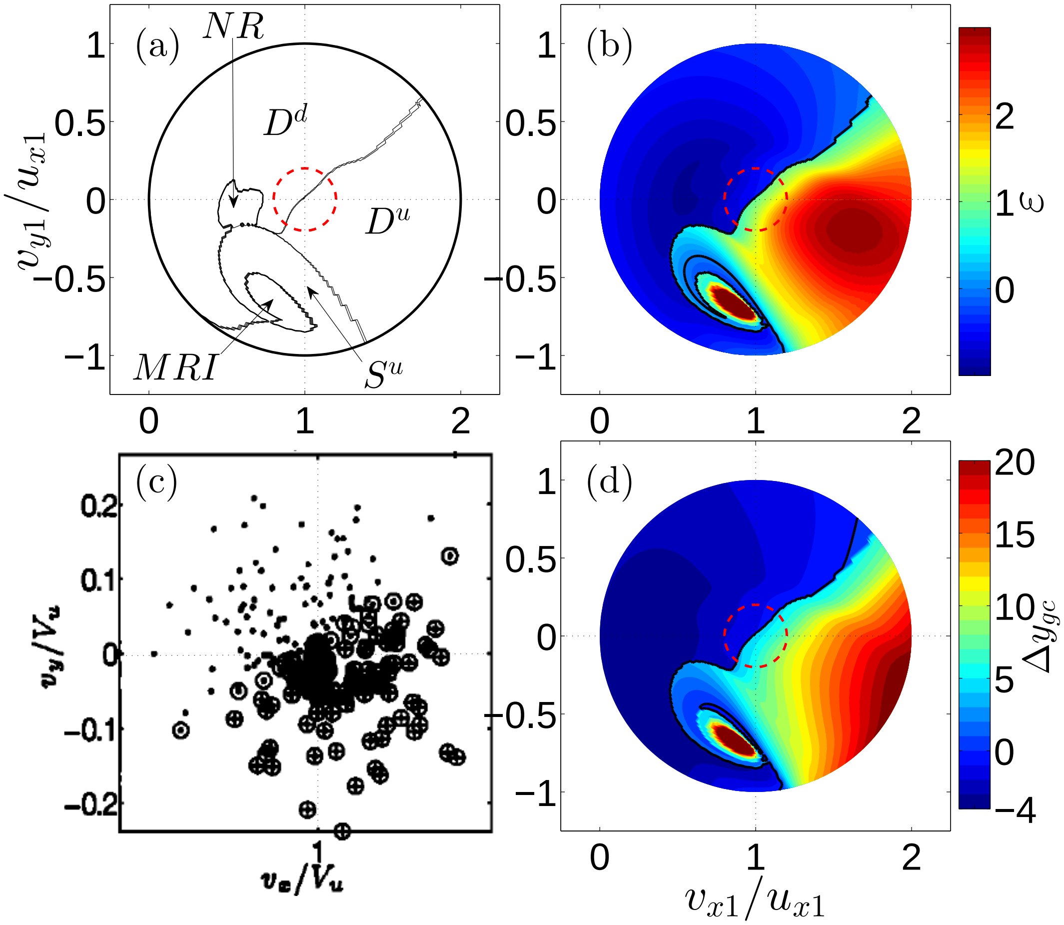

Figure 4.4: For the test-particle simulation using *Gedalin*'s [1996] shock parameters $M_A = 7.5$, $l_r = 0.225$, $B_2/B_1 = 3.2$, and $\Delta\varphi_E = 0.5$: plots in $v_{x1} - v_{y1}$ phase space of (a) the particle source regions, (b) the energization profile and $\varepsilon = 0$ contour, (c) *Gedalin*'s [1996] original simulation results identifying D^u particles (+) and all other particles ($\cdot$) where open circles mark D^u and D^r particles theoretically predicted by (4.10), and (d) each particle's guiding center displacement in y, Δy_{gc}.

initial phase space range, i.e., $v_c^E < 0.8u_{x1}$. Comparing panel (c) with panel (a) it is clear that we recover *Gedalin*'s [1996] results: we also extend them to a larger domain of phase space and consider the energy gains in panels (c) and (d).

In Figure 4.4(a) the MRI particles have a relatively large initial normal speed close to incoming flow speed, i.e. $v_{x1} \approx u_{x1}$. However, due to the rotation of the ion distribution through the foot (given its large thickness $l_f \approx 4.1$) these particles still enter the shock ramp with a normal velocity close to zero which is a necessary condition for MRI [*Zank et al.*, 1996; *Lee et al.*, 1996].

Panel 4.4(b) is a contour plot of the energization factor of the final transmitted ion distribution. Clearly the particles that are most energized undergo MRI ($\varepsilon \gtrsim 3$) followed by D^u particles ($\varepsilon \sim 2-3$) and then S^u particles ($\varepsilon \sim 1-2$). Classes D^d, S^u, and NR all suffer net losses of energy, with $\varepsilon < 0$. No D^r or S^r particles were found. The particles that are least energized surround the local minimum located at $\mathbf{v}_1 \approx (-0.56, 0)$ corresponding to the NR source region.

Panel 4.4(c) presents *Gedalin*'s [1996] original figure that identifies ions that are initially transmitted but are then reflected in the downstream region, i.e. D^u or D^r particles. This is compared to our simulation in Figure 4.4(a), which shows a very similar source region for these downstream reflected particles: the D-separatrix is consistent in rotation angle and has a gradient of approximately unity in both panels. Figure 4.4(b) shows clearly that the distinction between classes D^d and D^u is that the latter group are energized when returning to the upstream region.

Qualitatively the trajectories in Figures 4.1-4.2 suggest that energization is due to drifts parallel to the upstream convective electric field. Figure 4.4(d), a contour plot in initial phase space of the particle displacement Δy_{gc}, shows that in general particles which have a positive displacement in their guiding center in y do indeed gain energy. However, the boundary $\Delta y_{gc} = 0$ does not exactly match the energization boundary $\varepsilon = 0$, particularly for the MRI particles and for the D^d and D^u boundary at large $v_{x1}/u_{x1} \gtrsim 0.8$. This is because even though some particles drift along the convective electric field they end up losing more energy through the shock because of the electrostatic potential, as described by (4.32).

Figure 4.5 compares these source regions to the analytic predictions derived in Section 4.4. Firstly, panel (a) plots the S-separatrix (4.1) using three values of the rotation angle $\Omega_{ci}\tau$: zero rotation $\Omega_{ci}\tau = 0°$ (red), $\Omega_{ci}\tau \simeq 70°$ (green) determined empirically from the simulation in the restricted phase space domain $v_{\perp 1}/u_{x1} < 0.4$, and $\Omega_{ci}\tau \simeq 94°$ (blue) using the theoretical prediction

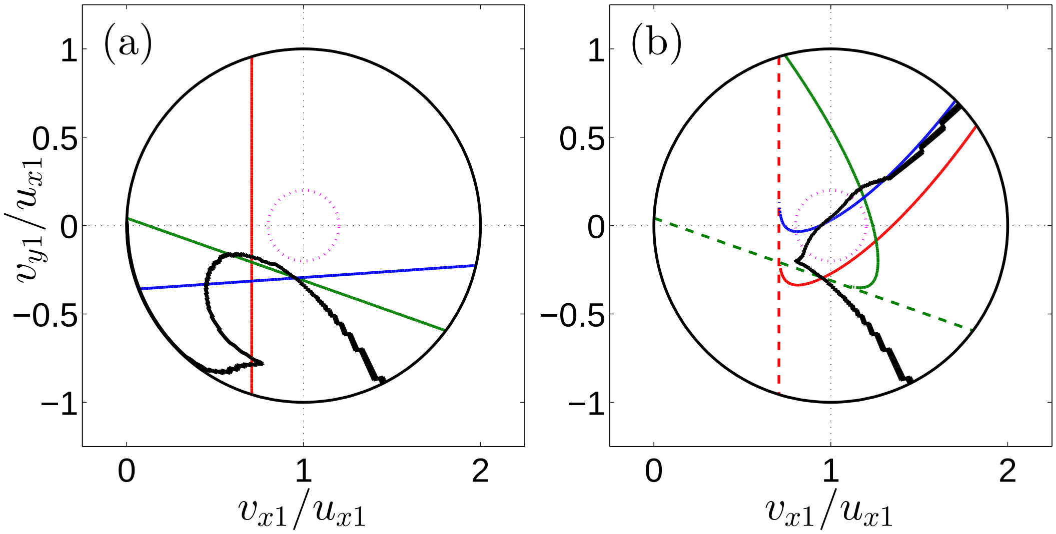

Figure 4.5: For the test-particle simulation using *Gedalin*'s [1996] shock parameters $M_A = 7.5$, $l_r = 0.225$, $B_2/B_1 = 3.2$, and $\Delta\varphi_E = 0.5$: (a) the observed S-separatrix (black) and the predictions of (4.1) for three values of the rotation angle $\Omega_{ci}\tau$: zero rotation $\Omega_{ci}\tau = 0°$ (red), $\Omega_{ci}\tau \simeq 70°$ (green) determined empirically from the simulation in the restricted phase space domain $v_{\perp 1}/u_{x1} < 0.4$, and $\Omega_{ci}\tau \simeq 94°$ (blue) using the theoretical prediction (4.5); (b) the observed D-separatrix (black) and the predictions of (4.10) with value of u_{y2} predicted theoretically by (4.15) and with rotation angles corresponding to the same colors as in panel (a). The dotted pink circles in panels (a) and (b) show the limit of *Gedalin*'s [1996] $v_{x1} - v_{y1}$ phase space range.

(4.5). These are to be contrasted with the numerical S-separatrix highlighted in black. Clearly the empirical value of $\Omega_{ci}\tau \simeq 70^\circ$ is the best prediction for the rotation of the reflection cutoff. In general the S^u source region is not bounded by a simple line in $v_{x1} - v_{y1}$ space; instead it is a complicated curve. Nonetheless, if we consider ions close to the thermal core with $v_{\perp 1} \lesssim 0.4u_{x1}$, then the empirical prediction (green) is a good approximation for the true source region.

Secondly, panel (b) plots the theoretical D-separatrix (4.10) using the input values $w_{x2} = -0.9v_A$, $w_{y2} = 1.5v_A$, $\Delta\varphi_E = 0.5$, and $u_{y2} \simeq -0.72v_A$, calculated from the relevant equations in *Gedalin*'s [1996] paper but not explicitly stated there, and the same rotation angles as in panel (a): $\Omega_{ci}\tau = 0^\circ$ (red) and $\Omega_{ci}\tau \simeq 70^\circ$ (green). In this panel, the black line describes the numerical D-separatrix. The S-separatrixes from panel (a) are also shown as dashed lines in the same colors. *Gedalin*'s [1996] original calculations did not take into account the rotation by the distribution's natural gyromotion across the shock and therefore is equivalent to the red solid curve. Both this prediction and the green solid prediction which includes the gyromotion agree poorly with the simulation results, lying outside the original domain of interest (highlighted within the pink dotted circle). This is in contrast to *Gedalin*'s [1996] claimed results in Figure 4.4(c): he finds perfect agreement between the analytic prediction (4.10) and his test-particle simulations.

We find that we can produce a similar result to *Gedalin*'s [1996] if we neglect rotation and increase the magnitude of the deflection speed $|u_{y2}|$; the latter shifts the D-separatrix vertically upwards while preserving its shape. By trial and error, a deflection speed of $u_{y2} = -3v_A$ produces a reflection separatrix (blue) that is consistent with the simulation results. Nevertheless, this prediction is unphysical since it neglects the rotation by the distribution's natural gyromotion across the shock foot and ramp. Furthermore, the applicability of (4.10) at the trailing edge of the ramp is questioned: the spatial magnetic field still varies extensively in the overshoot region $x/\lambda_i \simeq 0.1 - 2.5$ from Figure 4.3(a), and therefore the local gyrocenter, gyrospeed, and gyrophase of the particle are no longer constant. Rather, (4.10) should be applied at the trailing edge of the overshoot $x/\lambda_i \simeq 2.5$ where these parameters reach their downstream constant values. Indeed we find that we can exactly recover the observed D-separatrix analytically (not shown here) by substituting the actual values of $\mathbf{v}_2$ and $\mathbf{w}_2/v_A = (2.35, 0)$ taken at the trailing edge of the overshoot $x = 2.5\lambda_i$ in (4.10).

4.5.2 Confirmation and extension of *Lever et al.*'s [2001] test-particle simulations

Lever et al. [2001] performed multiple 1-D test-particle simulations using piecewise linear field profiles for the spatial magnetic field and electric potential (Figure 4.3b). They extracted these field profiles as functions of M_A from their 1-D hybrid simulations, finding

$$\Delta\varphi_{E,\max} = 0.775 - 0.024 M_A, \tag{4.33a}$$

$$\Delta\varphi_{E,2} = 0.644 - 0.047 M_A, \tag{4.33b}$$

$$\frac{B_o}{B_1} = 0.294 + 0.799 M_A, \tag{4.33c}$$

$$\frac{B_2}{B_1} = r \tag{4.33d}$$

where r is the Rankine-Hugoniot compression ratio. These profiles have a shock ramp and overshoot but no shock foot. *Lever et al.* [2001] calculated the source regions for S^u, D^u, and MRI particles for a $M_A = 5$ shock with $l_r = 0.6$, $B_2/B_1 = 2.6$, $\Delta\varphi_{E,\max} = 0.655$, and $\Delta\varphi_{E,2} = 0.409$.

Performing test-particle simulations on a shock with the same field profiles and shock parameters as *Lever et al.* [2001] leads to the results shown in Figure 4.6. The source regions for each particle class are shown in Figure 4.6(a). Populations of NR, S^u, MRI, D^d, and D^u are found, as well as a small population of D^r particles that turn around in the ramp region. These source regions are qualitatively consistent with *Lever et al.*'s [2001] original results except those authors only identified S^u, D^u, and MRI particle groups in their test-particle simulations.

Figure 4.6(b) shows that MRI particles are highly energized ($\varepsilon \gtrsim 3$) and that (in this case) S^u and D^u particles achieve lower but comparable gains in energy ($\varepsilon \sim 1 - 3$). Interestingly, there are some S^u particles which lose energy through the shock, located in the phase space range $v_{x1}/u_{x1} = [0, 0.3]$ and $v_{y1}/u_{x1} = [-0.7, 0]$ near to the MRI domain. Note that D^d and NR particles lose energy on crossing the shock. Figure 4.6(d) is a contour plot of Δy_{gc} showing that most particles which drift along the convective electric field are energized. Moreover the energization boundary $\varepsilon = 0$ and the displacement boundary $\Delta y_{gc} = 0$ differ because for some particles the energy gain by drifting along the convective electric field is still less than the energy loss they suffer on traversing the electrostatic potential, i.e. $0 < E_y \Delta y_{gc} < -e\Delta\phi_E$.

Figure 4.6(c) compares the S- and D-separatrixes to the source regions

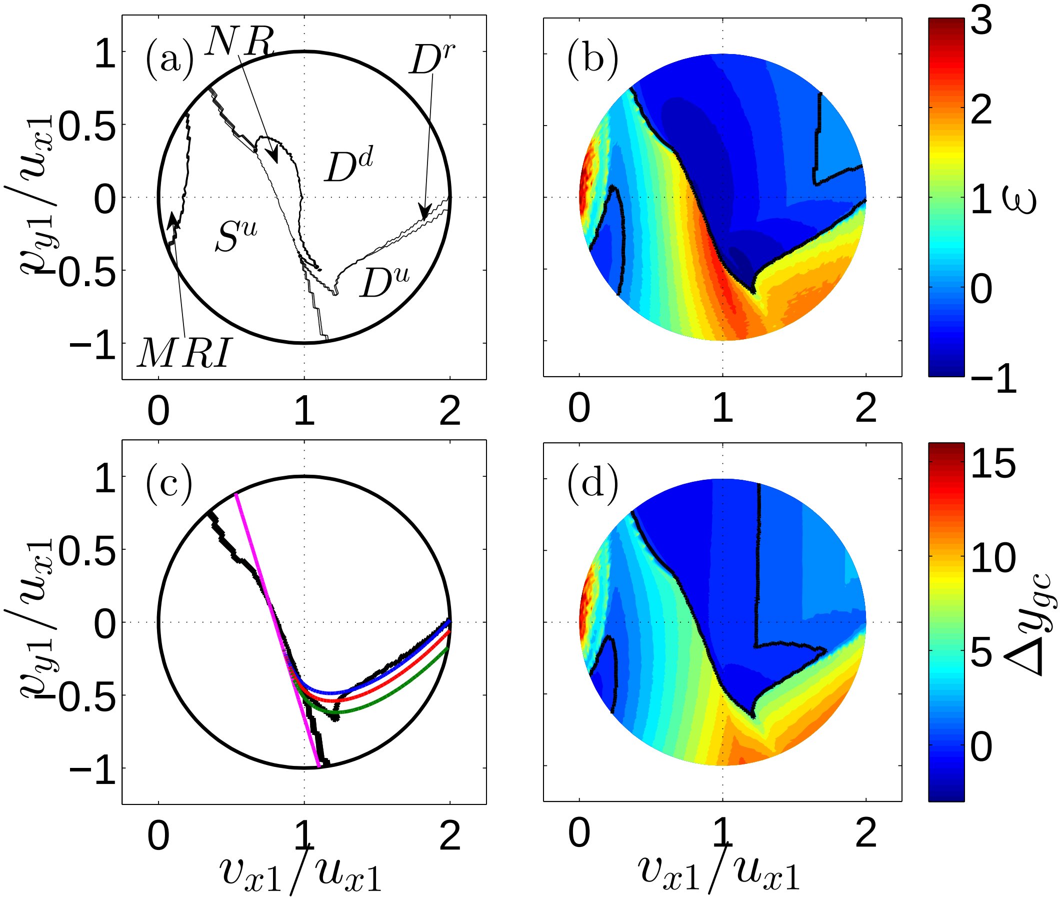

Figure 4.6: Panels (a), (b), and (d) are the same plots as Figure 4.4(a), 4.4(b), and 4.4(d), respectively, but for the test-particle simulation having *Lever et al.*'s [2001] shock parameters: $M_A = 5$, $l_r = 0.6$, $B_2/B_1 = 2.6$, and $\Delta\varphi_E = 0.655$. Panel (c) compares the theoretical S-separatrix (4.1) in pink to the combined boundary of S^u and MRI particles in black. The blue, red, and green lines plot the D-separatrix (4.10) for three values of the velocity shift in v_y: those predicted theoretically in (4.15) and (4.16), and zero, respectively. This is compared to the combined boundary of D^r and D^u particles in black.

predicted numerically in the test-particle simulation. Black lines mark the combined regions of (1) S^u, S^r, and MRI particles and (2) D^u and D^r particles. The S-separatrix (4.1) accurately describes the boundary between initial reflection (S^u, S^r, and MRI) versus initial transmission (NR, D^u and D^d) except at $v_{x1}/u_{x1} \approx [0.35, 0.65]$ and $v_{y1}/u_{x1} \approx [0.3, 0.7]$ where the true boundary lies to the left of the predicted cutoff. The green, red, and blue lines plot the D-separatrix (4.10) using velocity shifts predicted by (4.15), (4.16), and $u_{y2} = 0$, respectively. Given the relatively thin nature of the shock ramp $l_r = 0.6$, little deflection is predicted by (4.15) and (4.16), with $u_{y2} \approx 0.68 v_A$ and $\approx 0.41 v_A$ respectively. Hence the difference in these reflection cutoffs is minimal. However from inspection, it appears that the green curve using *Gedalin*'s [1996] prediction for the deflection (4.15) best matches the true boundary.

4.5.3 Subcritical shock profile

Here we run test-particle simulations using a subcritical laminar profile, with a ramp but no foot or overshoot, to examine the changes in particle source regions and associated energization as a function of ramp thickness and electrostatic potential. The magnetic field profile $B(x)$ increases monotonically from B_1 for $x \ll 0$ to B_2 at $x \gg 0$ according to

$$B(x) = B_1 + \frac{1}{2}(B_2 - B_1)\left[1 + \tanh\left(\frac{6x}{L_r}\right)\right]. \tag{4.34}$$

In each simulation the profile of the electrostatic potential mimics $B(x)$ via

$$\phi_E(x) = \Delta\phi_E \left(\frac{B(x) - B_1}{B_2 - B_1}\right), \tag{4.35}$$

for instance by analogy with *Kuncic et al.* [2002], and the electric field has components $\mathbf{E}(x) = (-d\phi_E(x)/dx, u_{x1}B_1, 0)$. The parameters $\Delta\phi_E$ and L_r are varied from run to run, where the latter indirectly controls the maximum reflection time τ. The upstream ion distribution has initial velocities between $\theta_1 = 0°$ and $360°$ and $v_{\perp 1} = 0$ and u_{x1} and is injected at the leading edge of the foot or ramp.

In our simulations we use the same $M_A = 6$ and downstream magnetic field strength $B_2/B_1 = 4$ but vary $l_r = 0.9, 1.6, 2.5$ and $v_c^E/v_A = 4$ or 5, the latter meaning $\Delta\varphi_E \simeq 0.44$ or 0.69. The spatial magnetic field profiles (4.34) are shown in Figure 4.7(a).

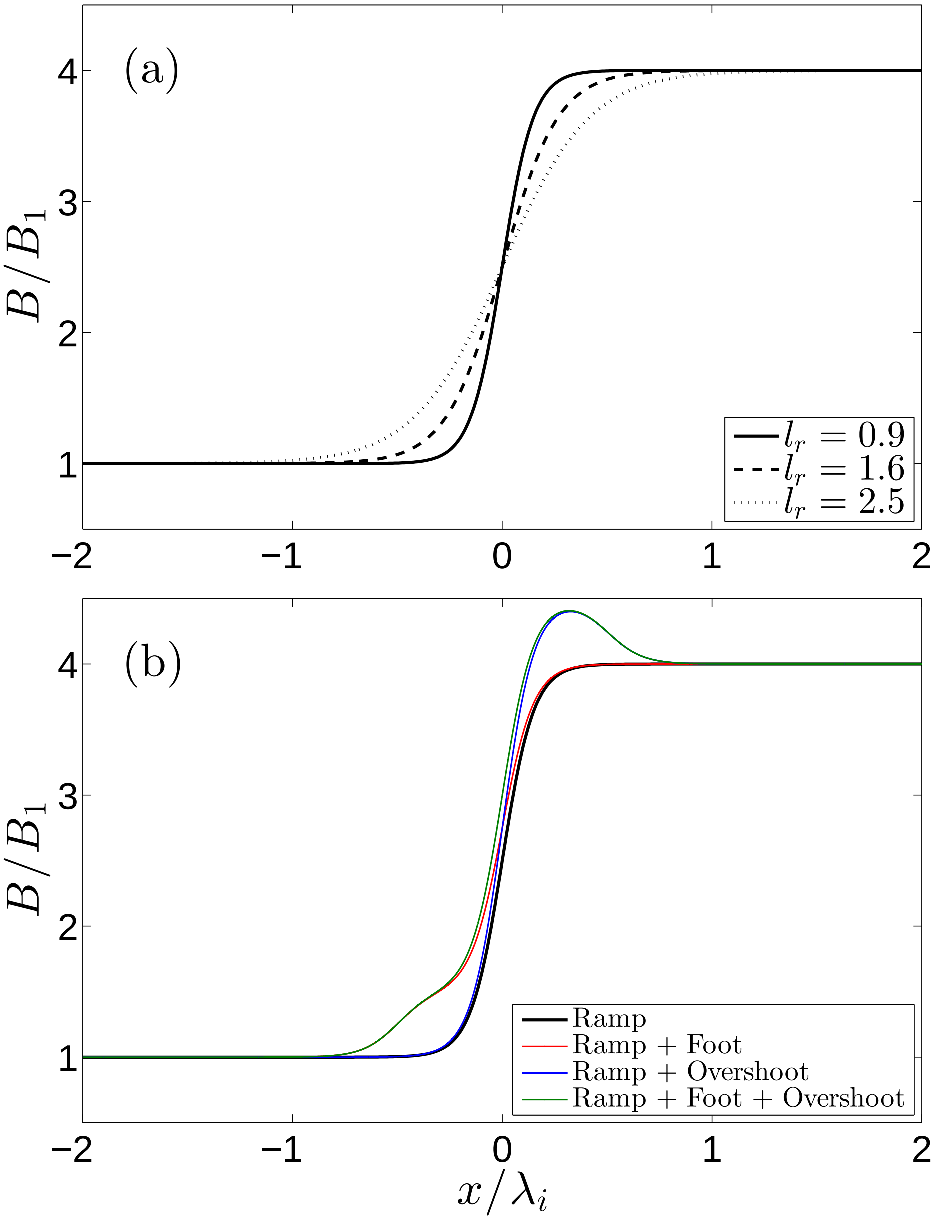

Figure 4.7: The magnetic field profile used in our test-particle simulations with (a) only a ramp of varying thickness, and (b) a ramp of fixed thickness $l_r = 0.9$ but the additional spatial features of a foot and/or overshoot. The ramp region in panel (a) is defined to be between $x = -l_r/2$ and $x = l_r/2$.

Substituting $B_o = B_2 = 4B_1$ and $M_A = 6$ into (4.4) yields the predicted work done by magnetic deflection

$$\frac{\langle W_{Bx}\rangle}{\frac{1}{2}m_i u_{x1}^2} \simeq \frac{2l_r^2}{75}. \tag{4.36}$$

However in Chapter 3 the replace l_r by $l_r/2$ was found to be a better approximation, giving

$$\frac{\langle W_{Bx}\rangle}{\frac{1}{2}m_i u_{x1}^2} \simeq \frac{l_r^2}{150}. \tag{4.37}$$

This is justified by noting that the linear portion of the magnetic profiles in Figure 4.7(a) are primarily between $x/\lambda_i = -l_r/4$ and $x/\lambda_i = l_r/4$ and also that $B(-l_r\lambda_i/4)/B_0 \approx 1.14$ and $B(l_r\lambda_i/4)/B_0 \approx 3.86$. Hence $\langle W_{Bx}\rangle/(\frac{1}{2}m_i u_{x1}^2) \simeq 0.0054, 0.017$, and 0.042 for our chosen values of $l_r = 0.9, 1.6$ and 2.5, meaning that magnetic deflection is unimportant for these shock parameters and therefore $v_c \simeq v_c^E$.

Figure 4.8 plots the particle source regions (left column), energization contours (middle column), and theoretical reflection cutoffs (right column) for test-particle simulations with these profiles for $\Delta\varphi_E \simeq 0.69$ and varying $l_r = 0.9, 1.6$, and 2.5. The MRI domain decreases as l_r increases, disappearing for $l_r = 2.5$; complementing this an S^r class develops for $l_r \gtrsim 1.6$, cannibalizing the MRI domain, for increasing l_r. Moreover, the S^u domain changes significantly as l_r increases, decreasing the D^u domain. The D^r domain increases with increasing l_r.

Comparing the particle source regions with the energization boundary $\varepsilon = 0$ suggests that primarily S^u and D^u particles are energized (and MRI for small l_r), corresponding to ions being energized mostly in the upstream region after reflection. This is particularly evident for the simulations with $l_r = 0.9$ and $l_r = 1.6$, where the phase space region $\varepsilon > 0$ accurately coincides with the source regions of S^u and D^u particles. However, for $l_r = 2.5$ this is no longer the case since D^r and S^r particles are now also enclosed within the energization region $\varepsilon > 0$. This is because the shock ramp is now sufficiently thick for particles that are reflected and turn around in the ramp to drift far enough along the convective electric field that they gain more energy than they lose from the electrostatic potential. Curiously, the boundary between D^r and D^u appears to remain fixed and independent of the ramp thickness in these simulations.

From inspection, the fractional energy gain of S^u particles depends on v_{x1}, being most evident for the $l_r = 0.9$ case. For D^u ions the local maximum at

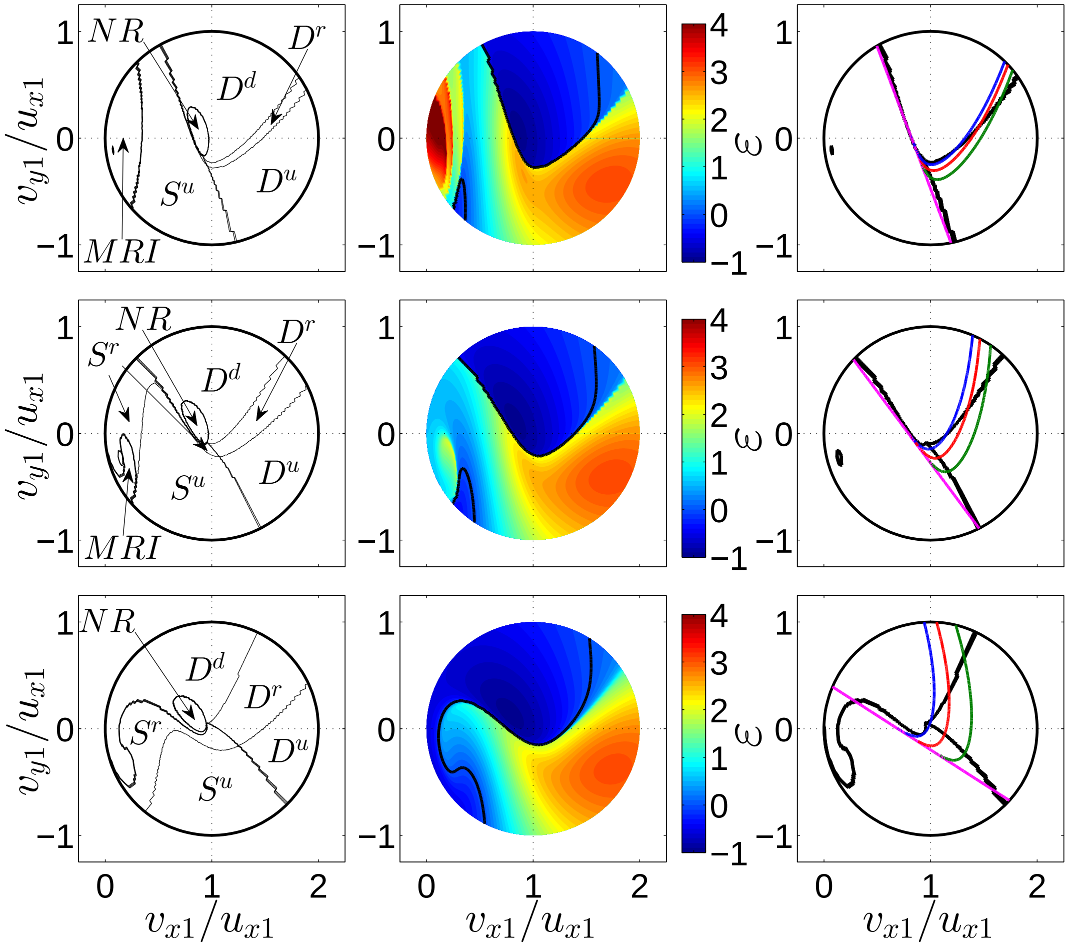

Figure 4.8: Results of test-particle simulations with varying ramp thickness $l_r = 0.9$ (1st row), $l_r = 1.6$ (2nd row), and $l_r = 2.5$ (3rd row) but common shock parameters $M_A = 6$, $B_2/B_1 = 4$, and $\Delta\varphi_E \simeq 0.69$: (left column) particle source regions, (middle column) energization profile and $\varepsilon = 0$ contour, and (right column) the analytic S- and D-separatrixes compared to the numerical source regions using the same colour coding as in Figure 4.6(b).

$\mathbf{v}_1/u_{x1} \simeq (1.7, -0.4)$ appears to remain fixed regardless of the ramp thickness. Furthermore, the energization contours about the local maximum have the same variations and magnitudes for all three values of l_r. MRI particles are most strongly energized for small l_r but disappear altogether for $l_r = 2.5$.

Finally the right column of Figure 4.8 plots the same analytic predictions as in Sections 4.5.1 and 4.5.2. For $l_r = 0.9$ and 1.6, we find excellent agreement between the theoretical S-separatrix (4.1) using (4.5) and the numerical results. However, for $l_r = 2.5$ the true boundary is a complex curve and deviates from the linear separatrix at large perpendicular speeds $v_{\perp 1}/u_{x1} \gtrsim 0.7$. The situation is different to the D-separatrix (4.10): for $l_r = 0.9$ there is reasonable agreement between the analytic and numerical results but for $l_r \gtrsim 1.6$ the agreement is poor except for the blue curve at small $v_{\perp 1}/u_{x1} \lesssim 0.2$. Note that the analytic predictions show that shape of the reflection separatrix (4.10) is the same for varying u_{y2} but that increasing u_{y2} moves the separatrix left and upwards. Moreover the three reflection cutoffs converge to the same curve as $l_r \to 0$ since $u_{y2} \to 0$ in (4.15) and (4.16).

Figure 4.9 shows the same 3 cases as Figure 4.8 but for a lower cross-shock potential $\Delta\varphi_E \simeq 0.44$. The phase space domains are very similar for the particle classes, although the MRI domain is smaller even for $l_r = 0.9$ and the reduction in the electrostatic cutoff speed from $v_c^E = 5v_A$ to $v_c^E = 4v_A$ decreases the phase space regions of S^u and MRI particles while increasing the domain of class D particles. Furthermore, for $l_r = 0.9$ the energization factor for MRI has noticeably dropped from $\varepsilon \gtrsim 4$ to $\varepsilon \simeq 1 - 2$ and similarly for D^u particles from $\varepsilon \gtrsim 3 - 4$ to $\varepsilon \simeq 2 - 3$. These trends are also evident for $l_r = 1.6$ and 2.5 simulation cases. Thus reducing $\Delta\varphi_E$ and so v_c^E from $5v_A$ to $4v_A$ decreases the number and energization of MRI and S^u particles even for small l_r, while increasing the domain but decreasing the energy of D particles.

4.5.4 Supercritical shock profile

Now we investigate the effects on the particle source regions and associated energization due to spatial variations in the electric and magnetic field profiles. Specifically we add supercritical shock features to the laminar shock profile such as the foot and the overshoot regions.

Firstly, we use a profile with foot and ramp structures, shown in Figure

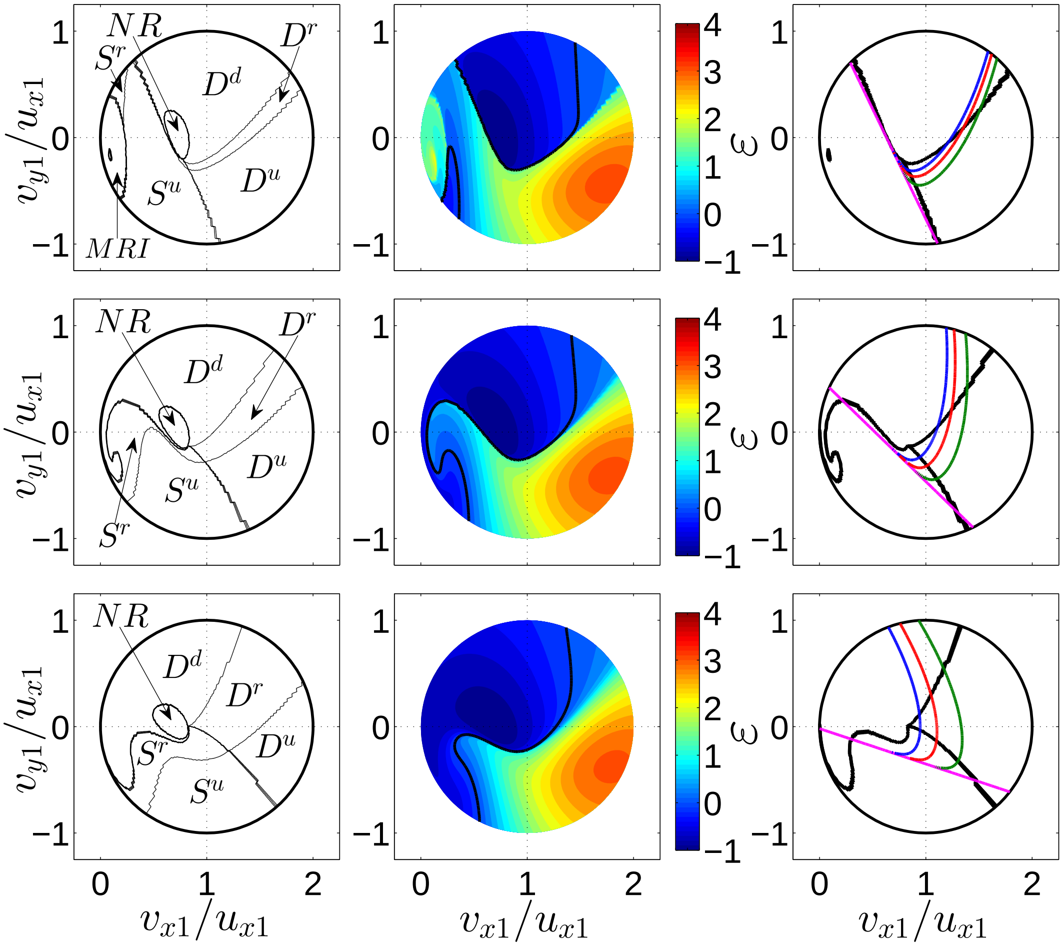

Figure 4.9: Same as Figure 4.8 but with $\Delta\varphi_E \simeq 0.44$.

4.7(b) with

$$B(x) = B_1 + \frac{1}{2}(B_2 - B_1 - B_f)\left[1 + \tanh\left(\frac{6x}{L_r}\right)\right] + \\ \frac{1}{2}B_f\left[1 + \tanh\left(\frac{6(x + L_f/2)}{L_f}\right)\right]. \tag{4.38}$$

Here L_f and B_f are the length scale and magnitude of the foot, respectively, and the spatial regions of the profile are divided into the foot ($x = -L_f$ to $x = 0$) and the ramp ($x = -L_r/2$ to $x = L_r/2$). Therefore the total shock width is $L \approx L_f + L_r/2$, which is the distance from the leading edge of the foot to the trailing edge of the ramp. Figure 4.7(b) plots (4.38) for $L_f = 1.0\ \lambda_i$ and $B_f = 0.5\ B_1$.

Secondly, we use a profile with ramp and overshoot structures, shown in Figure 4.7(b) with

$$B(x) = B_1 - B_o + \frac{1}{2}(B_2 - B_1 + B_o)\left[1 + \tanh\left(\frac{6x}{L_r}\right)\right] + \\ \frac{1}{2}B_o\left[1 + \tanh\left(\frac{6(-x + L_o/2)}{L_o}\right)\right]. \tag{4.39}$$

Here L_o and B_o are the length scale and magnitude of the overshoot, respectively, and the spatial regions of the profile are divided into the ramp ($x = -L_r/2$ to $x = L_r/2$) and the overshoot ($x = 0$ to $x = L_0$). Therefore the total shock width is $L \approx L_o + L_r/2$, which is the distance from the leading edge of the ramp to the trailing edge of the overshoot. Figure 4.7(b) plots (4.39) for $L_o = 1.0\ \lambda_i$ and $B_o = 0.5\ B_1$.

Finally, we use a profile with a foot, ramp, and overshoot, shown in Figure 4.7(b) and modelled with

$$B(x) = B_1 - B_{fo} + \frac{1}{2}(B_2 - B_1)\left[1 + \tanh\left(\frac{6x}{L_r}\right)\right] + \\ \frac{1}{2}B_{fo}\left[2 + \tanh\left(\frac{6(x + L_{fo}/2)}{L_{fo}}\right) + \\ \tanh\left(\frac{6(-x + L_{fo}/2)}{L_{fo}}\right)\right]. \tag{4.40}$$

Here L_{fo} and B_{fo} are the length scale and magnitude of the foot or overshoot and the maximum magnetic field strength is $B_2 + B_{fo}$. As for the spatial profile is divided between the foot ($x = -L_{fo}$ to $x = -L_r/2$), ramp ($x = -L_r/2$ to $x = L_r/2$) and overshoot ($x = L_r/2$ to $x = L_{fo}$), and the total shock width is $L \approx 2L_{fo}$, the distance from the leading edge of the foot to the end of the overshoot. Figure 4.7(b) plots (4.40) for values of $L_{fo} = 1.0\ \lambda_i$ and $B_{fo} = 0.5\ B_1$.

We run test-particle simulation using the spatial profiles from Figure 4.7(b) and with the common shock parameters: $M_A = 6$, $B_2 = 4B_1$, $l_r = 0.9$, and $v_c^E = 5v_A$ or equivalently $\Delta\varphi_E \simeq 0.44$. Likewise, in the test-particle simulations with subcritical shock profiles, the spatial profile of the electrostatic potential $\Delta\phi(x)$ is given by (4.35). Figure 4.10 plots the energization profiles from these test-particle simulations and labels the source regions of the major particle classes: S^u, MRI, and D^u.

Each panel is qualitatively similar, showing similar variation and magnitude in the energization of S^u and D^u particle groups. However the energization of MRI particles is markedly different across the various shock profiles. The presence of the foot significantly alters the scope and shape of the MRI domain in phase space; the domain is now reduced in size and its shape more complicated. Furthermore, particles that are most energized ($\varepsilon > 4$) are now localized in phase space with a small but finite v_{x1} rather than an almost zero initial normal velocity $v_{x1} \approx 0$ in simulations without a foot. The foot also rotates the profile anti-clockwise and is particularly evident when comparing the S^u separatrix with and without the foot. With the inclusion of an overshoot region there is marginal change in the particle energization; little difference is observed between the bottom and top panels for simulations with and without an overshoot, respectively. While class S^u particles are somewhat further energized by the addition of an overshoot structure, presumably due to the increase in the electrostatic potential, D^u particles do not have noticeably increase energy gains. In conclusion, Figure 4.10 shows that shocks with an appreciable foot have significantly reduced MRI energization domains, while the addition of an overshoot region does not affect the D^u particles but does increase the energization factor and domain for S^u particles.

4.6 Discussion

4.6.1 MRI energization

The detailed structure of the energization contours for MRI particles are further examined in Figure 4.11. Here we see that the energization profiles have layered contours which is tempting to associate with an additional "kick" a particle receives from every reflection. This suspicion is confirmed by calcu-

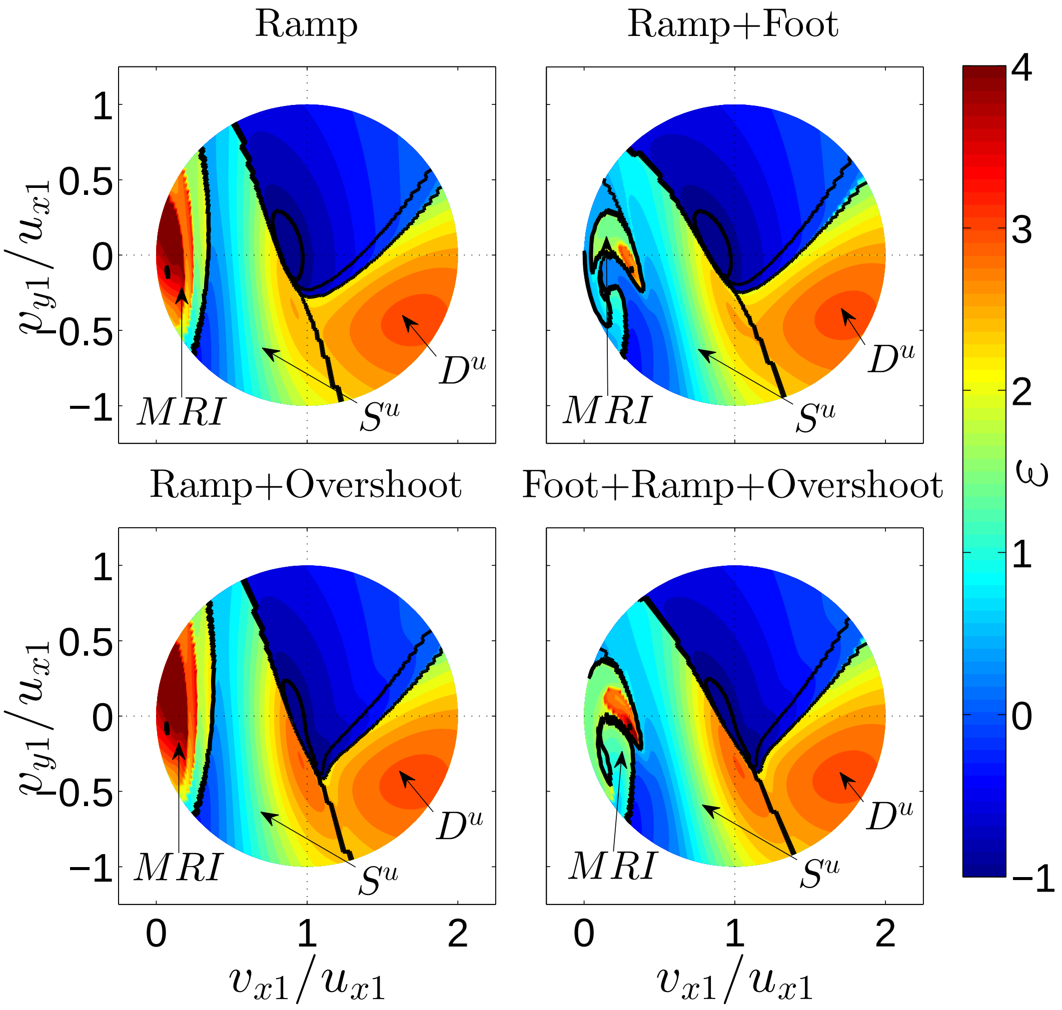

Figure 4.10: Energization profiles labeled with major particle classes for shock profiles with (a) ramp only, (b) foot and ramp structures, (c) ramp and overshoot structures, and (d) foot, ramp, and overshoot structures. Here the ramp thickness is fixed $l_r = 0.9$ and $M_A = 6$, $B_2 = 4B_1$, and $v_c^E = 5v_A$. The length scale and magnitude of the foot or overshoot structures are 1.0 λ_i and 0.5 B_1, respectively.

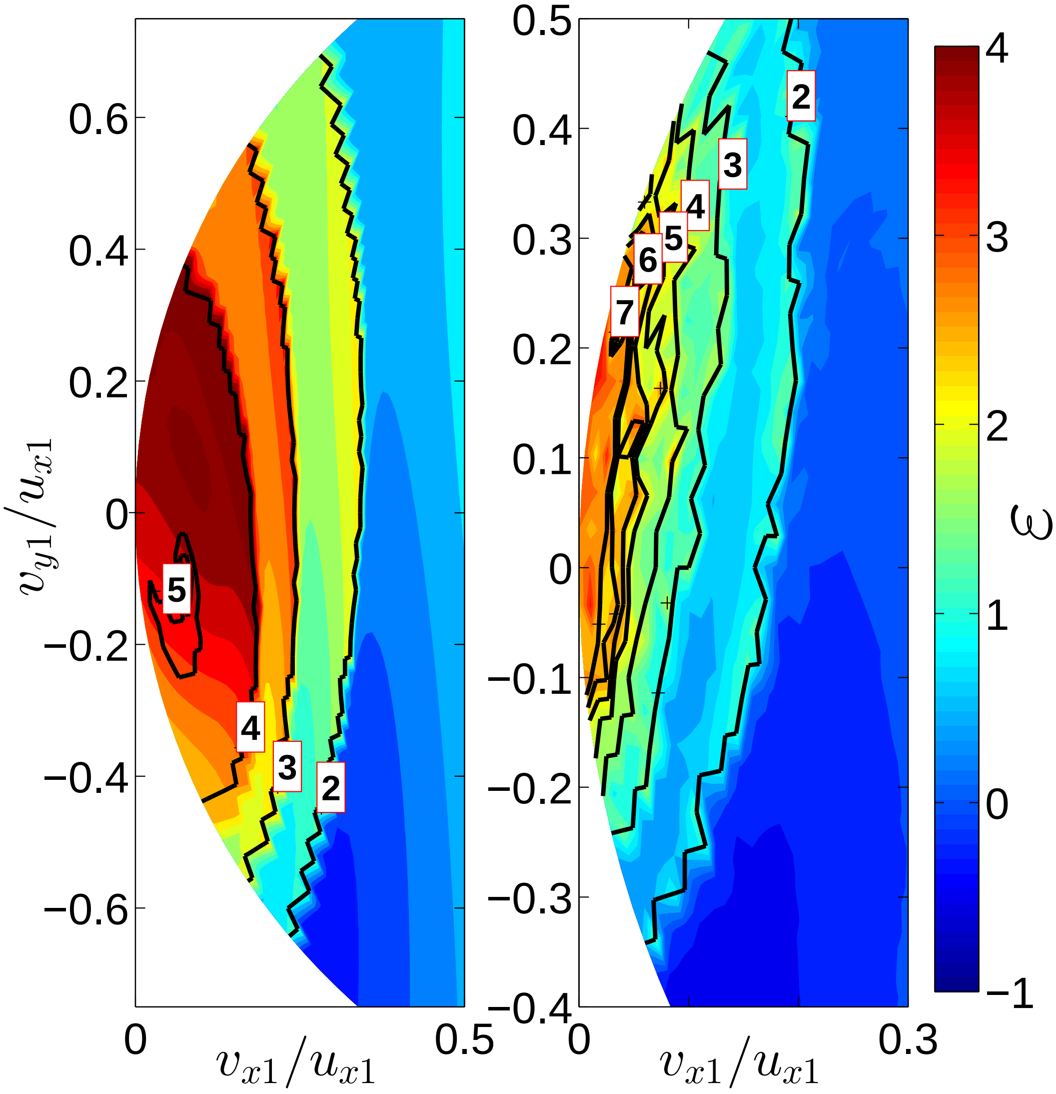

Figure 4.11: Zoomed MRI source regions of ε contour plots from Figures 4.8 (left) and 4.6 (right). Overlay are contour lines counting the number of particle reflections in the upstream and ramp region $x < L_r$.

lating, independently, the number of times a particle is reflected before final transmission. The reflection count is overlay as contour lines in Figure 4.11; it closely matches the boundaries between the fractional energy gains of the MRI particles.

4.6.2 Fractional populations of particle classes

Figure 4.12 presents the fractional populations of each particle class (4.6) as functions of the upstream ion thermal speed v_{th1} for (a) *Gedalin*'s [1996] test-particle simulations, and (b) *Lever et al.*'s [2001] test-particle simulations. (Explicitly plotted are the fractional contributions to the cumulative reflection fraction.) The theoretical fractional population (4.8) of S^u particles is also plotted in each panel. The studied thermal range is restricted to $v_{th1}/u_{x1} = [0.05, 0.4]$ since for $v_{th1}/u_{x1} \gtrsim 0.4$ the total number density is no longer conserved, i.e. (4.6) integrated over the entire phase space domain is less than unity. For a certain particle class its population fraction can be extracted from these Figures by subtracting the cumulative total without its contribution from the cumulative total with its contribution. Population fractions from here on are stated as their explicit values not their cumulative values.

For *Gedalin*'s [1996] test-particle simulations the distribution is mainly comprised of D^u and D^d particles, where $\alpha_{D^u} \simeq 41 - 62\%$ and $\alpha_{D^d} \simeq 43 - 46\%$ as v_{th1}/u_{x1} varies. The next largest group are S^u particles, increasing from $\alpha_{S^u} = 0\%$ to $\alpha_{S^u} \simeq 9.8\%$ with increasing v_{th1}, and then D^r particles, which decrease from $\alpha_{D^r} \simeq 5.6\%$ to $\alpha_{D^r} = 0\%$ with increasing v_{th1}. We find that the predicted α_{S^u} agrees well with the numerical results in the range $v_{th1}/u_{x1} \lesssim 0.25$ but above $v_{th1}/u_{x1} \approx 0.25$ the theoretical value slightly overpredicts the true fractional population. This can be easily explained by examining Figures 4.4(a) and 4.5(a): the lower sector bounded by the S-separatrix (green) in Figure 4.5(a) consists of S^u particles as well as MRI and D^d particles, so as v_{th1} increases the actual population will be less than the population calculated if the sector consisted solely of S^u particles. There are very few MRI particles, with their maximum fractional population of $\alpha_{MRI} \simeq 0.9\%$ occuring at the maximum thermal speed $v_{th1}/u_{x1} = 0.4$; this is because MRI particles are largely nonthermal with initial gyrospeeds of $v_{\perp 1}/v_{th1} \gtrsim 2$. Thus we find that for the shock profile and parameters of *Gedalin* [1996] the D^u particles have the greatest contribution to the total energization of the ion distribution given their large fractional population and energization factor.

In *Lever et al.*'s [2001] test-particle simulations the fractional populations

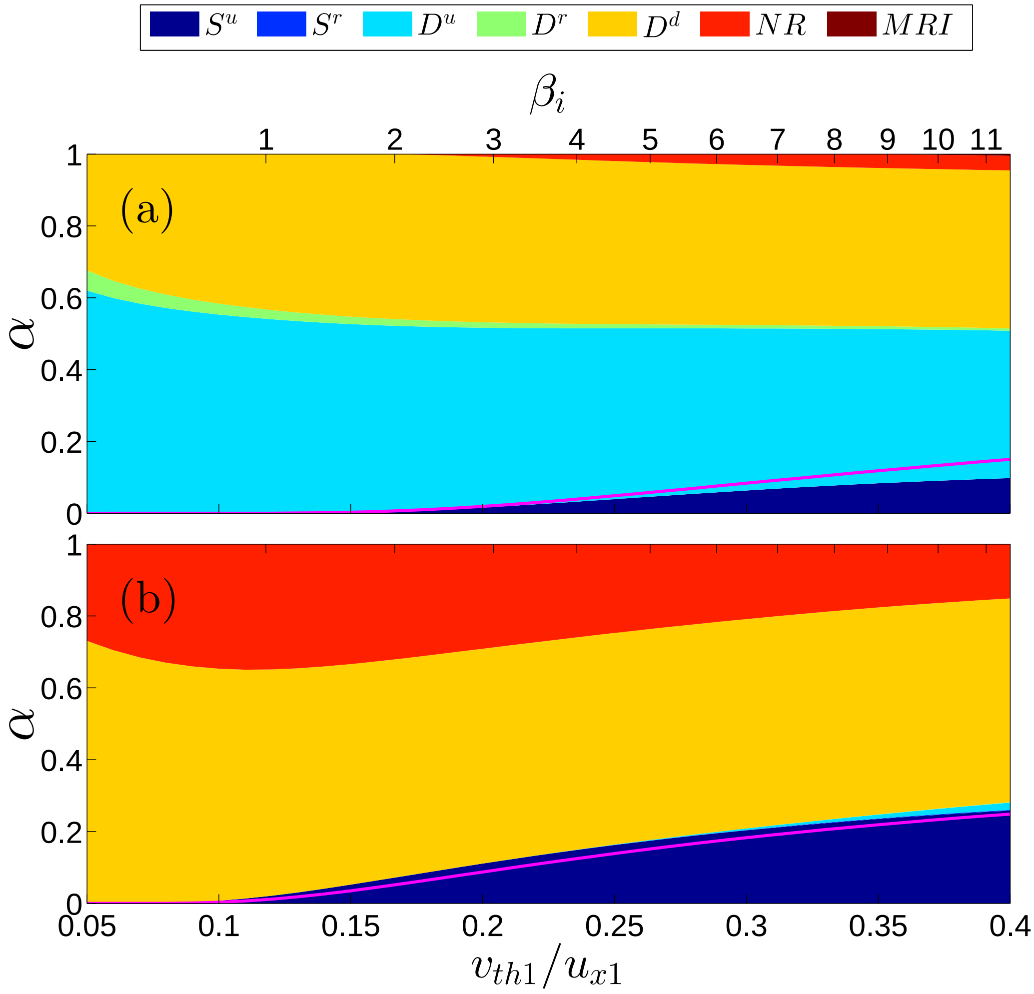

Figure 4.12: The calculated reflection efficiencies α of each particle class are color-coded as functions of the upstream thermal speed v_{th1} in (a) *Gedalin*'s [1996] test-particle simulations, and (b) *Lever et al.*'s [2001] test-particle simulations. The pink curve in each panel is the theoretical reflection efficiency (4.8) of S^u particles.

of each particle class in descending order for $0.05 \leq v_{th1}/u_{x1} \leq 0.4$ are: $\alpha_{D^d} \simeq 57-73\%$, $\alpha_{NR} \simeq 15-35\%$, $\alpha_{S^u} \simeq 0-26\%$, and $\alpha_{D^u} \simeq 0-2\%$. All other particle classes have negligible populations. Similar to *Gedalin*'s [1996] simulation, there are very few MRI particles; their maximum fractional population is $\alpha_{MRI} \approx 0.1\%$ at $v_{th1}/u_{x1} = 0.4$. On the other hand, the prediction (4.8) for α_{S^u} agrees very well with the numerical results for all values of v_{th1}. Therefore, for *Lever et al.*'s [2001] test-particle simulation and chosen shock parameters the S^u particles (not the D^u particles) have the greatest contribution to the total energization of the ion distribution because of their large fractional population and energization factor. This is important because *Lever et al.*'s [2001] shock profiles and parameters are derived from hybrid simulations whereas those of *Gedalin* [1996] are not.

Figure 4.13 is analogous to Figure 4.12 but for the test-particle simulations in Figures 4.8. At a glance the results are more similar to the shock profiles of *Lever et al.* [2001] than *Gedalin* [1996], at least for $l_r = 0.9$ and 1.6, but major differences are apparent from both for $l_r = 2.5$. Panels (a) and (b) correspond to the simulation cases $l_r = 0.9$ and $l_r = 1.6$, respectively, and are qualitatively similar; the distribution is mainly comprised of D^u and NR particles for small $v_{th1}/u_{x1} \lesssim 0.15$, but makeup of the distribution changes noticeably with increasing v_{th1} as the fractional populations of S^u, S^r, D^r, and D^u particles increase. Panel (c), corresponding to the $l_r = 2.5$ simulation case, is markedly different from the simulation results in panels (a) and (b). Class S^r and D^r particles now constitute a significant population of the ion distribution for all ranges of v_{th1}; specifically $\alpha_{S^r} + \alpha_{D^r} \simeq 90\%$ at $v_{th1}/u_{x1} = 0.05$ whereas $\alpha_{S^r} + \alpha_{D^r} \simeq 38\%$ at $v_{th1}/u_{x1} = 0.4$. Furthermore, there is little variation between the particle populations above $v_{th1}/u_{x1} \simeq 0.25$. Thus the fractional populations of each particle class are sensitive to the ramp thickness l_r.

Figure 4.14 now examines the calculated fractional populations for the same profiles as Figure 4.13 but with a lower potential $\Delta\varphi_E \simeq 0.44$. Major differences in particle populations are again apparent. As expected, more particles now surpass the lower electrostatic potential; populations of initially transmitted particles, i.e. D class particles, constitute at least $\gtrsim 63\%$ of the particle distribution over the entire thermal range in panels (a), (b), and (c). As a result, the population of S^u particles is reduced but still agrees with the analytic prediction (4.8).

Figure 4.15 plots the explicit fractional populations of MRI, S^u, and D^u particles from the test-particle simulations with varying spatial profiles in Figure 4.7(b). Qualitatively, Figure 4.10 shows reduction of the MRI domain for

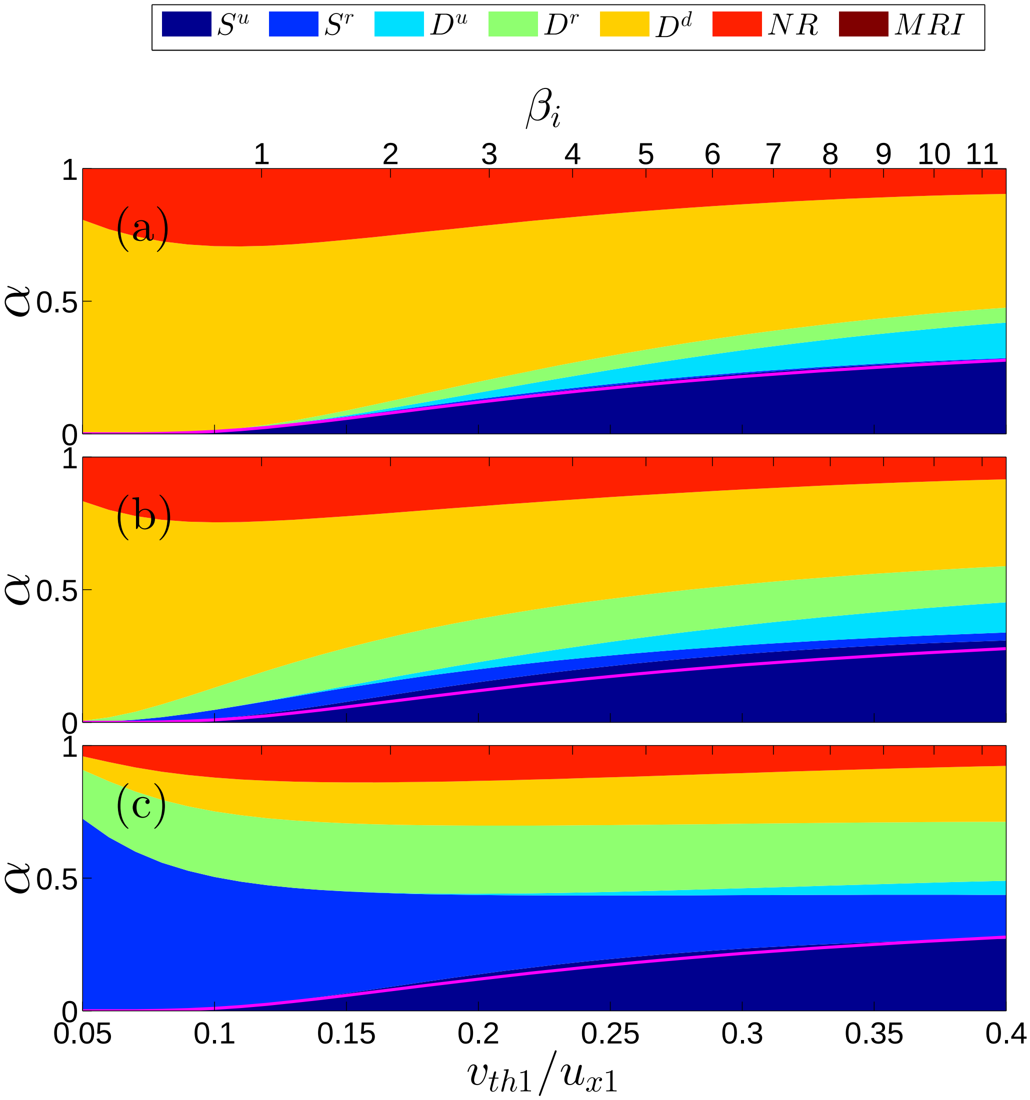

Figure 4.13: Same as Figure 4.12 but for the test-particle simulations in Figure 4.8 where (a) $l_r = 0.9$, (b) $l_r = 1.6$, and (c) $l_r = 2.5$.

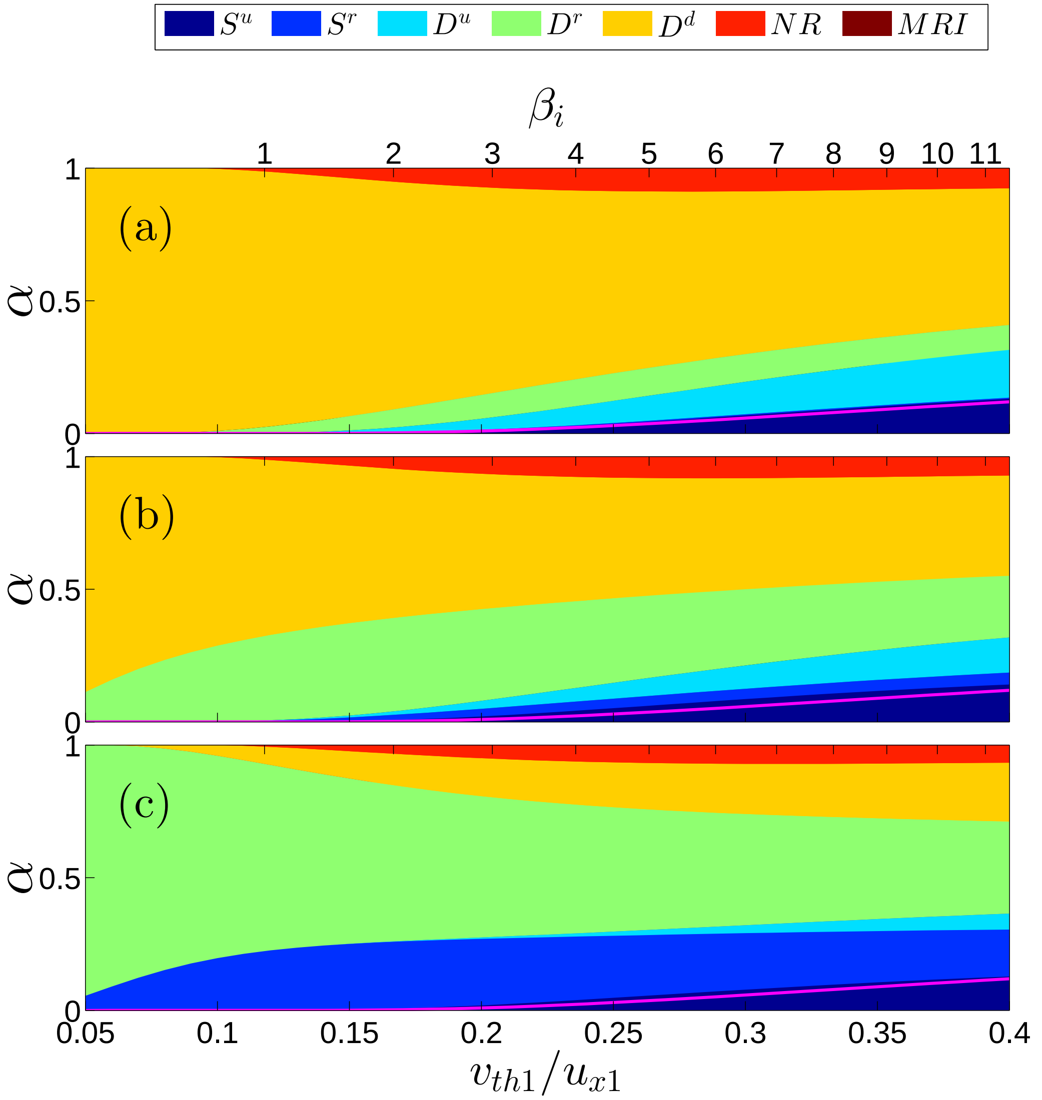

Figure 4.14: Same as Figure 4.12 but for the test-particle simulations in Figure 4.9 where (a) $l_r = 0.9$, (b) $l_r = 1.6$, and (c) $l_r = 2.5$. The difference in conditions between Figures 4.8 and 4.9 (and 4.13 versus 4.14) is that $\Delta\varphi_E = 0.44$ here rather than 0.69.

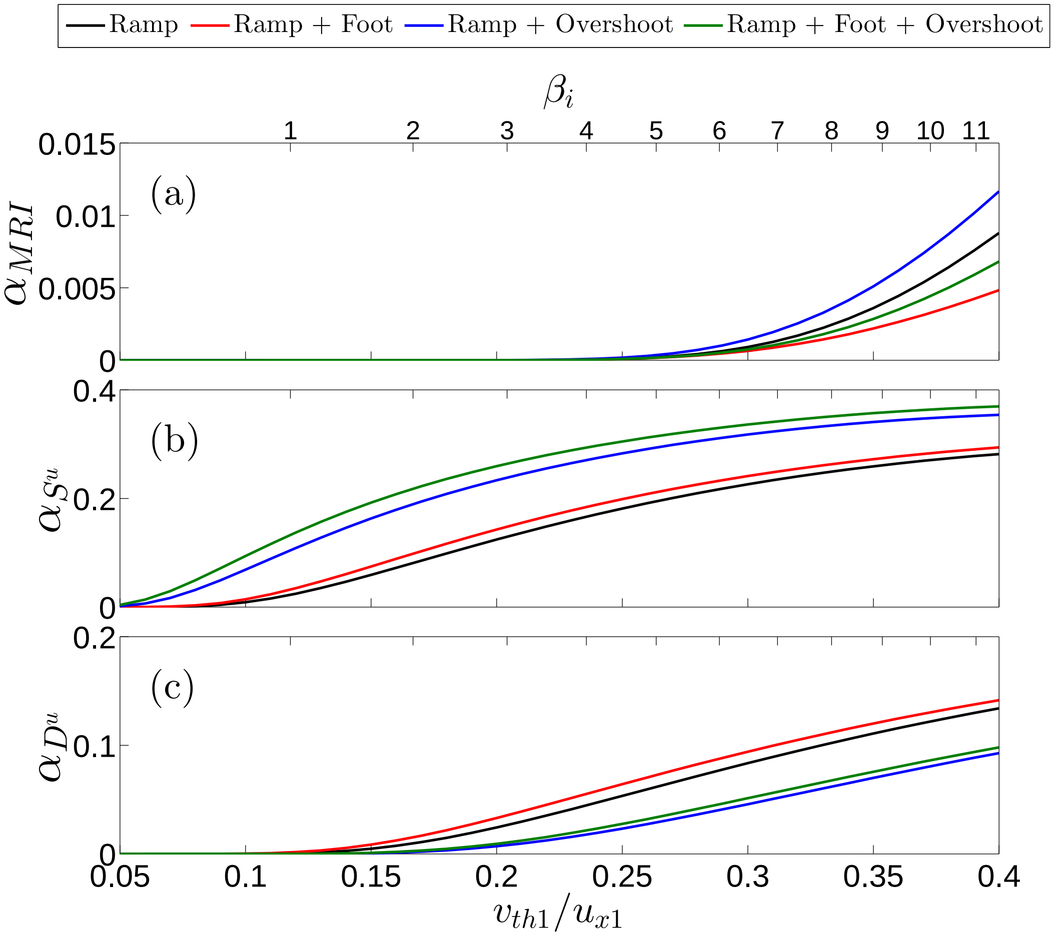

Figure 4.15: Fractional populations of MRI, S^u, and D^u particle groups from the test-particle simulations in Figure 4.10.

spatial profiles including a foot. Quantitatively, this is confirmed in Figure 4.15(a) which shows α_{MRI} is smaller for profiles with a foot region. Also MRI particles still constitute a very small fraction of the entire population, with a maximum value of 1.2% at $v_{th1}/u_{x1} = 0.4$ for the ramp and overshoot profile.

Figure 4.15(b) reveals that the addition of a foot or overshoot increases the S^u domain with small ($\sim 1\%$) and large ($\sim 10\%$) percentage gains in α_{S^u}, respectively. This is in contrast to values for α_{D^u} in Figure 4.15(c): the D^u population is slightly larger ($\sim 1\%$) for profiles with a foot but is significantly smaller for profiles with an overshoot, decreasing the D^u population by as much as $\sim 10\%$.

It is apparent from Figures 4.12, 4.13, 4.14, and 4.15 that the fractional populations of each particle class are sensitive to certain shock parameters, namely the electrostatic potential $\Delta\phi_E$, shock thickness l_r, and the spatial profiles of the electric and magnetic fields. Therefore in general it is difficult to ascertain a priori the importance of any particle class. Put it another way, based on these calculations it should not be assumed that D^u particles always correspond to the majority of the ion heating at shocks, as might be inferred from the emphasis on D^u particles [e.g. *Gedalin*, 1996]. It is important to note, however, that the results from our test-particle simulations and those of *Gedalin* [1996] and *Lever et al.* [2001] are not self-consistent, although *Lever et al.*'s [2001] shock parameters were extracted from 1-D hybrid simulations.

4.7 Conclusions

In this Chapter we proposed a new classification scheme that distinguishes between different classes of reflected particles based on their trajectories across a shock. This scheme was applied to test-particle simulations using the same shock parameters and field profiles as *Gedalin* [1996] and *Lever et al.* [2001]. Furthermore, we performed our own test-particle simulations which varied normalized ramp thickness l_r, electrostatic potential $\Delta\phi$, and spatial profiles of the electric and magnetic field.

We found that multiple classes of "reflected" particles typically exist at perpendicular shocks, with population fractions that depend on multiple shock parameters. Test-particle simulations show for $l_r \lesssim 1$ the ion distribution comprises of mainly S^u, D^u, and D^d particles. If the shock ramp is sufficiently thick, there exist particles that can now be reflected and turned-around in the ramp region, namely S^r and D^r particles. In addition, we found that particles with almost zero incoming normal speed $v_{x1}/u_{x1} \approx 0$ are reflected multiple times off the shock front, i.e. undergo MRI acceleration.

For each particle class we calculated its source region and compared them to two analytic separatrixes: one for S^u particles (4.1) and one for D^u and D^r particles (4.10). The S-separatrix depends on two parameters: the electrostatic cutoff speed v_c^E and the maximum reflection time τ (4.5), from which the latter gives the rotation angle $\Omega_{ci}\tau$ of the reflection separatrix. In all but one simulation, the S^u separatrix agreed extremely well with numerical simulations, being consistent in angle of rotation and location in phase space. The only exception was for *Gedalin*'s [1996] situation where the empirical value for τ produced a rotation angle that was consistent with the true separatrix found in the test-particle simulation.

The D-separatrix (4.10), which describes the source region of D^u and D^r particles, depends on several parameters: the downstream gyrocenter $\mathbf{w}_2$ and the velocity $\mathbf{v}_2$ of transmitted particles at the trailing of the ramp, where the latter parameter further depends on the electrostatic potential $\Delta\phi$, angle of rotation $\Omega_{ci}\tau$, and the velocity shift u_{y2} due to magnetic deflection. Our test-particle simulations show that the D-separatrix is relatively insensitive to $\Delta\phi$ but depends strongly on $\Omega_{ci}\tau$ and u_{y2}; specifically, a more negative value of u_{y2} shifts the separatrix vertically upwards in velocity phase space. For thicker shocks, the D-separatrix agreed poorly with numerical results; the challenge is being able to predict an accurate value for $\mathbf{v}_2$ across a thicker shock. However, in our revised prediction for the D-separatrix, (4.10) with (4.19) and (4.20), we confirmed the necessity of including a rotation angle $\Omega_{ci}\tau$ due to the natural gyromotion of the distribution through the foot and ramp.

We also investigated the energization of the different particle groups. In all cases we found that MRI particles have the greatest energization factor with, $\varepsilon \gtrsim 3$. This was followed closely by either D^u or S^u particles which had $\varepsilon \sim 1 - 3$. In general, particles are energized by drifting along the convective electric field; this fact was confirmed by calculating a particle's y-displacement between their upstream and downstream guiding centers. However, test-particle simulations do not account for other energization mechanisms, such as wave-particle interactions, which could possibly contribute to the net energization of the ion distribution.

Spatial variations in the magnetic and electric field profiles have modest effects on particle energy gains and their source regions. The most pronounced effect is due to the addition of a foot region; MRI energization and its particle source region are weaker and smaller, respectively. Including an overshoot region provides small energy gains for S^u and MRI particles and significantly increases the S^u population but significantly reduces the D^u population.

Finally, fractional populations of each particle class were calculated as functions of the upstream ion thermal speed v_{th1}, electrostatic potential $\Delta\phi_E$, ramp thickness l_r, and spatial variations in the magnetic and electric field profiles. Significant variation in particle populations are found between *Gedalin*'s [1996] simulation, *Lever et al.*'s [2001] simulation, and our model profiles with and without shock feet and overshoots. However, the values of α_{S^u} and α_{D^u} were comparable between our simulations and *Lever et al.*'s [2001] results. Note, however, that it is not currently possible to predict in detail the population and energization of each particle class since they depend on $\Delta\phi_E$, l_r, and the electromagnetic spatial profile which are not a priori predictable. This implies that D^u particles are not always the most important class of particles in terms of number fraction and energization, contrary to simulation results in *Gedalin* [1996]. Likewise S^u particles are unimportant if the difference between the electrostatic cutoff speed and upstream flow speed is much larger than the upstream thermal speed, i.e. $|v_c^E - u_{x1}| \gg v_{th1}$. Therefore, self-consistent calculations of these fractional populations and their energization are needed to truly determine the relative importance of each particle class.

Future work will quantify the energization fraction between different particle groups and study the MRI process in detail, for example, comparing the theoretical energy gains predicted in *Lee et al.* [1996] and *Zank et al.* [1996] to our numerical results.

Chapter 5

Concluding remarks and future directions

In this thesis we have addressed several outstanding problems in collisionless shock physics. In Chapter 2 we presented strong evidence from Voyager 2 data that the Uranian bow shock was reforming. Observations of extremely high and long-duration magnetic and density compressions by Voyager 2 can be explained simply in terms of the bow shock reforming and receding planetwards with the spacecraft. This interpretation was supported by a detailed analysis of Uranus's bow shock motions by *Xue et al.* [1996], using upstream Langmuir waves and magnetic connection conditions, which gave strong evidence that the bow shock was in fact moving away from the Sun, towards Uranus, just before the Voyager 2 encounter. This explanation was examined in detail using results from a 1-D hybrid simulation with similar plasma parameters to those observed at the Uranian bow shock. For a test spacecraft along a trajectory which remained close to the shock front, we found localized magnetic and density enhancements a factor of $4-6$ above the asymptotic predictions of the Rankine-Hugoniot relations, consistent with observations by Voyager 2. These results support the growing evidence for shock reformation occurring in nature [*Horbury et al.*, 2001; *Lobzin et al.*, 2007; *Mazelle et al.*, 2010; *Sundberg et al.*, 2013], and in particular for reformation appearing at extraterrestrial planetary shocks. Future work could investigate the existence of reformation for other planetary bow shocks and the heliospheric termination shock using a similar analysis to the one developed in Chapter 2.

Additional simulations showed that the relative magnetic overshoot $B_{\max}/B_1$ increases approximately linearly with M_A and is mostly insensitive to variations in magnetic field orientation. These large overshoots may be important in applications involving shock drift acceleration (SDA) and type II solar radio bursts. The reason is that if $M_A \gg 1$ then the maximum energy increase for a reflected particle under SDA, $E_{\max}/E = 2r + 2r\sqrt{1 - 1/r} - 1$ [*Ball and Melrose*, 2001], can be much larger and unbounded if the compression ratio is $r = B_{\max}/B_1$ rather than $r = B_2/B_1 \leq 4$ which gives the conventional bounded limit $E_{\max}/E \leq 13.93$. Future test-particle simulations for reforming shocks should be used to test this idea.

Chapter 3 provided the first quantitative treatment of the magnetic deflection process for thermal ions at quasiperpendicular shocks. We derived an analytic expression for the work done by magnetic deflection, W_{Bx}, which scales with the shock thickness squared and magnitude of the magnetic overshoot. In 1-D hybrid simulations of quasiperpendicular shocks with a wide range of $M_A \sim 1.8 - 10.3$, we found that the electrostatic potential $\Delta\phi_E$ decreases with M_A whereas the work done by magnetic deflection increases with M_A. Therefore, a purely electrostatic model for specular ion reflection would predict little to no ions being reflected at the maximum Mach-number. However, calculations of the average ion reflection efficiency $\langle\alpha\rangle$ in the same simulations showed a growing population of reflected ions with increasing M_A, specifically $\langle\alpha\rangle$ increasing steadily from $\sim 2\%$ at $M_A \sim 1.8$ to a maximum of $\sim 20\%$ at $M_A \sim 10.3$. This apparent discrepancy between theoretical and numerical values of the reflection efficiency was first acknowledged by *Leroy et al.* [1982]. Revised predictions of $\langle\alpha\rangle$, based on a total effective potential $e\Delta\phi = W_{Bx} - e\Delta\phi_E$ which includes the work done by magnetic deflection in addition to the electrostatic potential, recovered good agreement to the numerical values found in simulations, consistent in magnitude and variation with M_A.

Chapter 3 also investigated the source region of initially reflected ions. The separatrix in initial phase space between initially reflected ions and initially transmitted ions was derived analytically assuming ion reflection by (1) the electrostatic potential alone, and (2) the electrostatic potential plus the work done by magnetic deflection. Excellent agreement was found between both separatrixes and the source regions in numerical simulations of low M_A ($\sim 1.8-3.4$) shocks, which were consistent in rotation angle and location. However for stronger shocks with $M_A \gtrsim 3.4$, the separatrix derived under purely electrostatic effects deviated significantly from the true source region, whereas the separatrix which included magnetic deflection maintained excellent agreement to the simulation results. Thus it is clear from the results of Chapter 3 that magnetic field effects are vital for the reflection of thermal ions at and upstream of the shock overshoot, and for accurately predicting the reflection efficiency of ions at high Mach-number shocks. Future research should investigate the contribution of magnetic deflection to shock thermalization, which needs to be quantified and related to that required by the Rankine-Hugoniot conditions. In addition the new prediction for the separatrix should be compared with results from 2-D and 3-D hybrid and PIC simulations.

Chapter 4 addressed the need for a consistent and logical classification scheme for reflected particles. Our classification scheme is based on particle trajectories across the shock layer, specifically categorizing particles by identifying their reflection and turn-around locations in either the upstream, ramp, or downstream regions. For each particle class we determined its energization ε and source region in initial phase space. In general, we found MRI particles are most energized ($\varepsilon \gtrsim 3$) followed by either S^u or D^u particles with $\varepsilon \sim 1-3$, but depending on the shock parameters and field profiles. Each particle source region is sensitive to different shock parameters. For instance, MRI particles are mostly sensitive to the shock thickness and the addition of a foot region whereas D^u particles are sensitive to the shock thickness and magnetic jump factor but are insensitive to the electrostatic potential. These source regions were compared to two analytic reflection separatrixes: one predicting the S^u source region and the other predicting the D^u and D^r source region. In the former case we found excellent agreement between the predictions and the test-particle results whereas for the latter case the predictions only performed well for thinner shocks. Fractional populations of each particle class was also calculated; significant variation exists between simulations with differing upstream ion thermal speed, electrostatic potential, ramp thickness, and spatial variations in the electromagnetic field profile.

An important general result is that it is difficult to determine the source regions, energization, and fractional populations of each particle class because they depend on shock parameters which cannot be determined a priori. Future work should quantify and compare the relative energizations of the different particle groups and their contributions to the heating required by the Rankine-Hugoniot conditions. Additionally, comparisons should be made between the predicted energy gain of MRI particles (e.g. in *Lee et al.* [1996] and *Zank et al.* [1996]) and test-particle simulations similar to those in Chapter 4. As for Chapter 4, comparisons of the source regions, energization, and fractional populations of those classes should be made with 2-D and 3-D hybrid, test-particle, and PIC results.

Bibliography

Armstrong, T. P., M. E. Pesses, and R. B. Decker (1985), Shock drift acceleration, in *Collisionless shocks in the Heliosphere: Reviews of current research*, pp. 271–285, American Geophysical Union.

Bagenal, F., J. W. Belcher, E. C. Sittler, and R. P. Lepping (1987), The Uranian bow shock: Voyager 2 inbound observations of a high Mach number shock, *Journal of Geophysical Research: Space Physics*, *92*(A8).

Bale, S. D., F. S. Mozer, and T. S. Horbury (2003), Density-transition scale at quasiperpendicular collisionless shocks, *Physical Review Letters*, *91*, 265,004.

Bale, S. D., M. A. Balikhin, T. S. Horbury, V. V. Krasnoselskikh, H. Kucharek, E. Möbius, S. N. Walker, A. Balogh, D. Burgess, B. Lembège, et al. (2005), Quasi-perpendicular shock structure and processes, *Space Science Reviews*, *118*(1-4), 161–203.

Balikhin, M., V. Krasnosselskikh, and M. Gedalin (1995), The scales in quasiperpendicular shocks, *Advances in Space Research*, *15*(8), 247–260.

Ball, L., and D. B. Melrose (2001), Shock drift acceleration of electrons, *Publications of the Astronomical Society of Australia*, *18*(4), 361–373.

Baumjohann, W., and R. A. Treumann (1999), *Basic Space Plasma Physics*, Imperial College Press.

Biskamp, D., and H. Welter (1972), Ion heating in high-Mach-number, oblique, collisionless shock waves, *Physical Review Letters*, *28*, 410–413.

Buneman, O. (1958), Instability, turbulence, and conductivity in current-carrying plasma, *Physical Review Letters*, *1*, 8–9.

Burgess, D. (1989), Cyclic behavior at quasi-parallel collisionless shocks, *Geophysical Research Letters*, *16*(5), 345–348.

Burgess, D., W. P. Wilkinson, and S. J. Schwartz (1989), Ion distributions and thermalization at perpendicular and quasi-perpendicular supercritical collisionless shocks, *Journal of Geophysical Research: Space Physics*, *94*(A7), 8783–8792.

Burgess, D., E. Möbius, and M. Scholer (2012), Ion acceleration at the Earths bow shock, *Space Science Reviews*, *173*(1-4), 5–47.

Chapman, S., R. Lee, and R. Dendy (2005), Perpendicular shock reformation and ion acceleration, *Space Science Reviews*, *121*(1-4), 5–19.

Coroniti, F. V. (1970), Dissipation discontinuities in hydromagnetic shock waves, *Journal of Plasma Physics*, *4*, 265.

de Hoffmann, F., and E. Teller (1950), Magneto-hydrodynamic shocks, *Phys. Rev.*, *80*, 692–703.

Dimmock, A. P., M. A. Balikhin, V. V. Krasnoselskikh, S. N. Walker, S. D. Bale, and Y. Hobara (2012), A statistical study of the cross-shock electric potential at low Mach number, quasi-perpendicular bow shock crossings using Cluster data, *Journal of Geophysical Research: Space Physics*, *117*(A2).

Edmiston, J. P., and C. F. Kennel (1984), A parametric survey of the first critical mach number for a fast MHD shock, *Journal of Plasma Physics*, *32*(03), 429–441.

Forslund, D. W., R. L. Morse, and C. W. Nielson (1970), Electron cyclotron drift instability, *Physical Review Letters*, *25*, 1266–1270.

Forslund, D. W., K. B. Quest, J. U. Brackbill, and K. Lee (1984), Collisionless dissipation in quasi-perpendicular shocks, *Journal of Geophysical Research: Space Physics*, *89*(A4), 2142–2150.

Gedalin, M. (1996), Ion reflection at the shock front revisited, *Journal of Geophysical Research: Space Physics*, *101*(A3), 4871–4878.

Gedalin, M. (1997), Ion heating in oblique low-Mach number shocks, *Geophysical Research Letters*, *24*(20), 2511–2514.

Goodrich, C. C. (1985), Numerical simulations of quasi-perpendicular collisionless shocks, in *Collisionless Shocks in the Heliosphere: Reviews of Current Research*, pp. 153–168, American Geophysical Union.

Goodrich, C. C., and J. D. Scudder (1984), The adiabatic energy change of plasma electrons and the frame dependence of the cross-shock potential at collisionless magnetosonic shock waves, *Journal of Geophysical Research: Space Physics*, *89*(A8), 6654–6662.

Gosling, J. T., and A. E. Robson (1985), Ion reflection, gyration, and dissipation at supercritical shocks, *Collisionless shocks in the Heliosphere: Reviews of current research*, pp. 141–152.

Gosling, J. T., and M. F. Thomsen (1985), Specularly reflected ions, shock foot thicknesses, and shock velocity determinations in space, *Journal of Geophysical Research: Space Physics*, *90*(A10), 9893–9896.

Gosling, J. T., M. F. Thomsen, S. J. Bame, W. C. Feldman, G. Paschmann, and N. Sckopke (1982), Evidence for specularly reflected ions upstream from the quasi-parallel bow shock, *Geophysical Research Letters*, *9*(12), 1333–1336.

Greenstadt, E. W., and R. W. Fredricks (1979), Shock systems in collisionless space plasmas, *Space Plasma Physics*, *2*, 807.

Hellinger, P., P. Trávníček, and H. Matsumoto (2002), Reformation of perpendicular shocks: Hybrid simulations, *Geophysical Research Letters*, *29*(24).

Hellinger, P., P. Trávníček, B. Lembège, and P. Savoini (2007), Emission of nonlinear whistler waves at the front of perpendicular supercritical shocks: Hybrid versus full particle simulations, *Geophysical Research Letters*, *34*(14).

Hobara, Y., M. Balikhin, V. Krasnoselskikh, M. Gedalin, and H. Yamagishi (2010), Statistical study of the quasi-perpendicular shock ramp widths, *Journal of Geophysical Research: Space Physics*, *115*(A11).

Horbury, T. S., P. J. Cargill, E. A. Lucek, A. Balogh, M. W. Dunlop, T. M. Oddy, C. Carr, P. Brown, A. Szabo, and K.-H. Fornaçon (2001), Cluster magnetic field observations of the bowshock: Orientation, motion and structure, in *Annales Geophysicae*, vol. 19, pp. 1399–1409.

Kennel, C. F., J. P. Edmiston, and T. Hada (1985), A quarter century of collisionless shock research, in *Collisionless Shocks in the Heliosphere: A Tutorial Review*, pp. 1–36, American Geophysical Union.

Kivelson, M. G., and C. T. Russell (Eds.) (1995), *Introduction to Space Physics*, Cambridge University Press.

Knock, S. A., and I. H. Cairns (2005), Type II radio emission predictions: Sources of coronal and interplanetary spectral structure, *Journal of Geophysical Research: Space Physics*, *110*(A1).

Knock, S. A., I. H. Cairns, P. A. Robinson, and Z. Kuncic (2001), Theory of type II radio emission from the foreshock of an interplanetary shock, *Journal of Geophysical Research: Space Physics*, *106*(A11).

Knock, S. A., I. H. Cairns, P. A. Robinson, and Z. Kuncic (2003a), Theoretically predicted properties of type II radio emission from an interplanetary foreshock, *Journal of Geophysical Research: Space Physics*, *108*(A3).

Knock, S. A., I. H. Cairns, and P. A. Robinson (2003b), Type II radio emission predictions: Multiple shock ripples and dynamic spectra, *Journal of Geophysical Research: Space Physics*, *108*(A10).

Krasnoselskikh, V., M. Balikhin, S. N. Walker, S. Schwartz, D. Sundkvist, V. Lobzin, M. Gedalin, S. Bale, F. Mozer, J. Soucek, Y. Hobara, and H. Comisel (2013), The dynamic quasiperpendicular shock: Cluster discoveries, *Space Science Reviews*, *178*(2-4), 535–598.

Krasnoselskikh, V. V., B. Lembège, P. Savoini, and V. V. Lobzin (2002), Nonstationarity of strong collisionless quasiperpendicular shocks: Theory and full particle numerical simulations, *Physics of Plasmas*, *9*, 1192.

Kuncic, Z., I. H. Cairns, and S. Knock (2002), Analytic model for the electrostatic potential jump across collisionless shocks, with application to Earth's bow shock, *Journal of Geophysical Research: Space Physics*, *107*(A8), 1218.

Ledvina, S. A., Y. J. Ma, and E. Kallio (2008), Modeling and simulating flowing plasmas and related phenomena, *Space Science Reviews*, *139*(1-4), 143–189.

Lee, M. A., and L. A. Fisk (1982), Shock acceleration of energetic particles in the heliosphere, *Space Science Reviews*, *32*(1-2), 205–228.

Lee, M. A., V. D. Shapiro, and R. Z. Sagdeev (1996), Pickup ion energization by shock surfing, *Journal of Geophysical Research: Space Physics*, *101*(A3), 4777–4789.

Lembège, B., and J. M. Dawson (1987), Self-consistent study of a perpendicular collisionless and nonresistive shock, *Physics of Fluids (1958-1988)*, *30*(6).

Lembège, B., and P. Savoini (1992), Nonstationarity of a two-dimensional quasiperpendicular supercritical collisionless shock by self-reformation, *Physics of Fluids B: Plasma Physics (1989-1993)*, *4*(11).

Lembège, B., J. Giacalone, M. Scholer, T. Hada, M. Hoshino, V. Krasnoselskikh, H. Kucharek, P. Savoini, and T. Terasawa (2004), Selected problems in collisionless-shock physics, *Space Science Reviews*, *110*(3-4), 161–226.

Lembège, B., P. Savoini, P. Hellinger, and P. M. Trávníček (2009), Nonstationarity of a two-dimensional perpendicular shock: Competing mechanisms, *Journal of Geophysical Research: Space Physics*, *114*(A3).

Leroy, M. M. (1983), Structure of perpendicular shocks in collisionless plasma, *Physics of Fluids (1958-1988)*, *26*(9).

Leroy, M. M., C. C. Goodrich, D. Winske, C. S. Wu, and K. Papadopoulos (1981), Simulation of a perpendicular bow shock, *Geophysical Research Letters*, *8*(12), 1269–1272.

Leroy, M. M., D. Winske, C. C. Goodrich, C. S. Wu, and K. Papadopoulos (1982), The structure of perpendicular bow shocks, *Journal of Geophysical Research: Space Physics*, *87*(A7).

Lever, E. L., K. B. Quest, and V. D. Shapiro (2001), Shock surfing vs. shock drift acceleration, *Geophysical Research Letters*, *28*(7), 1367–1370.

Livesey, W. A., C. F. Kennel, and C. T. Russell (1982), ISEE-1 and -2 observations of magnetic field strength overshoots in quasi-perpendicular bow shocks, *Geophysical Research Letters*, *9*(9).

Livesey, W. A., C. T. Russell, and C. F. Kennel (1984), A comparison of specularly reflected gyrating ion orbits with observed shock foot thicknesses, *Journal of Geophysical Research: Space Physics*, *89*(A8), 6824–6828.

Lobzin, V. V., V. V. Krasnoselskikh, J.-M. Bosqued, J.-L. Pinçon, S. J. Schwartz, and M. Dunlop (2007), Nonstationarity and reformation of high-Mach-number quasiperpendicular shocks: Cluster observations, *Geophysical Research Letters*, *34*(5).

Matsukiyo, S., and M. Scholer (2003), Modified two-stream instability in the foot of high Mach number quasi-perpendicular shocks, *Journal of Geophysical Research: Space Physics*, *108*(A12).

Matsukiyo, S., and M. Scholer (2006), On microinstabilities in the foot of high Mach number perpendicular shocks, *Journal of Geophysical Research: Space Physics*, *111*(A6).

Mazelle, C., B. Lembège, A. Morgenthaler, K. Meziane, T. S. Horbury, V. Génot, E. A. Lucek, and I. Dandouras (2010), Self-reformation of the quasi-perpendicular shock: Cluster observations, in *AIP Conference Proceedings*, vol. 1216, p. 471.

Melrose, D. B. (1986), *Instabilities in Space and Laboratory Plasmas*, Cambridge University Press, Cambridge.

Morse, D. L., W. W. Destler, and P. L. Auer (1972), Nonstationary behavior of collisionless shocks, *Physical Review Letters*, *28*(1), 13.

Ofman, L. (2009), Progress, challenges, and perspectives of the 3D MHD numerical modeling of oscillations in the solar corona, *Space Science Reviews*, *149*(1-4), 153–174.

Pritchett, P. L. (2003), Particle-in-cell simulation of plasmas – A tutorial, in *Space Plasma Simulation*, *Lecture Notes in Physics*, vol. 615, edited by J. Büchner, M. Scholer, and C. T. Dum, pp. 1–24, Springer Berlin Heidelberg.

Quest, K. B. (1985), Simulations of high Mach-number collisionless perpendicular shocks in astrophysical plasmas, *Physical Review Letters*, *54*, 1872–1874.

Quest, K. B. (1986), Simulations of high Mach number perpendicular shocks with resistive electrons, *Journal of Geophysical Research: Space Physics*, *91*(A8), 8805–8815.

Russell, C. T. (1985), Planetary bow shocks, in *Collisionless Shocks in the Heliosphere: Reviews of Current Research*, pp. 109–130, American Geophysical Union.

Russell, C. T., M. M. Hoppe, and W. A. Livesey (1982), Overshoots in planetary bow shocks, *Nature*, *296*(5852), 48.

Scholer, M. (1985), Diffusive acceleration, in *Collisionless shocks in the Heliosphere: Reviews of current research*, vol. 35, pp. 287–301, American Geophysical Union.

Scholer, M., and S. Matsukiyo (2004), Nonstationarity of quasi-perpendicular shocks: A comparison of full particle simulations with different ion to electron mass ratio, *Annales Geophysicae*, *22*(7), 2345–2353.

Schwartz, S. J., M. F. Thomsen, and J. T. Gosling (1983), Ions upstream of the Earth's bow shock: A theoretical comparison of alternative source populations, *Journal of Geophysical Research: Space Physics*, *88*(A3), 2039–2047.

Sckopke, N., G. Paschmann, S. J. Bame, J. T. Gosling, and C. T. Russell (1983), Evolution of ion distributions across the nearly perpendicular bow shock: Specularly and non-specularly reflected-gyrating ions, *Journal of Geophysical Research: Space Physics*, *88*(A8), 6121–6136.

Sckopke, N., G. Paschmann, A. L. Brinca, C. W. Carlson, and H. Lühr (1990), Ion thermalization in quasi-perpendicular shocks involving reflected ions, *Journal of Geophysical Research: Space Physics*, *95*(A5), 6337–6352.

Scudder, J. D., A. Mangeney, C. Lacombe, C. C. Harvey, T. L. Aggson, R. R. Anderson, J. T. Gosling, G. Paschmann, and C. T. Russell (1986), The resolved layer of a collisionless, high β, supercritical, quasi-perpendicular shock wave: 1. Rankine-Hugoniot geometry, currents, and stationarity, *Journal of Geophysical Research: Space Physics*, *91*(A10).

Stone, R. G., and B. T. Tsurutani (1985), *Collisionless shocks in the Heliosphere: A tutorial review*, vol. 34, American Geophysical Union.

Sundberg, T., S. A. Boardsen, J. A. Slavin, V. M. Uritsky, B. J. Anderson, H. Korth, D. J. Gershman, J. M. Raines, T. H. Zurbuchen, and S. C. Solomon (2013), Cyclic reformation of a quasi-parallel bow shock at Mercury: MESSENGER observations, *Journal of Geophysical Research: Space Physics*, *118*(10), 6457–6464.

Tidman, D. A., and N. A. Krall (1971), *Shock waves in collisionless plasmas*, vol. 1, New York.

Tiu, D., I. H. Cairns, X. Yuan, and P. A. Robinson (2011), Evidence for reformation of the Uranian bow shock: Hybrid simulations and comparisons with Voyager data, *Journal of Geophysical Research: Space Physics*, *116*(A4).

Tsurutani, B. T., and R. G. Stone (1985), *Collisionless shocks in the Heliosphere: Reviews of current research*, American Geophysical Union.

Vlasov, A. A. (1968), The vibrational properties of an electron gas, *Sov. Phys. Usp.*, *10*(6), 721.

Winske, D., N. Omidi, K. B. Quest, and V. A. Thomas (1990), Re-forming supercritical quasi-parallel shocks: 2. Mechanism for wave generation and front re-formation, *Journal of Geophysical Research: Space Physics*, *95*(A11), 18,821–18,832.

Winske, D., L. Yin, N. Omidi, H. Karimabadi, and K. Quest (2003), Hybrid Simulation Codes: Past, Present and Future - A Tutorial, in *Space Plasma Simulation*, *Lecture Notes in Physics*, vol. 615, edited by J. Büchner, M. Scholer, and C. T. Dum, pp. 136–165, Springer Berlin Heidelberg.

Wu, C., D. Winske, Y. Zhou, S. Tsai, P. Rodriguez, M. Tanaka, K. Papadopoulos, K. Akimoto, C. Lin, M. Leroy, and C. Goodrich (1984), Microinstabilities associated with a high Mach number, perpendicular bow shock, *Space Science Reviews*, *37*(1-2), 63–109.

Wu, S. T., M. D. Andrews, and S. P. Plunkett (2001), Numerical magnetohydrodynamic (MHD) modeling of coronal mass ejections (CMEs), *Space Science Reviews*, *95*(1-2), 191–213.

Xue, S., I. H. Cairns, C. W. Smith, and D. A. Gurnett (1996), A study of Uranus' bow shock motions using Langmuir waves, *Journal of Geophysical Research: Space Physics*, *101*(A4).

Yuan, X., I. H. Cairns, and P. A. Robinson (2007), Hybrid simulation of reforming shocks with electron mass and pressure tensor effects, *Geophysical Research Letters*, *34*(2), L02,101.

Yuan, X., I. H. Cairns, and P. A. Robinson (2008a), Numerical simulation of electron distributions upstream and downstream of high Mach number quasi-perpendicular collisionless shocks, *Journal of Geophysical Research: Space Physics*, *113*(A8).

Yuan, X., I. H. Cairns, L. Trichtchenko, and R. Rankin (2008b), Effects of shock parameters on upstream energetic electron burst events, *Journal of Geophysical Research: Space Physics*, *113*(A9).

Yuan, X., I. H. Cairns, L. Trichtchenko, R. Rankin, and D. W. Danskin (2009), Confirmation of quasi-perpendicular shock reformation in two-dimensional hybrid simulations, *Geophysical Research Letters*, *36*(5).

Zank, G. P., H. L. Pauls, I. H. Cairns, and G. M. Webb (1996), Interstellar pickup ions and quasi-perpendicular shocks: Implications for the termination shock and interplanetary shocks, *Journal of Geophysical Research: Space Physics*, *101*(A1), 457–477.